MICROFLUIDICS-BASED TOOLS FOR CULTURE AND MULTI-FUNCTIONAL ASSESSMENTS OF THREE-DIMENSIONAL PLURIPOTENT STEM CELL DERIVED TISSUES

A Dissertation
Presented to
The Academic Faculty

By

Emily L. Jackson-Holmes

In Partial Fulfillment
Of the Requirements for the Degree
Doctor of Philosophy in Chemical & Biomolecular Engineering

Georgia Institute of Technology

August 2018

MICROFLUIDICS-BASED TOOLS FOR CULTURE AND MULTI-FUNCTIONAL ASSESSMENTS OF THREE-DIMENSIONAL PLURIPOTENT STEM CELL DERIVED TISSUES

Approved by:

Dr. Hang Lu, Advisor
School of Chemical & Biomolecular Engineering
Georgia Institute of Technology

Dr. Todd C. McDevitt, Advisor
Gladstone Institute of Cardiovascular Disease
Gladstone Institutes

Dr. Victor Breedveld
School of Chemistry and Biochemistry
Georgia Institute of Technology

Dr. Melissa Kemp
Department of Biomedical Engineering
Georgia Institute of Technology

Dr. Mark Styczynski
School of Chemical & Biomolecular Engineering
Georgia Institute of Technology

Date approved: June 14, 2018

To my family, for their lifelong love and support.

To Christopher, for his unconditional love and support.

ACKNOWLEDGEMENTS

First and foremost, I would like to thank my advisor, Hang Lu, for all of the guidance, mentoring, and support that she has provided over the course of my PhD. She has significantly contributed to my development as a scientist and researcher in many aspects, and for that I am grateful. I have particularly appreciated how she encourages her students to develop not just research-related skills, but also professional and interpersonal skills. I came to Georgia Tech planning (and hoping) to work with Hang and have been thankful for the opportunity to work with her.

I would also like to thank my co-advisor, Todd McDevitt, who has challenged me to think critically about my work. Being a part of his lab has brought a new, second perspective on my research, which has made it better and more impactful. I have also adopted many of his and his lab's high standards for creating scientific presentations, which have served me well throughout my PhD.

I would next like to thank my committee members, Victor Breedveld, Mark Styczynski, and Melissa Kemp. Each of them has been truly helpful in their guidance, suggestions, and critiques of my research. I appreciate the ways in which they have challenged me to think about my work, especially when I had initial ideas that were a bit over-zealous. In particular, I want to acknowledge Melissa for going above and beyond her role as a committee member in providing helpful suggestions for many of projects and generously allowing me to share her lab space and equipment. My collaborations and daily interactions with her and the rest of the Kemp lab have provided much-appreciated intellectual support and camaraderie through the last few years of my PhD. I would also

like to thank our collaborator, Zhexing Wen, and his students, all of whom have been amazingly supportive of our collaborative research efforts on the organoid platform project. From providing support on experiments and data analysis, to sharing my enthusiasm for potential commercialization of this project, I truly appreciate working with Zhexing.

I would next like to thank all of the past and present members of the Lu lab who have contributed to my graduate school experience. I thank Loice and Tom, for mentoring me, especially when I first joined the lab. Maria Elena, Kathleen, Dan, Tel, have each helped me with technical questions, image processing, and general brainstorming and troubleshooting. I also appreciate the conversations I have had with Guillaume and Yongmin on my work. Eric has been supportive as my desk mate, lunch buddy, and our lab manager. Seleipiri and Robin have worked with me closely on the organoid culture platform project, and I truly appreciate how they have contributed to this work. Weipeng has been a close friend both within and outside of the lab, and I am thankful for our friendship. For each of the other members of the lab, I appreciate the help and friendship that they have provided throughout my PhD experience.

I have had the opportunity to work with two phenomenal undergraduate researchers during my PhD, and I am thankful for how they have contributed to my research. Sharon Ochoa worked with me for one summer through the EBICS REU program, and I appreciate the contributions she made in microfluidic device development and the friendship that we formed. Amanda Schaefer worked with me for the last two years of my PhD, and I am extremely proud of the contributions she made to the work described in Chapter 3 of this thesis. She is an extremely intelligent and self-motivated

individual who needed very little guidance and supervision in the work that collaborated with me on.

I also want to thank graduate students in other labs that supported me throughout my PhD. In the McDevitt lab, I appreciate the training and mentoring that I received from Melissa, Jenna, and Doug. I also appreciate contributions and feedback from the rest of the McDevitt lab members on my earlier work. I would like to thank all of the members of the Kemp lab for sharing their workspace with me and being great research "neighbors". In particular, I sincerely thank Chad and Sarah for their friendship and support. I could always approach them with technical questions, troubleshooting issues, brainstorming, or just when I needed to complain about something.

Last but not least, I would like to thank my family. My parents, Bill and Tammy, and my brother, Bryan, have always provided me with love and support as I have pursued my goals, even when they took me all of the way across the country. I would not be where I am today without them. Finally, I cannot adequately express my gratitude for my husband, Christopher, who has supported me throughout this crazy journey to getting a PhD.

TABLE OF CONTENTS

Page

ACKNOWLEDGEMENTS iv
LIST OF TABLES x
LIST OF FIGURES xi
LIST OF SYMBOLS AND ABBREVIATIONS xix
SUMMARY xxi
CHAPTER 1 : INTRODUCTION 1
1.1 Pluripotent Stem Cell Aggregate Differentiation 1
1.1.1 Overview 1
1.1.2 Conventional Culture Methods and Challenges 2
1.1.3 Motor Neuron Differentiation 5
1.2 PSC-Derived Organoids for Modeling Human Tissues 6
1.2.1 Overview 6
1.2.2 Current Organoid Technology and Challenges 7
1.2.3 Brain Organoids 8
1.3 Microfluidic Approaches for Studying PSC Aggregates 10
1.3.1 Microfluidic Culture Methods for PSC Aggregates 11
1.3.2 Microfluidic Culture Methods for Organoids 12
1.3.3 Considerations in Microfluidic Culture 13
1.4 Thesis Objectives and Significance 14
CHAPTER 2 : A MICROFLUIDIC PLATFORM FOR LONGITUDINAL MONITORING AND MULTI-MODAL PHENOTYPIC ANALYSIS OF INDIVIDUAL STEM CELL AGGREGATES 15
2.1 Introduction 15
2.2 Materials and Methods 19
2.2.1 Device Fabrication 19
2.2.2 Mouse Embryonic Stem Cell Culture 19
2.2.3 Aggregate Formation and Culture 20
2.2.4 Device Loading and Operation 21

2.2.5 LIVE/DEAD Assay 22
2.2.6 Immunofluorescent Staining and Imaging 22
2.2.7 Fluorescent Image Analysis 23
2.2.8 Aggregate Size and Growth Rate Analysis 24
2.2.9 Peclet Number Calculation 25
2.2.10 Statistical Analysis 25
2.3 Results and Discussion 26
2.3.1 Design of the Microfluidic Device 26
2.3.2 Device Operation and Validation 28
2.3.3 Growth and size control 30
2.3.4 On-chip immunofluorescent staining and imaging analysis 33
2.4 Conclusions 36
CHAPTER 3 : MODULATION OF MOTOR NEURON DIFFERENTIATION OF STEM CELL AGGREGATES USING MICROFLUIDIC PERFUSION 37
3.1 Introduction 37
3.2 Materials and Methods 40
3.2.1 Device Fabrication 40
3.2.2 mESC Culture 40
3.2.3 Motor Neuron Differentiation of mESC Aggregates 41
3.2.4 Device Loading and Operation 42
3.2.5 Immunofluorescent Staining 43
3.2.6 Confocal Microscopy 44
3.2.7 Image Analysis 44
3.2.8 Statistical Analysis 46
3.3 Results and Discussion 46
3.3.1 Microfluidic Device Design 46
3.3.2 Differentiation under Continuous and Discontinuous Perfusion 50
3.3.3. Effects of increasing RA and Pur Delivery on pMN Differentiation 58
3.3.4 Influence of Device Asymmetry on Microenvironment and pMN Differentiation 66
3.4 Conclusions 71
CHAPTER 4 : DESIGN AND VALIDATION OF A PLATFORM FOR CULTURE AND ASSESSMENTS OF BRAIN ORGANOIDS 73

4.1 Introduction 73
4.2 Materials and Methods 77
4.2.1 Device Fabrication 77
4.2.3 Transport Modeling 79
4.2.4 Forebrain Organoid Culture 79
4.2.5 Organoid Culture in Microfluidic Devices 80
4.2.6 Live Imaging and Quantification 81
4.2.7 Immunohistology, Imaging, and Quantification 81
4.3 Results and Discussion 82
4.3.1 Design of First Generation, Diffusion-Based Microfluidic Device 82
4.3.2 Transport Modeling in First Generation Device Design to Inform Optimization Operating Conditions 84
4.3.3 Testing Organoid Culture in First Generation Device Design 93
4.3.4 Design of Second Generation, Flow-Through Microfluidic Device 106
4.3.5 Transport Modeling in Second Generation Device Design to Inform Optimization of Operating Conditions 108
4.3.6 Testing Organoid Culture in the Second Generation Device Design 112
4.4 Conclusions 117
CHAPTER 5 : CONCLUSIONS AND FUTURE WORK 120
5.1 Thesis Contributions 120
5.2 Future Directions 122
5.2.1 Investigating Roles of Autocrine and Paracrine Signaling in 3D Stem Cell Differentiation 123
5.2.2 Generation of Asymmetrically Patterned Stem Cell Tissues 123
5.2.3 Improvements to Brain Organoid Culture Platform 124
5.2.4 Drug Screening with Forebrain Organoids 125
APPENDIX A: CHAPTER 3 SUPPLEMENTARY MATERIAL 127
APPENDIX B: CHAPTER 4 SUPPLEMENTARY MATERIAL 132
APPENDIX C: CHAPTER 5 SUPPLEMENTARY MATERIAL 142
REFERENCES 144

LIST OF TABLES

Page

Table 3.1: Transport modeling parameters 55

Table 3.2: Spearman Rank Correlation Analysis of Olig2 Expression and Aggregate Size 57

Table 3.3: Spearman Rank Correlation Analysis of Olig2 Expression and Aggregate Size 62

Table 3.4: Percentages of aggregates blocking flow through traps 67

Table 4.1. Values for transport and reaction of key species. 86

LIST OF FIGURES

Page

Figure 2.1. Overview of microfluidic platform. a) Schematics illustrate the design of the device, with inset detailing the main channel, trap, and resistance channel. b,c) Diagrams show key device geometrical features. d) Photograph of a dye-filled device. e) Image shows the hydrodynamic loading mechanism, which is dependent on the balance of flow through the main channel versus flow through the traps and resistance channels..... 27

Figure 2.2. Validation of device culture. a) Experimental design. b) Phase contrast images show representative aggregates at days 1 and 4 of differentiation. c) Representative confocal images of day 4 aggregates treated with a LIVE/DEAD stain (live cells: green, dead cells: red); (i) Maximum projection images; (ii) single channel z planes. 29

Figure 2.3. Device culture reduces variability in aggregate size. a) Phase contrast images showing size and morphology at days 1 and 4. Red arrows indicate subpopulations of much smaller aggregates. White arrows indicate aggregates with budding morphologies. b) Aggregate radii were quantified from phase contrast images at day 1 (before loading into devices) and day 4 of differentiation. Two independent samples are shown for each condition, with $n \geq 80$ aggregates for batch and $n \geq 40$ aggregates for devices. * $P < 0.0001$. c) Aggregate growth rates for different starting sizes and device perfusion rates. Growth rate was defined as change in size between days 1 and 4, normalized by initial size. $n \geq 2$ batch samples or devices, respectively, per condition. All samples: n.s. 31

Figure 2.4. On-chip immunostaining and quantification of protein expression. (1) Immunostaining is performed on-chip by perfusing all reagents through the device via gravity-driven flow. (2) Confocal microscopy is used to image samples. (3) Image processing is used to quantify single-cell level protein expression within aggregates..... 33

Figure 2.5. Device facilitates studying individual sample phenotypes. a) Representative immunostaining images. b) Mean aggregate Oct4 expression for different culture platforms. Two independent experiments are shown for batch and device conditions ($n \geq 25$ each) and one experiment is shown for multiwell condition ($n = 8$). * $P < 0.00001$ vs. batch and $P < 0.0001$ vs. multiwell. c) Inter-aggregate heterogeneity in Oct4 expression for device and batch cultures. 35

Figure 3.1. Microfluidic device design. a) Schematic illustrates the design of the new, modified microfluidic device, with inset depicting the main channel, trap, and resistance channel. b) Schematics show key geometries and dimensions of the new design, compared to the previous design..... 47

Figure 3.2. Device and external fluid handling components. Photograph depicts the microfluidic device and external components, including the inlet and media reservoir, valves, outlet tubing, and filter. 50

Figure 3.3. Differentiation of mESC aggregates to motor neurons. a) Cartoon depicts the differentiation of mESCs first to pMNs marked by Olig2 and then to either Hb9+ MNs or Nkx2.2+ OPCs. b) Schematic shows the differentiation protocol used..... 51

Figure 3.4. Effects of media perfusion method on morphology. a) Aggregate cross-sectional area was measured from bright field images at day 7. b) Aggregate eccentricity was measured from bright field images at day 7. Continuous: n = 58 from 2 devices; Plate control: n = 41. Discontinuous: n = 67 from 2 devices; Plate control: n = 18. Error bars indicate SEM. Kruskal-Wallis test with Dunns multiple comparisons was used. * indicates $p < 0.01$; *** indicates $p < 0.0001$. 52

Figure 3.5. Effect of media perfusion method on differentiation of pMNs. a) Representative images from a single confocal slice of Olig2 expression at day 7 and corresponding bright field images. All scale bars are 100 μm. b) Normalized Olig2 expression quantified for each condition. Continuous: n = 58 from 2 devices; Plate control: n = 41 aggregates. Discontinuous: n = 37 from 1 device; Plate control: n = 18. Error bars represent SEM. Kruskal-Wallis test with Dunns multiple comparisons was used. *** indicates $p < 0.0001$. Plate controls were n.s..... 56

Figure 3.6. Effects of aggregate size and device position on pMN differentiation. a) Correlation between aggregate area and normalized Olig2 expression at day 7. b) Normalized Olig2 expression for aggregates in a single representative device plotted based on position in the device. Traps are numbered with respect to position along the serpentine channel, with trap 1 at the inlet and trap 105 at the outlet..... 57

Figure 3.7. Effects of discontinuous perfusion and RA and Pur concentrations on morphology. a) Aggregate cross-sectional area was measured from bright field images at day 7. b) Aggregate eccentricity was measured from bright field images at day 7. Discontinuous device: n = 94 from 2 devices. Plate control (6 μM/3 μM): n = 58. Plate control (2 μM/1.5 μM): n = 37. Error bars indicate SEM. Kruskal-Wallis test with Dunns multiple comparisons was used. * indicates < 0.01; *** indicates $p < 0.0001$. 60

Figure 3.8. Effects of discontinuous perfusion and RA and Pur concentration on differentiation of pMNs. a) Representative images from a single confocal slice of Olig2 expression at day 7 and corresponding bright field images. All scale bars are 100 μm. b) Normalized Olig2 expression quantified for each condition. Discontinuous device: n = 91 from 2 devices. Plate control (6 μM/3 μM): n = 58. Plate control (2 μM/1.5 μM): n = 33. Error bars represent SEM. Kruskal-Wallis test with Dunns multiple comparisons was used. *** indicates $p < 0.0001$..... 62

Figure 3.9. Effects of aggregate size and device position on pMN differentiation. a) Relationship between aggregate area and normalized Olig2 expression at day 7. b) Normalized Olig2 expression for aggregates in a single representative device plotted based on position in the device. Traps are numbered with respect to position along the serpentine channel, with trap 1 at the inlet and trap 105 at the outlet..... 63

Figure 3.10. Effects of discontinuous perfusion and RA and Pur concentration on differentiation of committed MNs. a) Representative images from a single confocal slice of normalized Hb9 and Olig2 expression at day 7 and corresponding bright field images. All scale bars are 100 μm. b) Normalized Hb9 expression quantified for each condition.

Discontinuous device: n = 37 from 1 device. Plate control (6 μM/3 μM): n = 25. Plate control (2 μM/1.5 μM): n = 14. Error bars represent SEM. Kruskal-Wallis test with Dunns multiple comparisons was used. ** indicates p < 0.001; *** indicates p < 0.0001. 64

Figure 3.11. Effects of discontinuous perfusion and RA and Pur concentration on differentiation of OPCs. a) Representative images from a single confocal slice of normalized Nkx2.2 and Olig2 expression at day 7 and corresponding bright field images. All scale bars are 100 μm. b) Normalized Nkx2.2 expression quantified for each condition. Discontinuous device: n = 56 from 1 device. Plate control (6 μM/3 μM): n = 23. Plate control (2 μM/1.5 μM): n = 15. Error bars represent SEM. Kruskal-Wallis test with Dunns multiple comparisons was used. * indicates p < 0.01; *** indicates p < 0.0001..... 65

Figure 3.12. Effects of discontinuous perfusion frequency on spatial characteristics of Olig2 expression. a) Image describes how metric is quantified. Histograms show population-level data for horizontal position of Olig2+ cells with respect to aggregate center line for (b) discontinuous perfusion (f = 1 d^{-1}) with 2 μM RA and 1.5 μM Pur (n = 31 from 1 device), (c) discontinuous perfusion (f = 3 d^{-1}) with 6 μM RA and 3 μM Pur (n = 47, representative of 2 devices), (d) plate controls with 2 μM RA and 1.5 μM Pur (n = 13), and (e) plate controls with 6 μM RA and 3 μM Pur (n = 25). 70

Figure 4.1. Design of the microfluidic platform for organoid culture. a) Schematic illustrates the design of organoid culture device in a top-down view, with inset depicting key trap and channel geometries. b) Schematic depicts a side view of a single chamber and channels for media delivery. c) Bright field image of chambers with organoids. 83

Figure 4.2. Device loading and assembly. Schematic depicts a side view of the device. Aggregates are loaded into devices with a pipette tip, and then devices are clamped against a glass slide for culture. 83

Figure 4.3. Depiction of how one chamber of the device was modeled. The geometry reflects a 2D side view of a single chamber with inlet and outlet channels. The organoid is modeled as a 2D circle centered at the bottom of the chamber. The heat map shows the velocity profile in the chamber for an inlet flow rate of 100 μL/hr. 85

Figure 4.4. Glucose transport and consumption. a) Graph shows average glucose concentration at organoid surface for a range of organoid sizes and media perfusion rates. b) Graph shows the change in average glucose concentration in one well of the SpinΩ bioreactor over a 48-hour period for a range of organoid sizes. 87

Figure 4.5. Modeling oxygen transport and consumption. a) Geometry used to model oxygen transport and consumption in the first generation microfluidic device. The heat map shows the velocity profile for a flow rate of 100 μL/hr. b) Graph shows average oxygen concentration at organoid surface in the center of five chambers in series for a range of organoid sizes and media perfusion rates. c) Graph shows the change in average oxygen concentration in one well of the SpinΩ bioreactor over a 48-hour period for a range of organoid sizes. 89

Figure 4.6. Small molecule transport and consumption. a) Graph shows average small molecule concentration at organoid surface for a range of organoid sizes and media

perfusion rates. b) Graph shows the change in average small molecule concentration in one well of the SpinΩ bioreactor over a 48-hour period for a range of organoid sizes.... 91

Figure 4.7. Lactate transport and secretion. a) Graph shows average lactate concentration at organoid surface for a range of organoid sizes and media perfusion rates. b) Graph shows the change in average lactate concentration in one well of the SpinΩ bioreactor over a 48-hour period for a range of organoid sizes. 91

Figure 4.8. Differences in glucose, small molecule, and lactate concentrations among culture chambers. Graphs show the modeled average (a) glucose, (b) small molecule, and (c) lactate concentrations at the organoid surface, within the chamber, and at the chamber outlet for every chamber in a given device. These were modeled for a 1.6 mm diameter organoid and a 200 μL hr^{-1} media perfusion rate..... 93

Figure 4.9. Representative bright field images of forebrain organoids. a) Images of two representative forebrain organoids culture in devices. b) Images of different representative forebrain organoids culture in tissue culture plates. c) Image of a D28 organoid cultured in device with round, neuroepithelial structures faintly visible and outlined in yellow. All scale bars: 100 μm. 95

Figure 4.10. Organoid size, morphology, and growth rate. a) Organoid diameter measured at days 14, 21, 28, and 35 of culture. Diameter was calculated from the cross-sectional area of organoids in brightfield images. Two-way ANOVA with Bonferroni posttests was used; * indicates $p < 0.01$. b) Organoid circularity at days 14, 21, 28, and 35 of culture was calculated from brightfield images. Two-way ANOVA with Bonferroni posttests was used; all samples n.s. c) Growth rate was calculated, defined as the difference in size between two time points and normalized by the size at the first of the two time points. Two-way ANOVA with Bonferroni posttests was used for devices only, as plate control growth rate was calculated from population averages. For all graphs, error bars indicate SEM. 97

Figure 4.11. Organoid size as a function of position in the device at D35. Diameters of day 35 forebrain organoids from 7 devices from 4 independent experiments are shown, with each device indicated by a different symbol. Numbering denotes position along the main serpentine channel with chamber 1 at the device inlet and chamber 30 at the device outlet. 98

Figure 4.12. Characterization of cellular proliferation. Immunohistological analysis was performed for (a) day 21, (b) day 35, and (c) day 42 forebrain organoids cultured in devices, plate controls, or the SpinΩ bioreactor. Representative images show staining for cellular proliferation (Ki67), NPCs (SOX2), and cell nuclei (DAPI). All scale bars are 100 μm. Images are representative of 20-40 organoids per time point. 3 independent experiments for day 21, 4 independent experiments for day 35, one experiment for day 42..... 99

Figure 4.13. Quantification of proliferation of NPCs. The percentage of proliferating (Ki67+) NPCs (SOX2+) was quantified from immunohistology images. Data is shown for device and plate cultures at days 21, 35, and 42. Error bars indicate S.D. ANOVA was used; ** indicates $p < 0.001$; *** indicates $p < 0.0001$. Data is representative of 20-40

organoids per time point. 3 independent experiments for day 21, 4 independent experiments for day 35, one experiment for day 42. 100

Figure 4.14. Characterization of forebrain organoid differentiation. Immunohistological analysis was performed for (a) day 21, (b) day 35, and (c) day 42 forebrain organoids cultured in devices, plate controls, or the SpinΩ bioreactor. Representative images show staining for NPCs (SOX2), cortical plate layer markers (TBR1, MAP2) and cell nuclei (DAPI). All scale bars are 100 μm. Images are representative of 20-40 organoids per time point. 3 independent experiments for day 21, 4 independent experiments for day 35, one experiment for day 42. 102

Figure 4.15. Quantification of VZ and CP layer thickness. The relative thicknesses of VZ (SOX2+) and CP (TBR1+) layers were quantified from immunohistology images. Data is shown for (a) device and (b) plate cultures at days 21, 35, and 42. Error bars indicate S.D. Data is representative of 20-40 organoids per time point. 3 independent experiments for day 21, 4 independent experiments for day 35, one experiment for day 42. 103

Figure 4.16. Characterization of cell death within forebrain organoids. Immunohistological analysis was performed for (a) day 21, (b) day 35, and (c) day 42 forebrain organoids cultured in devices or plate controls. Representative images show staining for NPCs (SOX2), the cell death marker caspase-3 (CASP3), a CP layer marker (TUJ1), and cell nuclei (DAPI). All scale bars are 100 μm. Images are representative of 20-40 organoids per time point. 3 independent experiments for day 21, 4 independent experiments for day 35, one experiment for day 42. 104

Figure 4.17. Quantification of cell death in organoids. a) The percentage of organoids with intact overall structure was manually quantified from bright field images for organoids cultured in devices and plate controls at days 21, 35, and 42. b) The percentage of dead cells (CASP3+) was quantified from immunohistology images for devices and plate controls at days 21, 35, and 42. Error bars indicate S.D. ANOVA was used; all groups: n.s. Data is representative of 20-40 organoids per time point. 3 independent experiments for day 21, 4 independent experiments for day 35, one experiment for day 42..... 105

Figure 4.18. Design of the second generation, flow-through microfluidic device for organoid culture. a) Schematic illustrates the design of both device layers in a top-down view. b) Schematic depicts enlarged top view and perspective views of a single chamber with key dimensions noted..... 107

Figure 4.19. Assembly of the device. Schematic shows each of the device layers and order of assembly. 108

Figure 4.20. Depiction of how one chamber of the device was modeled. The geometry reflects a 2D side view of a single chamber with inlet and outlet channels. The organoid is modeled as a 2D circle centered at the bottom of the chamber. The heat map shows the velocity profile in the chamber for an inlet flow rate of 100 μL/hr. 109

Figure 4.21. Glucose transport and consumption. a) Graph shows average glucose concentration at organoid surface for a range of organoid sizes and media perfusion rates. 110

Figure 4.22. Modeling oxygen transport and consumption. a) Geometry used to model oxygen transport and consumption. Heat map shows the velocity profile for a flow rate of 100 µL/hr. b) Graph shows average oxygen concentration at organoid surface in the center of seven chambers in series for a range of organoid sizes and media perfusion rates. 112

Figure 4.23. Representative bright field images of forebrain organoids. a) Images of representative forebrain organoids cultured in devices or static plate controls at days 14, 21, 28, and 35. Devices were operated with media exchange every 24 hours (24 hr^{-1}) or continuous perfusion at 200 µL hr^{-1}. All scale bars: 100 µm..... 115

Figure 4.24. Organoid size, morphology, and growth rate. a) Organoid diameter measured at days 14, 21, 28, and 35 of culture. Diameter was calculated from the cross-sectional area of organoids in bright field images. Two-way ANOVA with Bonferroni posttests was used; * indicates $p < 0.01$. b) Organoid circularity at days 14, 21, 28, and 35 of culture was calculated from bright field images. Two-way ANOVA with Bonferroni posttests was used; * indicates $p < 0.01$. c) Growth rate was calculated, defined as the difference in size between two time points and normalized by the size at the first of the two time points. Two-way ANOVA with Bonferroni posttests was used for devices only, as plate control growth rate was calculated from population averages. * indicates $p < 0.01$. For all graphs, error bars indicate SEM. 116

Appendix A.1. Stitched representative image of a device loaded with 1000 cell aggregates. Black arrows indicate singly loaded traps. 127

Appendix A.2. Additional viability data. Representative confocal images of day 4 aggregates treated with a LIVE/DEAD stain (live cells: green; dead cells: red). For each condition, the top image is a maximum intensity projection of all z slices imaged for a given aggregate. Underneath, three z slices are shown. a) Images for both 1000 cell starting size aggregates cultured at 10 µL/hr and for 500 cell starting size aggregates cultured at 5 µL/hr. b) Images for 100 cell starting size and 500 cell starting size aggregates cultured in batch. All scale bars: 100 µm. 128

Appendix A.3. a) Device culture reduces variability in size for 500 cell starting size aggregates. Aggregate radii were quantified from phase contrast images at day 1 and day 4 of differentiation for 500 cell aggregates cultured under 10 µL/hr media perfusion). Two independent samples are shown for each condition, with $n \geq 100$ for batch samples and $n \geq 85$ for device samples. * $P < 0.01$; *** $P < 0.0001$. b) Size distributions of aggregates captured in devices are similar to batch aggregates. Two replicates per condition are shown for 1000 cell aggregates (device culture: 10 µL/hr media perfusion). ** $P < 0.001$; *** $P < 0.0001$ c) Schematic of trap numbering convention used in c and d. c,d) Aggregate radii is plotted as a function of position within the device, for 1000 cell aggregates cultured under 10 µL/hr perfusion. Two devices are shown for days 1 and 4 of differentiation..... 129

Appendix A.4. Image processing pipeline used to analyze fluorescent images modified from Lou, et al.[110]..... 130

Appendix A.5. a) Schematic of trap numbering convention used in b. b) Mean aggregate Oct4 expression is plotted as a function of position within the device. One device is shown. Performing linear regression on this data produced a line of slope -0.002 and an R^2 value of 0.141, indicating no trend between Oct4 expression and position. c,d) Mean aggregate Oct4 expression is plotted as a function of aggregate radius at day 1 (c) and day 4 (d). e) Scatter plot shows mean Oct4 expression for individual aggregates cultured within batch, multiwell, or device platforms (raw data corresponding to Figure 5b). Two independent experiments are shown for batch and device conditions ($n \geq 25$ each) and one experiment is shown for multiwell condition ($n = 8$). * $P < 0.00001$ vs. both batch and multiwell samples, $P < 0.0001$ vs. other device sample. f) Intra-aggregate heterogeneity in Oct4 expression for device and batch platforms. Two independent experiments are shown for batch and device conditions ($n \geq 25$ each). # $P < 0.001$, $ $P < 0.00001$, & $P < 0.0001$. 131

Appendix B.1. Histograms show horizontal position of Olig2+ cells with respect to aggregate center line for discontinuous perfusion (f = 1 d-1) with 2 μM RA and 1.5 μM Pur. Zero indicates aggregate center line, positive numbers indicate portion of aggregate closer to trap entrance, and negative numbers indicate portion of aggregate closer to back of trap 133

Appendix B.2. Histograms show horizontal position of Olig2+ cells with respect to trap coordinates for discontinuous perfusion ($f = 1\ d^{-1}$) with 2 μM RA and 1.5 μM Pur. Zero indicates trap entrance and 1 indicates back of trap, where circular trap meets restriction channel. 134

Appendix B.3. Histograms show horizontal position of Olig2+ cells with respect to aggregate center line for discontinuous perfusion ($f = 3\ d^{-1}$) with 6 μM RA and 3 μM Pur, one device. Zero indicates aggregate center line, positive numbers indicate portion of aggregate closer to trap entrance, and negative numbers indicate portion of aggregate closer to back of trap. 136

Appendix B.4. Histograms show horizontal position of Olig2+ cells with respect to aggregate center line for discontinuous perfusion ($f = 3\ d^{-1}$) with 6 μM RA and 3 μM Pur, a second device. Zero indicates aggregate center line, positive numbers indicate portion of aggregate closer to trap entrance, and negative numbers indicate portion of aggregate closer to back of trap. 137

Appendix B.5. Histograms show horizontal position of Olig2+ cells with respect to trap coordinates for discontinuous perfusion ($f = 3\ d^{-1}$) with 6 μM RA and 3 μM Pur, one device. Zero indicates trap entrance and 1 indicates back of trap, where circular trap meets restriction channel. 138

Appendix B.6. Histograms show horizontal position of Olig2+ cells with respect to trap coordinates for discontinuous perfusion ($f = 3\ d^{-1}$) with 6 μM RA and 3 μM Pur, a second device. Zero indicates trap entrance and 1 indicates back of trap, where circular trap meets restriction channel. 139

Appendix B.7. Histograms show horizontal position of Olig2+ cells with respect to aggregate center line for plate controls with 6 μM RA and 3 μM Pur. Zero indicates

aggregate center line, positive numbers indicate portion of aggregate closer to trap entrance, and negative numbers indicate portion of aggregate closer to back of trap. ... 140

Appendix B.8. Histograms show horizontal position of Olig2+ cells with respect to aggregate center line for plate controls with 2 μM RA and 1.5 μM Pur. Zero indicates aggregate center line, positive numbers indicate portion of aggregate closer to trap entrance, and negative numbers indicate portion of aggregate closer to back of trap. ... 141

Appendix C.1. Organoid size distributions. Organoid diameter measured at days 14, 21, 28, and 35 of culture. Diameter was calculated from the cross-sectional area of organoids in brightfield images. Each dot represents an individual organoid. Growth rate was calculated, defined as the difference in size between two time points and normalized by the size at the first of the two time points. Error bars are SEM. 142

Appendix C.2. Organoid growth rate distributions in device cultures. Growth rate was calculated, defined as the difference in size between two time points and normalized by the size at the first of the two time points. Error bars are SEM. 143

LIST OF SYMBOLS AND ABBREVIATIONS

2D	Two-dimensional
3D	Three-dimensional
CASP3	Caspase-3
CFD	Computational fluid dynamics
CP	Cortical Plate
CPR	Critical perfusion rate
CV	Coefficient of variation
EB	Embryoid body
ECM	Extracellular matrix
ECT	Effective culture time
ESC	Embryonic stem cell
GFP	Green fluorescent protein
iPSC	Induced pluripotent stem cell
LIF	Leukemia inhibitory factor
mESC	Mouse embryonic stem cell
MN	Spinal motor neuron
NPC	Neural progenitor cell
OPC	Oligodendrocyte precursor cell
PDMS	Polydimethylsiloxane
Pe	Peclet number

pMN	Progenitor motor neuron
PSC	Pluripotent stem cell
Pur	Purmorphamine
RA	Retinoic acid
Shh	Sonic hedgehog
SpinΩ	SpinOmega bioreactor
VZ	Ventricular zone

SUMMARY

Due to their capacity for self-renew and differentiation, pluripotent stem cells (PSCs) are used as a cell source in applications including tissue engineering, regenerative medicine, and studies of human development and disease. A common format for PSC differentiation is as three-dimensional (3D) cell aggregates. Differentiation of PSCs as aggregates mimics biochemical and biophysical aspects of *in vivo* embryonic development that promote differentiation and complex cell behaviors. Aggregates are used as a format both in directed differentiation approaches and in generating complex human tissue models such as organoids. Key challenges in generating and studying PSC aggregates include the low throughput and time-consuming nature of culture techniques, the lack of precise control over the culture microenvironment, and the inability to perform a variety of *in situ* functional assays. This thesis focuses on addressing some of these challenges through the development of microfluidics-based technologies for culture and assessment of stem cell aggregates.

In Chapter 2 of this thesis, I developed a microfluidic platform for longitudinal monitoring and multi-modal phenotypic analysis of individual stem cell aggregates. This platform uses a hydrodynamic loading principle to capture pre-formed aggregates in independent traps, which enables physical isolation and tracking of aggregates during culture. I demonstrated that culture of aggregates in individual traps reduces heterogeneity in parameters such as size and gross morphology. Additionally, culture and analysis steps such as immunostaining and imaging could be performed sequentially in

the same platform, enabling correlation of multiple modes of analysis for individual samples.

In Chapter 3 of this thesis, I applied the microfluidic platform developed in Chapter 2 in exploring how microfluidic culture parameters influence stem cell behavior and differentiation in the context of motor neuron differentiation. Transport modeling and experimental studies were used to assess how media exchange frequency and asymmetrical device geometries modulated the biochemical environment and differentiation. These studies demonstrated that discontinuous media perfusion was effective at supporting PSC aggregate growth, but there was a balance between sufficient media exchange frequency and allowing accumulation of required cell-secreted. Finally, work in this chapter showed how asymmetrical microscale geometries can be used to generate gradients of cell-secreted factors and induce asymmetric differentiation events.

In Chapter 4 of this thesis, I developed a culture platform for brain organoids. This aim built upon technologies presented in the first two aims and extended these for much larger organoid tissue models. The platform developed in this aim allows culture of individual organoids in an array of chambers with controlled delivery of media and reagents, the ability to perform imaging-based assays, and the ability to retrieve organoids for end-point based assays. I developed and validated two iterations of the platform design. With each design, computational fluid dynamics and qualitative transport modeling were used to validate design choices and optimize culture conditions. I validated culture of forebrain organoids in the platforms for up to 42 days through characterization of organoid size, morphology, cell types, and structural features. Results from these analyses revealed that organoids cultured in the microfluidic platform

developed comparably to conventional methods. Together, the work performed in this thesis establishes a set of technologies for higher throughput, robust formation of stem cell derived tissues of multiple size scales, coupled with highly informative assays. These tools provide new capabilities that can be broadly applied by other researchers in studies of 3D stem cell differentiation and in generation of stem cell derived tissue models.

CHAPTER 1 : INTRODUCTION

The chapter provides an introduction to three-dimensional pluripotent stem cell tissues, their applications, and challenges with current culture and analysis techniques. Portions of this chapter are adapted from the following two publications: "Three-dimensional models for studying development and disease: moving on from organisms to organs-on-a-chip and organoids" published in Integrative Biology in 2016[1] and "A microfluidic trap array for longitudinal and multi-modal phenotypic analysis of individual stem cell aggregates" published in Lab on a Chip in 2017[2].

1.1 Pluripotent Stem Cell Aggregate Differentiation

1.1.1 Overview

Pluripotent stem cells (PSCs) are uniquely able to self-renew and to differentiate into cells from each of the three germ lineages as well as germ cells. Due to these capabilities, PSCs have been widely studied for applications in understanding human developmental biology and developing tissue engineering strategies. Types of PSCs include embryonic stem cells (ESCs), which are derived from the inner cell mass of an embryo[3-5], and induced pluripotent stem cells (iPSCs), which are created through reprogramming of somatic cells. The ability to generate iPSCs was first reported in 2006 by Yamanaka[6,7] and then independently by others[8-10]. iPSCs are similar to ESCs in terms of developmental potential and self-renewal but with additional advantages, including the relative ease of generating cell lines, the ability to generate patient- and disease-specific cells, and the avoidance of ethical issues associated with the source of ESCs. For these reasons, iPSCs have generated much excitement for use in disease modeling, drug discovery, and development of cell therapies.

One common format for differentiation of PSCs is as three-dimensional (3D) aggregates. In this format, many of the biochemical and biophysical interactions that occur during *in vivo* early embryonic development are mimicked[11,12]. In some contexts, PSC aggregates are referred to as "embryoid bodies" (EBs), a term that describes spontaneous differentiation to cell types from each of the three germ lineages. EB differentiation has applications in modeling embryonic development and tissue morphogenesis. In addition to applications in studying embryonic development, PSC aggregates are frequently used as a step in directed differentiation protocols, including cardiac[13] and neural differentiation[14], as they promote cell-cell signaling and other interactions that facilitate differentiation. A variety of strategies have been developed for directing differentiation of aggregates, and examples of these include control of aggregate size[15-20], delivery of soluble factors, encapsulation in polymer matrices[21-23], and incorporation of microparticles[24-26]. Despite the development of many strategies for directed differentiation of PSCs in an aggregate format, there are still challenges in controlling differentiation and an incomplete understanding of the mechanisms that regulate differentiation. This thesis does not directly focus on these challenges, but rather on developing technologies that provide new capabilities for culture and phenotypic assesses of PSC aggregates. These technologies can then enable studies to improve understanding of stem cell differentiation. In the next section, an overview of current culture methods and their challenges is provided.

1.1.2 Conventional Culture Methods and Challenges

A variety of methods have been developed for formation and culture of PSC aggregates which facilitate control over directing differentiation. Although this thesis

does not focus on methods for aggregate formation specifically, they are briefly described here to provide context. Aggregate formation methods include the spontaneous aggregation of cells seeded in low attachment tissue culture plates[5] or hanging drops[27] and the forced aggregation of cells by centrifugation in multiwell plates[28,29] or microwells[18,30-32]. When aggregates are formed individually in hanging drops, 96-well plates, and microwells, the initial aggregate size can be specified by adjusting the cell seeding density. The consistent aggregate size produced by these methods reduces heterogeneity in the starting population, and controlling aggregate size is important, as size has been shown to influence differentiation.[18-20,33]

Following formation, aggregates can be cultured in different types of culture systems. In batch-based culture platforms, aggregates are grown in suspension in petri dishes or larger vessels such as bioreactors, either under static[5] or stirred conditions[13,16,17,34]. In static suspension culture, gradients of nutrients, metabolites, and soluble signaling molecules can form in the local environments of individual aggregates. In contrast, stirred suspension culture promotes more uniform spatial concentrations of soluble factors through mixing. The primary advantage of batch-based culture methods is the ability to culture many aggregates at once (up to 1,000s per culture vessel). However, one disadvantage is that aggregates can physically interact with one another in a stochastic manner, for example, when multiple aggregates agglomerate. These interactions can contribute to heterogeneity in the cultures. A second key disadvantage is the inability to observe and track individual aggregates throughout culture. Collecting phenotypic information through time for individual samples is valuable for investigating,

for example, how differentiation processes evolve and how different phenotypic metrics correlate with one another.

The second category of conventional aggregate culture systems is comprised of culture platforms that maintain individual aggregates in physically separate compartments. These include multiwell plates[28,29], microwells[18,30-32], and hanging drops[27]. Each of these culture systems enables manipulation and observation of individual aggregates, capabilities which batch culture methods do not provide. However, these systems can require time- and labor-intensive culture procedures that involve manipulation of individual aggregates and individual volumes of media. A second disadvantage is that high-resolution imaging is difficult to perform *in situ* for observing cell and aggregate phenotypes: the curved material comprising the bottom of a multiwell plate or microwell required for aggregate formation typically does not have a thickness, index of refraction, or shape suitable for confocal imaging. For hanging drop culture, imaging *in situ* at high magnification requires water immersion objectives which introduce risk of contamination into ongoing cultures. Finally, performing end point based phenotypic assays, such as immunostaining, in the same platform as used for culture can save time and labor and enable correlation of live and end point phenotypes. However, the many liquid handling steps required for immunostaining are tedious and use large volumes of reagents when performed in microwells, multiwell plates, or hanging drops.

Overall, the disadvantages associated with current PSC aggregate culture systems demonstrate the need for new culture technologies. Ideally, new culture platforms would enable the differentiation of aggregates in well-controlled environments with minimal

required manual manipulation, longitudinal tracking of samples, and the ability to perform live- and end-point imaging-based phenotypic assays. This thesis will address these technological needs through the development of microfluidics-based culture systems for handling, culture, and performing imaging-based assessments of PSC aggregate differentiation.

1.1.3 Motor Neuron Differentiation

In order to demonstrate the capabilities of the microfluidic technologies developed in Chapters 2 and 3 of this thesis, they were applied to studying differentiation of mouse embryonic stem cells (mESCs) to spinal motor neurons (MNs). Differentiation protocols for generating MNs from ESCs and iPSCs are relatively well-established in literature, and MNs are a cell type that can potentially be used in therapeutic applications. These two considerations motivated using a MN differentiation protocol as an example application of our microfluidic technologies. To provide background and context for the biological studies performed in Chapter 3, a brief overview of MN differentiation is provided here.

Previous work has investigated how MNs are generated during embryonic development and mimicked the developmental signaling *in vitro* to differentiate MNs from both ESCs[35-37] and iPSCs[38]. For differentiation, PSCs are first formed into EBs and then exposed to the caudalizing signal retinoic acid (RA) to yield spinal progenitors. Next, upon exposure to the ventralizing signal Sonic hedgehog (Shh), spinal progenitors differentiate into progenitor motor neurons (pMNs). pMNs are characterized by the expression of the basic helix-loop-helix transcription factor Olig2[39,40]. Committed MNs are generated from pMNs through downregulation of Olig2 and expression of

homeodomain transcription factor Hb9[39,40]. In addition to committed MNs, pMNs also give rise to oligodendrocytes and astrocytes[41,42]. Previous studies have focused on understanding the signaling events that regulate these fate transitions and developing methods to generate MNs with higher efficiency and purity[43-45]. Together, previous work has contributed to an overall understanding of how MNs can be generated from PSCs. In Chapter 3, this differentiation pathway is applied in exploring how microfluidic culture parameters influence cell behavior and differentiation.

1.2 PSC-Derived Organoids for Modeling Human Tissues

1.2.1 Overview

Recent work has shown the ability to generate organoids, which are 3D tissues derived from PSCs that mimic key tissue- and organ-specific features of cellular assembly, integration, and organization. Strategies for generating organoids rely on the self-organizing capabilities of PSCs, as opposed to traditional directed differentiation approaches[46,47]. More specifically, strategies for promoting self-organization aim to exploit and facilitate endogenously produced developmental signals to promote differentiation and morphogenesis of tissues. In contrast, directed differentiation methods often focus on using exogenous compounds to sequentially activate and inhibit key signaling pathways in a population of cells. To date, organoids have been developed for a range of tissues types, including the optic cup[48], intestine[49], kidney[50], liver[51], brain[52]. Protocols for generating organoids share commonalities across different tissue types. They typically begin with the formation of an EB, followed by culture in different media formulations to facilitate self-organization, differentiation, and morphogenesis processes for the desired tissue type. A key step in most organoid protocols is embedding the EB in

Matrigel, an extracellular matrix (ECM) based hydrogel extracted from the Engelbreth-Holm-Swarm mouse sarcoma. Although the role of Matrigel is not completely understood, Matrigel seems to provide structural support and cell-ECM interactions that facilitate organoid development.

One of the exciting applications of organoid cultures is for modeling human development and disease[53,54]. Organoids can potentially address gaps in knowledge in understanding diseases that are difficult or impossible to study using animal models—for example, because of significant physiological or behavioral differences. A key advantage is the ability to generate organoids from disease- and patient-specific iPSCs. Overall, organoids provide an exciting technology for studying development and disease in complex, human-specific tissue models. This thesis focuses on the development of new tools for culture and assessments of organoids. The goal is to provide new methods for studying organoids, thus enabling broader use of organoids in fundamental biological studies and in drug development.

1.2.2 Current Organoid Technology and Challenges

A number of current challenges associated with producing organoids stem from the complexity of the biological processes involved in organogenesis. For self-organization of cells into functional tissues to occur, a complex orchestration of events such as cell differentiation, cell migration, timed activation of signaling pathways, and formation of tissue architecture is required. As a result, *in vitro* organoid cultures are often highly heterogeneous. Furthering our understanding of the cues involved in self-organization of tissues during *in vivo* development can aid in improving methods for robustly generating organoids. In working to better understand how to reproducibly

generate organoids, there is a need for improved technologies for culturing organoids and characterizing organoid phenotypes. Existing culture procedures require time-consuming manual manipulation steps, such as embedding of individual organoids in Matrigel[55] and mechanical removal of Matrigel at later time points during culture. In addition, the culture platforms that are typically used for organoids have a number of disadvantages. Organoids are typically cultured in platforms such as spinning bioreactors[52], tissue culture plates, miniaturized spinning bioreactors[56], and multiwell plates. Large bioreactors require large volumes of costly media and take up significant space; these issues make it difficult to multiplex experimental conditions. Tissue culture plates and multiwell plates use smaller media volumes and allow some multiplexing, but not to the extent required for large-scale screening. Disadvantages of these current systems highlight the need for new, miniaturized, culture technologies for use with organoids. In addition, the integration of imaging-based analysis tools with culture technologies will provide new abilities for characterization of live and intact organoid tissues. If methods such as live imaging, tissue clearing[57-60], and immunocytochemistry can be performed in culture platforms, this will better facilitate screening. In this thesis, to address challenges associated with current organoid technologies, a miniaturized platform for organoid culture and screening was developed. This technology provides new capabilities for culture of individual organoids, imaging-based assessments, and screening, and it will enable future work in understanding how to generate organoids more reproducibly.

1.2.3 Brain Organoids

The technology developed in Chapter 4 for culture and assessments of organoids was applied and validated specifically for forebrain organoids. This choice was motivated

by the existence of a close collaboration with Dr. Zhexing Wen at Emory University, whose lab works extensively with this region-specific brain organoid type. Here, an overview of brain organoid technology and its applications is described in order to provide context.

Brain organoids have exciting potential for studying human brain development and disease, as the human brain is particularly difficult to study. Studies of human brain development and disease have conventionally used medical imaging, post-mortem human brain samples, animal models, and *in vitro* two-dimensional (2D) cell cultures. Animal models, in particular, have yielded many important insights about brain development. However, many diseases are difficult to recapitulate in animal models, and the lack of human-specific physiology has limited translation of findings from animal models to the development of therapeutics[61]. Recent work has shown the ability both to generate brain[52] and brain region-specific[56,62,63] organoids. Brain organoids, also referred to as cerebral organoids, typically contain tissues characteristic of multiple regions of the brain, whereas brain region-specific organoids model only one region of the brain. Brain organoids have been used to study human brain development[62,64,65], differences in brain development across species[66], autism spectrum disorders[67], Zika virus infection[56], and microcephaly[52].

An early application of brain organoid technology was the use of cerebral organoids generated from patient-derived iPSCs to model microcephaly[52]. Although mutations in several genes have been implicated in this neurodevelopmental disorder, mouse mutants do not exhibit the same severe reduction in brain size that is seen in patients. Analysis of patient-derived organoids revealed premature neuronal

differentiation, suggesting this as a potential cause for the disease phenotype. This also demonstrated the feasibility of using cerebral organoid cultures for studying human neurodevelopment and disease. In a second example of brain organoid technology, Qian et al.[56] developed methods for generating region-specific organoids including forebrain, midbrain, and hindbrain. A key aspect of their method was the development of the SpinΩ bioreactor, a miniaturized spinning bioreactor in a 12-well tissue culture plate. The brain region-specific organoids and bioreactor technology were applied in studying mechanisms by which Zika virus infects brain tissue and produces phenotypes associated with microcephaly. These two brief examples illustrate how brain organoid models have enabled new studies of human development and disease. Overall, brain organoids show great promise in enabling new studies of the human brain and development of therapeutics. However, studies are still limited by challenges associated with culturing, handling, and reproducibly generating brain organoids. This thesis focuses on development of technologies that provide new abilities for culturing and handling brain organoids. These tools will broadly enable future studies focused on generating brain organoids more robustly and applying them in large-scale studies.

1.3 Microfluidic Approaches for Studying PSC Aggregates

Advances in microscale technologies have greatly facilitated the development of 3D cell culture systems. With fabrication techniques borrowed from the microelectronics industry, as well as newer technologies such as 3D printing, microfluidic devices can be rapidly designed and prototyped.[68-71] In a common method of fabrication known as soft lithography, a master mold is first made in a cleanroom, using photolithography to pattern features on a silicon wafer. Then, individual devices are cast from the mold in a

material such as polydimethylsiloxane (PDMS)[69] and are bonded to a glass slide to create enclosed channels. PDMS is commonly used for biological samples because it is biocompatible and optically transparent, facilitating imaging. The inherent features of microfluidics, including the small size scale that matches biological samples and the existence of low Reynolds number, laminar flow, enable enhanced control over soluble and physical aspects of cellular microenvironments. Additionally, microfluidics can increase experimental throughput via assay integration, parallelization, and automation. Together, these capabilities make microfluidics well-suited for engineering 3D culture systems.

1.3.1 Microfluidic Culture Methods for PSC Aggregates

A number of microfluidic approaches have been developed to address technological challenges associated with formation, manipulation, culture, and analysis of cell aggregates. Microfluidic methods for forming aggregates of defined size include seeding single cells in wells[72-75], traps[76], hanging drops[77-80], or droplets[81,82]. Other microscale technologies have been developed for culturing pre-formed aggregates in devices with wells or traps[83-87]. In these methods, device features are used to individually position cell aggregates, thereby preventing physical interactions among aggregates and enabling tracking at multiple time points during culture. Device designs that allow *in situ* imaging enable acquisition of phenotypic information to be collected during and following culture. Some methods have also been developed for manipulation and perturbation of individual aggregates, such as controlled pairing of aggregates[88]. A significant disadvantage of current microfluidic technologies is that platform designs are low-throughput, handling 20 samples or less, and are not inherently scalable.

Additionally, many trapping mechanisms physically constrain the aggregates, which can impart mechanical cues as the aggregates grow and increase in size during culture. Thus, there is still a need for microfluidic technologies that enable the culture of many individual PSC aggregates in controlled environments with the ability to perform longitudinal tracking and *in situ* imaging. This technological need will be addressed in Chapters 2 and 3 of this thesis.

1.3.2 Microfluidic Culture Methods for Organoids

Although many microscale technologies have been developed for handling cell aggregates, they have been relatively unexplored for the culture of organoids. One of the most significant challenges is handling organoid size changes. For example, brain organoids are a few hundred microns in size after formation but grow to a few millimeters in size after weeks to months in culture. Organoid growth, therefore, requires device features that range from the micro- to the meso-scale. In general, there are multiple ways in which miniaturized fluidic technologies can address the current challenges associated with organoid culture. Scaling down culture systems uses reduced media volumes and enables the multiplexing of conditions, making large-scale screens feasible. Fluidic flow can be leveraged to control spatial and temporal delivery of soluble molecules to define instructive cues that promote self-organization. Additionally, imaging-based assays can be performed *in situ* to facilitate live tracking of organogenesis. There are two key examples of technologies that have been developed for the culture of brain organoids. In the first, an array of micropillars was used to form brain organoids from single cells. Organoids were then embedded in Matrigel in the micropillar array and cultured[89]. In the second example, organoids were cultured in a central channel

embedded in Matrigel and two side channels were used to perfuse media and reagents[90,91]. Although both technologies were able to generate and culture cerebral organoids in a microfluidic device, neither device configuration is adaptable for screening, in which exposing subsets of organoids to different drugs, molecules, etc. is desired. Development of a microscale technology that provides the ability to reproducibly culture and screen individual organoids in controllable environments will help enable the use of organoids in studying human development and disease and in drug screening.

1.3.3 Considerations in Microfluidic Culture

The cell microenvironment is composed of biochemical factors such as nutrients and cell-secreted molecules, physical factors such as substrates for cell growth and fluid shear, and physicochemical factors such as oxygen, pH, and temperature. Microscale culture platforms can be designed to control these different aspects of the cell microenvironment. Some key examples are the use of microscale techniques for cell patterning[92], spatial[93,94] and temporal[95-97] variation of the soluble microenvironment, and for probing autocrine/paracrine signaling[98,99].

Specifically for controlling the soluble cell culture environment, there are a number of aspects that microfluidic techniques provide control over. First, the density of cells per volume of media is typically significantly increased in microscale culture. This provides the opportunity for concentrating biochemical factors such as cell-secreted molecules but also requires tuning of media exchange to provide sufficient nutrients and remove waste. Length scales and media perfusion rate can also be tuned to operate in diffusion or convection-dominated regimes for modulating aspects of the biochemical environment. One application of this is in studying roles that autocrine and paracrine

signaling play in cellular processes[100]. In designing a microfluidics-based cell culture system, these types of parameters need to be carefully considered in design and validation of the system. This topic will be discussed in greater detail in Chapter 3 of this thesis.

1.4 Thesis Objectives and Significance

As discussed, there are a number of technical challenges associated with current conventional and microfluidic platforms for culture and assessments of PSC aggregate cultures. The overall objective of this thesis was to develop microfluidics-based tools that enable culture of individual stem cell aggregates, provide spatiotemporal control over the culture environment, and enable *in situ*, imaging-based assessments of cell phenotypes. In Chapter 2, a microfluidic platform was developed for culture of small (< 500 μm) stem cell aggregates that provides the ability to isolate individual aggregates, track aggregates throughout culture and perform *in situ* imaging and immunocytochemical analysis. In Chapter 3, the same microfluidic platform was improved upon and used to investigate how key microfluidic culture parameters modulate differentiation of ESC aggregates to motor neurons. This work enhances understanding of how aspects of microfluidic culture influence cell growth and differentiation and informs design of future studies. Chapter 4 presents a miniaturized platform for culture and imaging-based assessments of forebrain organoids. This work combined modeling and experimental approaches to validate culture of organoids in the platform, establishing the platform as tool that can be broadly applied in future organoid studies and screens. Finally, Chapter 5 of this thesis provides overall conclusions and suggestions for future work.

CHAPTER 2 : A MICROFLUIDIC PLATFORM FOR LONGITUDINAL MONITORING AND MULTI-MODAL PHENOTYPIC ANALYSIS OF INDIVIDUAL STEM CELL AGGREGATES

This chapter is adapted from a research article entitled "A microfluidic trap array for longitudinal and multi-modal phenotypic analysis of individual stem cell aggregates" published in Lab on a Chip in 2017[2].

2.1 Introduction

Pluripotent stem cells (PSCs) have the ability to self-renew and differentiate to the three germ lineages.[3,4,101] In particular, when PSCs are cultured as three-dimensional (3D) cellular aggregates, they mimic many of the biochemical and biophysical interactions that occur during *in vivo* early embryonic development.[11,12] Efforts to direct stem cell aggregate morphogenesis have demonstrated that complex 3D tissue structures, termed "organoids", can be generated *in vitro*,[46] and that these tissues recapitulate many key features of native tissue structure and function.[48,52,102] Thus, the generation of PSC-derived tissue models has broad applications in studying mechanisms of tissue development, in disease modeling, and in drug screening.

Within the 3D stem cell culture microenvironment, both exogenous and endogenous biophysical and biochemical cues mediate cellular differentiation and morphogenesis. Maintaining uniformity of aspects of the culture microenvironment is important for standardizing differentiation and morphogenesis of cultures. For example, changes in aggregate size can influence differentiation by affecting diffusive transport of oxygen, nutrients, and morphogens.[103] In addition, modulating the frequency of media exchange or perfusion also affects delivery of biochemical cues to cells.[98,100,104,105]

Despite development of various strategies to improve uniformity of cell aggregate cultures, for example by controlling aggregate size,[17,19,106] a significant amount of heterogeneity often remains within cultures. It is unclear how factors such as biological stochasticity, environmental parameters, and experimental procedures each contribute to the heterogeneity, thus motivating the development of technologies that enhance the ability to standardize stem cell aggregate differentiation and morphogenesis by providing improved control of the 3D cellular microenvironment.

A variety of culture systems have been developed for stem cell aggregates. One category of these is batch-based methods, in which aggregates are cultured under static[5] or stirred[13,16,34] suspension conditions in petri dishes or larger vessels. Batch-based methods enable high-throughput culture (1,000s per experiment) and have been shown to improve uniformity in aggregate size, such as in stirred suspension cultures.[17] However, in batch systems, aggregates can physically interact with one another in a stochastic manner, which can contribute to heterogeneity in differentiation. An additional challenge associated with batch-based culture systems is the lack of ability to longitudinally observe and track individual samples throughout culture. Observation of differentiation and morphogenesis at multiple time points in the same samples is of interest, for example, in order to understand how processes evolve through time and to observe population heterogeneity. Culture platforms which physically isolate cell aggregates provide the ability to longitudinally monitor samples. Examples of such platforms include multiwell plates,[28,29] microwells,[18,30-32] droplets[107], and hanging drop[27] culture. However, with each of these methods, it is labor- and time-intensive to manipulate aggregates individually, to exchange media, and to apply chemical factors. In particular, studies that

require delivery of soluble factors with time scales on the order of seconds to hours are challenging. Additionally, high-resolution imaging, such as confocal microscopy, cannot be performed directly with these culture platforms for live and end-point imaging of sample phenotypes.

In contrast to macroscale culture systems, microfluidic-based platforms offer the ability to address challenges related to culture and handling individual cellular aggregates. Microfluidic systems provide spatiotemporal control over the culture microenvironment due to the nature of low Reynolds number flow and the ability to precisely control media exchange rates.[108] Additionally, microscale features can be designed to position and culture cellular aggregates within individual chambers. Finally, microfluidic devices made with traditional soft lithography techniques,[71] fabricated from polydimethylsiloxane (PDMS), and bonded to glass coverslips are compatible with high resolution microscopy for live imaging-based assessment of aggregate differentiation.

While previously a few microfluidic approaches for culturing cellular aggregates have been demonstrated, there are technical demands that these systems do not fully address. In one subset of approaches, aggregates are formed on-chip by seeding single cells in wells,[72-75] traps,[76] hanging drops,[77-80], or droplets[81], followed by culture of the resulting aggregates. Forming aggregates within devices allows for control of initial size, as with many off-chip methods, and circumvents the challenge of transferring pre-formed aggregates into devices. However, many of the methods that use microwells within microfluidics to form aggregates are not compatible with high-resolution imaging during culture, due to limitations of objective working distances through the device material. *In situ* imaging is typically desired to assess expression of fluorescent reporters in live

samples during culture. Additionally, having the ability to perform off-chip aggregate formation and pre-treatment steps is desired in many protocols, which these existing platforms do not currently possess. Examples of the utilities of this capability include formation of aggregates from multiple cell types, incorporation of microparticles within aggregates, and Matrigel embedding steps. Thus, a platform that is designed for loading of pre-formed aggregates has greater experimental flexibility and can be used more broadly. While previous work has shown the ability to load pre-formed aggregates into devices with wells or traps,[83-87] the majority of existing platforms are low-throughput, accommodating 20 samples or less, and are not inherently scalable (e.g. the fluidics required for trapping are not compact or the trapping mechanism is not deterministic). In addition, many existing platforms use trapping mechanisms that physically constrain aggregates, which in addition to limiting space for size increases during culture can also impose exogenous mechanical cues or induce diffusion limitations in traps.

In this chapter, we have created a culture platform for stem cell aggregates that satisfies the following criteria: can be deterministically loaded with pre-formed aggregates, allows aggregate growth over multiple days of culture without physically constraining aggregates, is compatible with high resolution live and end point imaging, and has a compact design that can be scaled up to increase higher throughput. We show that this microfluidic platform provides the ability to culture and perform multi-functional, on-chip phenotypic analyses of individual stem cell aggregates at high spatial density. This is facilitated by the abilities to deterministically trap individual pre-formed aggregates, easily exchange fluids, and couple devices directly with high-resolution microscopy. This platform also reduces heterogeneity in cultures in terms of aggregate

size and morphology. We envision applications of this technology in standardizing the generation of PSC-derived tissue models and in expanding abilities for phenotypic analysis.

2.2 Materials and Methods

2.2.1 Device Fabrication

Microfluidic devices were fabricated in polydimethylsiloxane (PDMS) (Dow Corning Sylgard 184, Midland, MI) by soft lithography.[71] Briefly, a master mold was fabricated by standard UV photolithography with the negative photoresist SU8-2100 (Microchem, Newton, MA) to create three layers of respective heights 200 μm, 100 μm, and 200 μm. Before PDMS molding, the master was treated with tridecafluoro-1,1,2,2-tetrahydrooctyl-1-trichlorosilane vapor (United Chemical Technologies, Bristol, PA) to allow release of the PDMS. To make devices, PDMS was mixed in a 10:1 ratio of pre-polymer and crosslinker, degassed to remove air bubbles, poured on the master mold, degassed a second time to remove remaining bubbles, and cured for 2 hours at 70 °C. Following curing, devices were cut and inlet and outlet holes for fluidic connections were punched with 18 gauge blunt needles (McMaster-Carr, Elmhurst, IL). Devices were then bonded onto glass coverslips by oxygen plasma bonding.

2.2.2 Mouse Embryonic Stem Cell Culture

Mouse ESCs (D3 cell line) were maintained in tissue culture-treated polystyrene dishes (Corning Inc., Corning, NY) coated with 0.1% gelatin (Millipore, EmbryoMax). Undifferentiated culture media consisted of Dulbecco's modified Eagle's medium (DMEM) (Mediatech, Herndon, VA) supplemented with 15% fetal bovine serum (Hyclone, Logan, UT), 100 U/mL penicillin, 100 μg/mL streptomycin, 0.25 μg/mL

amphotericin (Mediatech), 2 mM L-glutamine (Mediatech), 1x MEM non-essential amino acid solution (Mediatech), 0.1 mM 2-betamercaptoethanol (Fisher Scientific, Fairlawn, NJ), and 10^3 U/mL leukemia inhibitory factor (LIF) (ESGRO, Chemicon, Temecula, CA). Cells were passaged at approximately 70% confluence (typically every 2-3 days) and seeded at a density of 1 million cells for a 100 mm plate. Culture media was completely exchanged every other day.

2.2.3 Aggregate Formation and Culture

A single cell suspension of undifferentiated mESCs was obtained by dissociating monolayer cultures with 0.05% trypsin-EDTA (Mediatech). Aggregates were formed by centrifugation (200 rcf) of mESCs into 400 μm agarose (OmniPur®, EMD Millipore) microwells placed within a 6-well tissue culture polystyrene plate (Corning, Inc.).[106] To yield either 500 cell or 1000 cell aggregates, volumes of 1 mL or 2 mL, respectively, of the single cell suspension (concentration: 3 million cells/mL) were added to each well of the 6-well plate. Cells were incubated in the wells in culture media without LIF for approximately 18-24 hours to allow aggregates to form.

For batch suspension culture, following formation aggregates were cultured in 100 mm bacteriological grade polystyrene Petri dishes (BD, Franklin Lakes, NJ) with approximately 2000 aggregates per plate in 10 mL of culture media (without LIF). Plates were maintained on rotary orbital shakers (Benchmark Scientific, Edison, NJ) at a frequency of 45 rpm.[15,17] Media was exchanged every other day, with 90% of the media replenished with fresh media.

For multiwell culture, following formation aggregates were cultured in 96-well U-bottom multiwell plates (Corning). Plates were prepared by coating with 2% Pluronic

(ThermoFisher) for 1 hour to prevent cell attachment to the surface. To achieve one aggregate per well, aggregates were initially suspended in media without LIF at a concentration of 400 aggregates/mL and diluted twice (at 1:10 and 1:12.5) to yield a final concentration of 5 aggregates/mL before volumes of 200 µL were pipetted into each well. The final volume of each well was 200 µL, and no media exchange was performed for the duration of culture.

2.2.4 Device Loading and Operation

Prior to each experiment devices, fittings (blunt 16 gauge needles; McMaster-Carr), and tubing (1/32" ID silicone tubing; Cole Parmer) were sterilized by autoclaving. Devices were connected to a second identical device during operation to increase the overall fluidic resistance and thereby decrease the flow rate during loading. Prior to aggregate loading, devices were first primed with 70% ethanol using a syringe to remove air bubbles. Next, devices were rinsed with sterile phosphate-buffered saline (PBS) and then incubated with a 1 mg/ml bovine serum albumin (BSA; Millipore) solution for 30 minutes to passivate the surfaces.[73,109] A 200 µL pipette tip filled with cell culture medium was placed at the device inlet for aggregate loading and perfusion. Aggregates were collected and resuspended at a concentration of approximately 600 aggregates/mL in a solution of 1.05 g/mL Percoll (Sigma Aldrich) in phosphate-buffered saline (PBS) to prevent rapid settling. Then, aggregates were pipetted into the inlet and loaded into devices via gravity-driven flow. Once aggregates were loaded, device outlets were connected to a syringe pump (PHD 2000; Harvard Apparatus), and the entire setup was placed in a humidified incubator (HERAcell 240i, Thermo Scientific). During culture, devices were continuously perfused at a defined flow rate by withdrawing culture media

without LIF from a 200 µL pipette tip reservoir at the inlet. Additionally, devices were kept in a shallow, sterile water bath to limit evaporation. Phase contrast images of loaded devices were acquired using an EVOS microscope (LifeTechnologies).

2.2.5 LIVE/DEAD Assay

A LIVE/DEAD assay (Invitrogen) was performed to evaluate cell viability at day 4 of differentiation. For aggregates cultured in devices, all steps were performed in devices. For aggregates cultured in batch suspension culture, all steps were performed in 1.5 mL microcentrifuge tubes. Aggregates were rinsed with PBS and then incubated with 2 µM calcein AM and 4 µM Ethidium-D in PBS with calcium and magnesium for 45 minutes. Samples were imaged on a confocal microscope (Zeiss LSM 700 Confocal Microscope). Device samples were imaged in devices; batch suspension culture samples were transferred to glass-bottom 24-well plates (MatTek Corporation) for imaging. Z stacks were acquired up to a depth of approximately 50 µm with a spacing of 3 µm.

2.2.6 Immunofluorescent Staining and Imaging

Immunofluorescent staining was performed in devices by perfusing all solutions through the pipette tip inlets by gravity-driven flow. For aggregates cultured in batch suspension, all steps were performed in 1.5 mL microcentrifuge tubes, and samples were continuously rotated on a tube rotator. For multiwell culture, all steps were performed in multiwell plates. First, samples were washed with PBS and fixed in 10% formalin at room temperature for 40 minutes. Following a wash in block buffer (2% BSA, 0.1% Tween 20, in PBS), samples were permeabilized in 1.5% Triton X 100 in PBS for 30 minutes. After washing in serum block buffer (2% donkey serum, 0.1% Tween 20, in PBS) for 30 minutes, samples were incubated overnight at room temperature in the

primary antibody solution (1:200 Santa Cruz Biotechnology Oct-3/4 (N-19): sc-8628 in serum block buffer). The next day, samples were washed in serum block buffer for 30 minutes and then incubated in the secondary antibody solution (1:200 AlexaFluor®546 donkey anti-goat) at room temperature for 4 hours. For the final 15 minutes of incubation, nuclear stain Hoechst 3342 was added (final concentration: 10 µg/mL). Samples were washed a final time with serum block buffer for 30 minutes, stored overnight at 4^0 C, and imaged the next day. Device samples were imaged in devices; batch suspension culture samples were transferred to glass-bottom 24-well plates (MatTek Corporation) for imaging. Samples were imaged on a confocal microscope (Zeiss LSM 700 Confocal Microscope) with a 20x objective. Z stacks were acquired up to a depth of 30 µm with spacings of 3-5 µm. For larger aggregates that did not fit in a single field of view, 2x2 tile scan images with 10% overlap were acquired and stitched together with the microscope software (ZEN, Zeiss).

2.2.7 Fluorescent Image Analysis

For each aggregate, a single two-channel z slice approximately 15 µm in from the surface was analyzed using custom-written MATLAB code. The two-channel image was separated into individual single-channel images, corresponding to the nuclear stain (Hoechst) and Oct4 antibody staining. As Oct4 is localized to the cell nucleus, we segmented nuclei in order to quantify Oct4 expression for each cell. To segment the nuclei, we used a modified version of a method developed by Lou, et al[110]. Starting from the greyscale nuclear stain image, contrast adjustment was performed as a preprocessing step. Next, we applied a Gaussian filter to the image, calculated the Hessian matrix of the resulting image, and calculated the first eigenvalue of the Hessian matrix. Then, a

threshold was applied to the first eigenvalue of the Hessian matrix to eliminate dim pixel values that would otherwise result in poor segmentation. The resulting image was used as a mask to segment the contrast adjusted greyscale nuclei image. This typically yielded slightly under-segmented nuclei, so a watershed transform was applied to the masked greyscale nuclei to yield a final, binary image of segmented nuclei. The image of segmented nuclei was then used to identify and segment nuclei in both the nuclear and Oct4 individual greyscale images.

To quantify Oct4 expression for each cell, the mean Oct4 pixel intensity was calculated and normalized by the mean Hoechst pixel intensity for the same cell. This yielded a metric for cellular Oct4 expression (Ratio of Oct4/Hoechst). To obtain a metric for mean Oct4 expression for a single aggregate (Ratio of Oct4/Hoechst), the cellular metric was averaged for all cells in the aggregate.

The coefficient of variation (CV) was used to describe the heterogeneity in Oct4 expression among cells within a single aggregate or among aggregates within a culture platform. In the former case, the CV was defined as the standard deviation in cellular Oct4 expression for a given aggregate, divided by the mean value for all cells in that aggregate. In the latter case, the CV was defined as the standard deviation in aggregate Oct4 expression for all aggregates in a given culture platform, divided by the mean value for all aggregates.

2.2.8 Aggregate Size and Growth Rate Analysis

Aggregate sizes were quantified from phase contrast images. Images were manually segmented in ImageJ and the cross sectional area of each aggregate was

measured. The aggregate radius was calculated from the cross sectional area, assuming each cross section to be circular and using the formula:

$$radius = \sqrt{\frac{area}{\pi}}$$

Growth rate was defined as change in radius between D1 and D4, normalized by the initial radius. This metric was calculated on a population-averaged basis, e.g.

$$Growth\ rate_{device\ 1} = \frac{mean\ D1\ radius_{device\ 1} - mean\ D4\ radius_{device\ 1}}{mean\ D1\ radius_{device\ 1}}$$

This was calculated on a population averaged basis due to the inability to measure the size of a single batch aggregate on both D1 and D4.

2.2.9 Peclet Number Calculation

We calculated the Peclet number (Pe) using the equation $Pe = \frac{Lv}{D}$ where L is the characteristic length, v is the fluid velocity, and D is the diffusion coefficient. We assumed L to be the width of the main channel (300 μm). We calculated v ~ 30 μm/s using the relationship $v = \frac{Q}{A}$ where Q is the volumetric flow rate through the device (10 μL/hr) and A is the cross-sectional area of the main channel ((300 μm)^2). We assumed D ~ 10^{-6} cm^2/s for a small molecule.[111] Using these values yielded Pe ~ 90.

2.2.10 Statistical Analysis

Experiments with replicate data are represented as the mean +/- standard deviation. Sample sizes (n) and number of independent experiments are detailed in the corresponding figure legends. Statistical analyses were performed using GraphPad Prism software. Statistical tests were performed using either a Mann-Whitney U test or non-parametric one-way ANOVA (with Kruskal-Wallis) combined with Dunn's multiple

comparison's test for comparison of individual samples. P values less than 0.05 were considered significant.

2.3 Results and Discussion

2.3.1 Design of the Microfluidic Device

The design of the microfluidic device consists of an array of 105 traps for culture of individual aggregates (**Figure 2.1**). Although the master is a multi-layer master, the devices can be fabricated using a standard single-layer PDMS micromolding process. The traps are connected by a main channel for aggregate loading and perfusion of media and reagents. Loading of individual aggregates into traps is accomplished by a previously demonstrated hydrodynamic loading mechanism[112-114] that is dependent on the ratio of two flow paths in the device (**Figure 2.1e**). Briefly, the presence of a resistance channel at the back of each trap creates a secondary flow path that directs aggregates into traps. Once an aggregate enters a trap it blocks most of the flow to that trap so that subsequent aggregates preferentially continue to flow down the main channel and enter subsequent traps. Isolating individual aggregates in separate traps has a number of advantages, namely, preventing physical interactions between aggregates and enabling longitudinal tracking of individual aggregates during culture.

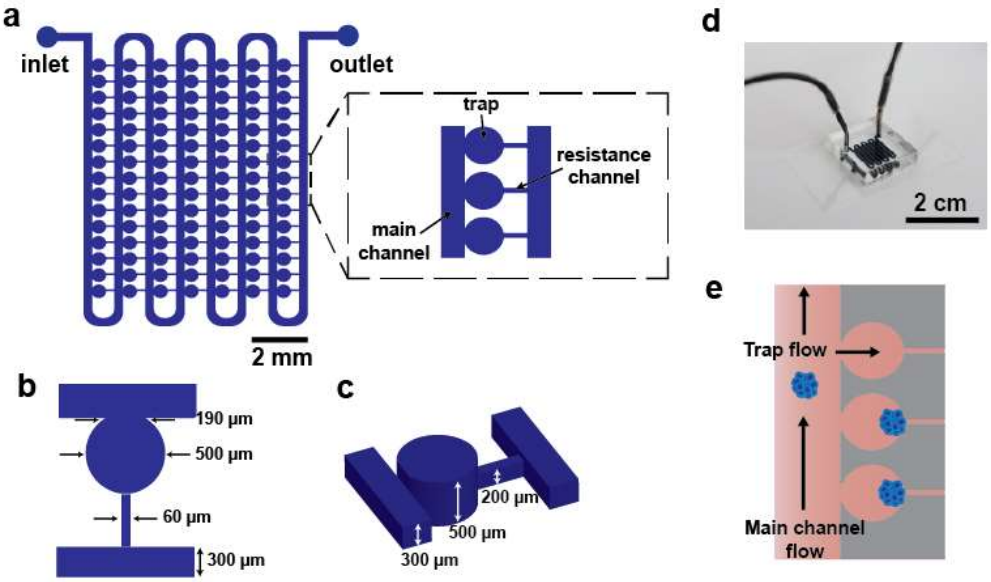

Figure 2.1. Overview of microfluidic platform. a) Schematics illustrate the design of the device, with inset detailing the main channel, trap, and resistance channel. b,c) Diagrams show key device geometrical features. d) Photograph of a dye-filled device. e) Image shows the hydrodynamic loading mechanism, which is dependent on the balance of flow through the main channel versus flow through the traps and resistance channels.

Designing a device that allows for both initial loading of aggregates and subsequent culture of aggregates with significant size changes presents an engineering challenge. For reproducible loading of single aggregates in individual traps, there are two primary design requirements. First, the dimensions of the resistance channels must be small enough such that aggregates are not able to pass through the resistance channels during loading. To address this, we designed the resistance channel width (60 µm, **Figure 2.1b**) to be less than half of the average diameter (~160 µm) of aggregates used for this study. Second, the relative fluidic resistances of the two flow paths in the device must be properly balanced for efficient loading of traps.[112,113] If flow through the traps and resistance channels is too low (fluidic resistance is too high), then few aggregates will be trapped; however, if the flow is too high then multiple aggregates will accumulate within

traps, also resulting in inefficient trapping. These requirements were balanced in the final device dimensions (**Figure 2.1b,c**). We found that a ratio of trap to main channel resistance of ~20 resulted in good loading. To address the challenge of designing a device that physically accommodates growing aggregates over multiple days of culture, a pinched-off circular trap geometry was used (**Figure 2.1b,c**). The trap dimensions (500 μm width and height) allow for initial loading of relatively small aggregates (< 190 μm in diameter) without constricting growing aggregates over time (up to a maximum diameter of 500 μm).

2.3.2 Device Operation and Validation

To demonstrate the capabilities of our platform for aggregate culture, we differentiated aggregates by removing LIF from the culture media. Aggregates were pre-formed in microwells (D0) and then loaded into devices the following day (D1) (**Figure 2.2a**). For comparison, aggregates were also differentiated in batch suspension culture. When devices were loaded, typically ~50% of traps were loaded with single aggregates, with the remaining traps containing no or multiple aggregates. We observed that multiple aggregate loading often occurred when clumps of aggregates entered a trap together, or when the first aggregate to enter a trap did not block the restriction channel before a second aggregate entered. The loading efficiency of this device reflects the tradeoff of scaling the traps to be small to allow effective loading and scaling to be large so that they can allow the aggregate size changes of up to five-fold over the course of culture. This is a unique challenge, in contrast to examples of previous work that trap objects such as cells and embryos, which do not grow bigger during the course of experiment and thus can be loaded using traps that fit tightly around the object. In our case, the criterion of not

constraining aggregates within traps means that the deterministic loading mechanism results in an unavoidable imperfect loading efficiency. To compensate for the 50% loading efficiency, one could simply scale up the number of traps to increase the number of successful samples, which is well within experimental control. A scaled-up device would occupy a larger footprint, but there are no inherent design or operational challenges inherent to scaling up the platform other than making larger masters.

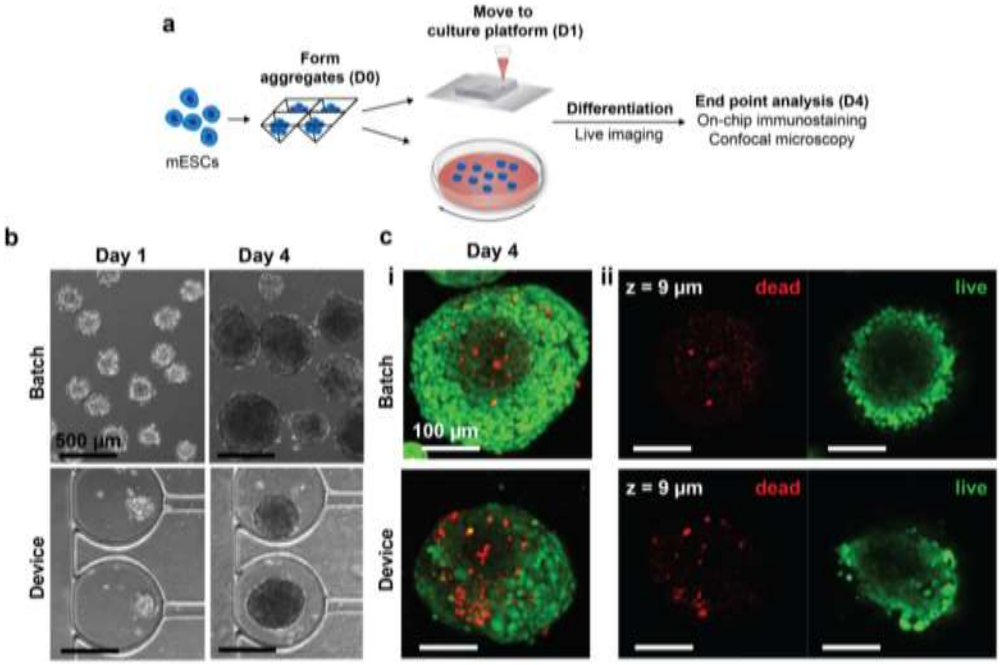

Figure 2.2. Validation of device culture. a) Experimental design. b) Phase contrast images show representative aggregates at days 1 and 4 of differentiation. c) Representative confocal images of day 4 aggregates treated with a LIVE/DEAD stain (live cells: green, dead cells: red); (i) Maximum projection images; (ii) single channel z planes.

Aggregates remained trapped over multiple days of culture, as seen in the representative phase contrast images (**Figure 2.2b**). Importantly, aggregates maintained a three-dimensional, spherical morphology during device culture, comparable to that of batch suspension culture, as opposed to plating down on the glass surface and forming morphologies resembling monolayer culture. In further support of the notion of little to

no cell adhesion to the glass culture surface, we observe that day 4 aggregates can move within the device under flow perturbations. Devices were continuously perfused at a flow rate of 10μL/hr, which was approximately equivalent to exchanging the volume of the device once per hour. This flow rate was chosen as it was comparable to the media exchange rate of batch suspension culture on the basis of volume of media per aggregate per time. To confirm that this perfusion rate supported cell viability aggregates were treated with a LIVE/DEAD stain. Representative confocal microscopy images (**Figure 2.2c**; **Appendix A.2**) demonstrated that there was high viability and minimal cell death in aggregates cultured in devices for 4 days and that viability was comparable to that of batch culture.

2.3.3 Growth and size control

A disadvantage of batch-based aggregate culture methods is that samples can physically interact with one another, which introduces a source of heterogeneity into cultures. We hypothesized that culture of aggregates in individual traps would maintain better uniformity compared to batch suspension culture in aspects such as size and morphology by preventing physical interactions between multiple aggregates. To assess how device culture impacted aggregate morphology and size during differentiation, phase contrast images of aggregates were acquired at day 1 (immediately following loading) and day 4 of differentiation, and the batch and on-chip cultures were compared (**Figure 2.3a**). In batch cultures at day 4, a variety of aggregate sizes and morphologies were observed. The presence of small aggregates in the cultures (comparable to day 1 sizes) was likely the result of single cells shedding off from aggregates and forming new, smaller aggregates (**Figure 2.3a**, indicated by red arrows). Aggregates with budding

morphologies, i.e. aggregates with small, spherical protrusions, were also observed in batch cultures **Figure 2.3a**, indicated by white arrows). In contrast, aggregate sizes were more uniform and the budding morphology was observed less frequently in device cultures.

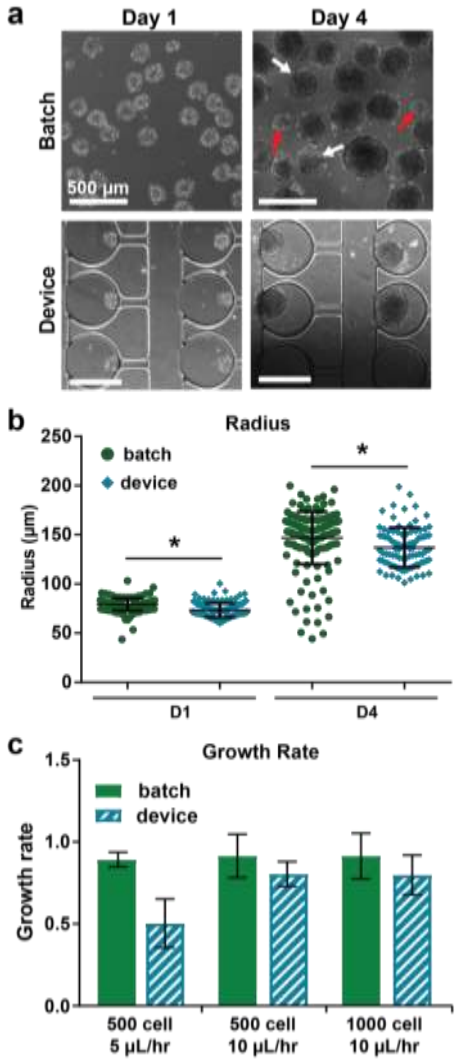

Figure 2.3. Device culture reduces variability in aggregate size. a) Phase contrast images showing size and morphology at days 1 and 4. Red arrows indicate subpopulations of much smaller aggregates. White arrows indicate aggregates with budding morphologies. b) Aggregate radii were quantified from phase contrast images at day 1 (before loading into devices) and day 4 of differentiation. Two independent samples are shown for each condition, with $n \geq 80$ aggregates for batch and $n \geq 40$ aggregates for devices. * $P < 0.0001$. c) Aggregate growth rates for different starting sizes and device perfusion rates.

Growth rate was defined as change in size between days 1 and 4, normalized by initial size. $n \geq 2$ batch samples or devices, respectively, per condition. All samples: n.s.

Aggregate size was quantified from the phase contrast images. At day 4, the mean size was similar for batch and device cultures, but there was a subpopulation of smaller aggregates present in the batch cultures, consistent with qualitative assessments (**Figure 2.3b**). The size distribution of aggregates was significantly larger for batch culture compared to device culturing, demonstrating the utility of the microfluidic platform for controlling aggregate size. It was also observed that device culture better controlled aggregate size compared to batch for different initial sizes of aggregates (500 cell starting size) (**Appendix A.3**).

Previous work has shown that microfluidic perfusion culture can modulate the soluble microenvironment, thereby affecting cell phenotype.[100] To characterize basic characteristics of the soluble environment, we calculated the Peclet number and found it to be ~90, suggesting that the platform operated under a convection-dominated regime. Based on the perfusion rate used, soluble molecules secreted by cells likely had a short enough residence time (~ minutes) to have a minimal effect on aggregates in neighboring traps. Additionally, it is possible that an aggregate's position within a device (i.e. closer to the inlet versus outlet) could have an impact on its phenotype. From the size data, however, there was no evidence that aggregate phenotypes differed depending on position in the device (**Appendix A.3c-e and A.5a-b**).

We compared the growth rate of aggregates cultured in devices to those maintained in batch culture. The metric for growth rate was defined as the change in average radii between days 1 and 4 of culture, normalized by the initial radii. We found that there was no significant difference in growth rate for aggregates cultured in devices,

compared to batch, for two different starting sizes of aggregates (500 cell and 1000 cell) and at a device perfusion rate of 10 µL/hr (**Figure 2.3c**). From this, we conclude that at these parameters, aggregates receive sufficient nutrients and grow comparably. Interestingly, aggregates cultured at a perfusion rate of 5 µL/hr exhibited a noticeably lower growth rate than batch (although not statistically significant as a result of low sample numbers) (**Figure 2.3c**). Importantly, we did not observe significant differences in viability for this condition (**Appendix A.2**), suggesting that the reduced growth rate in devices could be due to limited mass transfer of nutrients. For this reason, the following experiments were conducted at 10 µL/hr perfusion.

2.3.4 On-chip immunofluorescent staining and imaging analysis

To demonstrate the utility of our microfluidic platform for performing various phenotypic assays on-chip in conjunction with multi-day culture, we fixed and immunofluorescently stained aggregates at day 4 of differentiation (**Figure 2.4**).

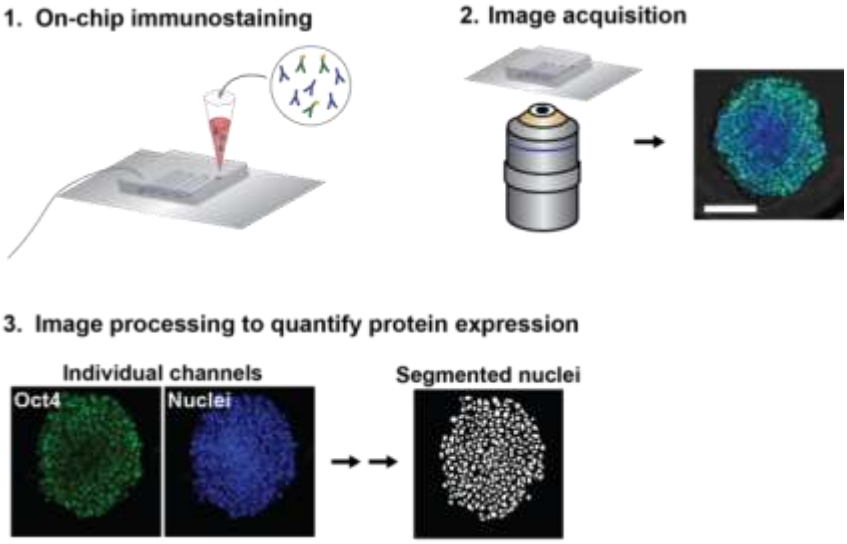

Figure 2.4. On-chip immunostaining and quantification of protein expression. (1) Immunostaining is performed on-chip by perfusing all reagents through the device via gravity-driven flow. (2) Confocal microscopy is used to image samples. (3) Image processing is used to quantify single-cell level protein expression within aggregates.

We examined expression of the pluripotency marker Oct4, which is highly expressed in pluripotent stem cells and decreases in expression over the first week of undirected aggregate differentiation.[115] Oct4 expression was quantified in day 4 aggregates cultured in devices, batch, or round bottom 96-well multiwell plates[116] (**Figure 2.5**). We performed a multiwell culture condition in order to compare on-chip differentiation to a platform where aggregates are also physically isolated. We hypothesized that the differences we saw in size and morphology between aggregates cultured in devices versus batch may manifest in differences in Oct4 expression. However, similar expression levels were observed across the three conditions. Aggregates cultured in devices had slightly higher Oct4 expression levels than both batch and multiwell culture formats (**Figure 2.5b**, **Appendix A.5e**). Although aggregate size can play a role in phenotype and rate of differentiation,[18-20,33] we did not find a correlation between Oct4 expression and aggregate size (**Appendix A.5a-c**). This data suggests that microfluidic culture can be leveraged to modulate aggregate differentiation, in this case, by maintaining pluripotency of aggregates at a higher level following LIF removal from the media. Previous work has demonstrated that microfluidic perfusion modulates the residence time of soluble secreted factors in the cellular microenvironment,[99] and this may play a role in promoting pluripotency, although the specific mechanism in this case is unknown.

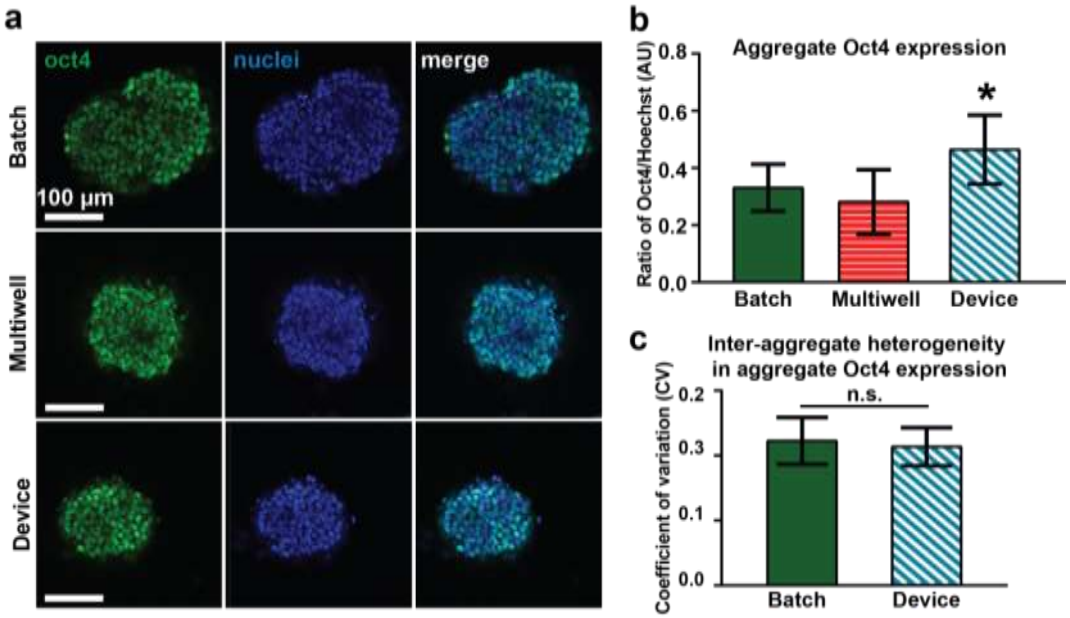

Figure 2.5. Device facilitates studying individual sample phenotypes. a) Representative immunostaining images. b) Mean aggregate Oct4 expression for different culture platforms. Two independent experiments are shown for batch and device conditions ($n \geq 25$ each) and one experiment is shown for multiwell condition ($n = 8$). * $P < 0.00001$ vs. batch and $P < 0.0001$ vs. multiwell. c) Inter-aggregate heterogeneity in Oct4 expression for device and batch cultures.

Next, we calculated the coefficient of variation of Oct4 expression to examine inter- and intra-aggregate heterogeneity in expression levels, across a given culture platform (**Figure 2.5c, Appendix A.5f**). There were no significant differences in inter-aggregate heterogeneity (**Figure 2.5c**), suggesting that each of the culture platforms perform equally well in this particular respect. However, there were subtle differences in intra-aggregate heterogeneity, indicating that there was more diversity in the Oct4 expression levels among cells of a single aggregate in device samples. Although these studies focused on a limited number of parameters to assess cell phenotypes, we anticipate that future studies will be valuable to assess how microfluidic culture modulates heterogeneity in terms of phenotypes seen during early differentiation beyond size.

2.4 Conclusions

Here we present the development of a microfluidic platform for culture, longitudinal tracking, and imaging of stem cell aggregates. Physical isolation of individual aggregates in individual traps prevents aggregate-aggregate interactions that contribute to heterogeneity in cultures and also enables correlation of live imaging and end point assay phenotypic information. Culture of aggregates in a high-density array format permits culture and analysis of ~50 samples at once, and this platform can be readily scaled up or parallelized to increase throughput. Finally, the design of the device permits high-resolution imaging for assessment of sample phenotypes, including incorporating techniques such as tissue clearing and multiphoton microscopy to image through denser, larger tissue constructs. Due to these combined capabilities, we anticipate that this platform can be applied for the generation of stem cell derived microtissues for drug screening and mechanistic studies of stem cell differentiation and tissue morphogenesis. Future applications are not limited to stem cells, and this platform could readily be applied to studying other cell aggregate systems, such as tumor spheroids. With the combined advantages of standardizing the culture environment and enabling single sample level analysis, we envision this platform as a tool in generating PSC aggregate derived cell and tissue models.

CHAPTER 3 : MODULATION OF MOTOR NEURON DIFFERENTIATION OF STEM CELL AGGREGATES USING MICROFLUIDIC PERFUSION

This chapter applies the microfluidic technology developed in Chapter 2, with the objective of exploring how microfluidic culture parameters influence stem cell aggregate behavior and differentiation. Experimental studies and transport modeling were used to assess how media exchange frequency and device geometries modulate the biochemical microenvironment, including availability of exogenous and cell-secreted molecules, and thereby impact differentiation. These studies were done in the context of differentiation of mESCs to progenitor motor neurons.

3.1 Introduction

Chapter 2 demonstrated a microfluidic device that provides the ability to culture, perturb, and observe individual stem cell aggregates[2]. This platform has wide applicability for studying mechanisms of stem cell differentiation, generating stem cell derived tissue models for drug screening, and developing methods for generating therapeutically relevant populations of cells. However, exploring any of these applications requires an understanding of how microfluidic culture conditions impact cell behavior and differentiation. Conventional cell culture techniques cannot directly be applied to the microscale, as microscale culture varies from macroscale culture in ways that can critically affect cell behavior.

One key difference in microscale culture is that the density of cells per volume of media is much higher, and this is particularly true for cell aggregates. This requires

careful consideration of the method and frequency with which media exchange is performed, so that there is sufficient delivery of nutrients and removal of waste. Approaches to considering media exchange in microfluidics have been discussed by Przybyla and Voldman[100], Young and Beebe[117], and others[118]. One method of choosing a media exchange interval or rate is to match volumes typical of bulk culture conditions (e.g. ~50-500 pL/h/cell for ESCs)[100]. A second method is to consider reaction and diffusion time scales of nutrient consumption and apply scaling arguments, such as with the effective culture time (ECT) and critical perfusion rate (CPR) described by Young and Beebe[117]. Regardless of the method used to estimate the required media exchange time scale, experimental validation is typically required depending on the specific cell type and microfluidic device configuration.

Media can be exchanged either by continuous perfusion or at defined intervals. The former strategy has been used as a way to regulate diffusible cell signaling and investigate its role in regulating cell behaviors[98,99]. For example, autocrine and paracrine signaling are known to play important roles in stem cell self-renewal[119,120], growth[121,122], and differentiation[123]. Previous work using microfluidic perfusion based approaches has shown that cell-secreted signaling is critical for maintenance of mESC pluripotency[99]. In contrast, periodic medium delivery, as opposed to continuous perfusion, has been shown to be an effective method for supporting cell growth and differentiation[124,125]. Giobbe, et al. showed that in the context of hiPSC microfluidic culture, discontinuous media perfusion resulted in more homogenous colonies[126]. Furthermore, for differentiation towards each of the germ lineages, different discontinuous perfusion rates were found to be optimal. It has been shown that higher accumulation of cell-secreted factors promoted

ectoderm and endoderm differentiation versus mesoderm, in contexts of spontaneous differentiation[124,126].

Given this previous work, the objective of this chapter was to explore key parameters in microfluidic culture of stem cell aggregates and understand how these parameters influence stem cell behavior and differentiation. These studies were done in the context of differentiation of embryonic stem cells (ESCs) to motor neurons (MNs). This differentiation protocol was chosen because it is well-established[35], MNs are a therapeutically relevant cell type, and there is evidence for roles of cell-secreted signaling in promoting differentiation[39,40,127]. Specifically, an approach coupling experimental studies and transport modeling was used to assess how media exchange frequency and device geometries modulate the biochemical microenvironment, including availability of exogenous factors (e.g., nutrients, small molecule additives) and cell-secreted molecules, and thereby impact differentiation. The results of these studies demonstrate that discontinuous perfusion is effective at supporting stem cell aggregate growth, in agreement with previous work with two-dimensional cultures. We find that there is a balance between the frequency of media exchange, which is needed to ensure that cells are not nutrient-limited, and the need to allow accumulation of cell-secreted factors to promote differentiation. Finally, we find that microfluidic device geometries can be exploited as a tool to expose aggregates to gradients of cell-secreted factors and promote asymmetric differentiation patterns.

3.2 Materials and Methods

3.2.1 Device Fabrication

Microfluidic devices were fabricated in polydimethylsiloxane (PDMS) (Dow Corning Sylgard 184, Midland, MI) by soft lithography.[71] Briefly, a master mold was fabricated by standard UV photolithography with the negative photoresist SU8-2100 (Microchem, Newton, MA) to create three layers of respective heights 200 μm, 100 μm, and 200 μm. Before PDMS molding, the master was treated with tridecafluoro-1,1,2,2-tetrahydrooctyl-1-trichlorosilane vapor (United Chemical Technologies, Bristol, PA) to allow release of the PDMS. To make devices, PDMS was mixed in a 10:1 ratio of pre-polymer and crosslinker, degassed to remove air bubbles, poured on the master mold, degassed a second time to remove remaining bubbles, and cured for 2 hours at 70 °C. Following curing, devices were cut and inlet and outlet holes for fluidic connections were punched with 18 gauge blunt needles (McMaster-Carr, Elmhurst, IL). Devices were then bonded onto glass coverslips by oxygen plasma bonding.

3.2.2 mESC Culture

G-Olig2 mESCs were obtained from ATCC® (ATCC SCRC-1037). These cells have green fluorescent protein (GFP) inserted into the gene for Olig2. Cells were maintained in tissue culture-treated polystyrene dishes (Corning Inc., Corning, NY) coated with 0.1% gelatin (Millipore, EmbryoMax). Undifferentiated culture media consisted of Dulbecco's modified Eagle's medium (DMEM) (Mediatech, Herndon, VA) supplemented with 15% fetal bovine serum (Hyclone, Logan, UT), 100 U/mL penicillin, 100 μg/mL streptomycin, 0.25 μg/mL amphotericin (Mediatech), 2 mM L-glutamine (Mediatech), 1x MEM non-essential amino acid solution (Mediatech), 0.1 mM 2-

betamercaptoethanol (Fisher Scientific, Fairlawn, NJ), and 10^3 U/mL leukemia inhibitory factor (LIF) (ESGRO, Chemicon, Temecula, CA). Cells were passaged at approximately 70% confluence (typically every 2-3 days) and seeded at a density of 1 million cells for a 100 mm plate. Culture media was completely exchanged every other day.

3.2.3 Motor Neuron Differentiation of mESC Aggregates

A single cell suspension of undifferentiated mESCs was obtained by dissociating monolayer cultures with 0.05% trypsin-EDTA (Mediatech). Cells were resuspended in basal differentiation media that consisted of Dulbecco's modified Eagle's medium/nutrient mixture F-12 (DMEM/F12) (ThermoFisher Scientific) supplemented with 5% Knockout Serum Replacement (ThermoFisher Scientific), 1x Insulin-Transferrin-Selenium solution (ITS) (ThermoFisher Scientific), 1x MEM non-essential amino acid solution (Mediatech), 0.1 mM 2-betamercaptoethanol (Fisher Scientific, Fairlawn, NJ), 5 μM thymidine (Sigma-Aldrich), and 15 μM each of adenosine, cytosine, guanosine, and uridine (Sigma-Aldrich)[35].

Aggregates were formed by centrifugation (200 rcf) of mESCs into 400 μm agarose (OmniPur®, EMD Millipore) microwells placed within a 12-well tissue culture polystyrene plate (Corning, Inc.).[106] To yield 1000 cell aggregates, volumes of 0.5 mL of the single cell suspension (concentration: 2.4 million cells/mL) were added to each well of the 12-well plate. Cells were incubated in the wells in culture media for approximately 18-24 hours to allow aggregates to form. Following formation, on day 1 aggregates were transferred either to microfluidic devices or Petri dishes. Starting on day 2, media was supplemented with 1.5 – 3.0 μM Purpmorphamine (Pur) (Calciobiochem) and 2 – 6 μM Retinoic Acid (RA) (Sigma-Aldrich).

For batch suspension culture, aggregates were cultured in 100 mm bacteriological grade polystyrene Petri dishes (BD, Franklin Lakes, NJ) with approximately 2000 aggregates per plate in 10 mL of basal differentiation. Plates were maintained on rotary orbital shakers (Benchmark Scientific, Edison, NJ) at a frequency of 45 rpm.[15,17] Media was exchanged every other day, with 90% of the media replenished with fresh media. RA and Pur were supplemented starting at day 2 and with each additional media change.

3.2.4 Device Loading and Operation

Prior to each experiment all devices and tubing connections were sterilized by autoclaving. Components that could not be autoclaved were either purchased sterile or sterilized by ethylene oxide gas treatment. Devices were assembled with a 14 gauge dispensing tip with luer lock connection (McMaster-Carr) at the inlet. For priming devices with a syringe, a piece of silicone tubing (1/32" ID silicone tubing; Cole Parmer) was connected to the inlet using 18 gauge polypropylene dispensing needles (McMaster-Carr). For culture, a sterile 3 mL syringe (Becton Dickinson) with plunger removed was screwed onto the inlet to serve as media reservoir. At the device outlet, a blunt 16 gauge needle (McMaster-Carr) was connected to a length of silicone tubing. A pinch valve was placed on this tubing to allow pressurization of devices to remove bubbles. The silicone tubing was connected to a luer lock two-way stop cock (McMaster-Carr) using polypropylene needles, and then to an additional length of silicone tubing. Finally, a 0.2 μm syringe filter (VWR) was connected to the end of the outlet tubing with a polypropylene needle to provide a sterile barrier.

Prior to aggregate loading, devices were first primed with 70% ethanol using a syringe to remove air bubbles. Next, devices were rinsed with sterile phosphate-buffered

saline (PBS) and then incubated with a 1 mg/ml bovine serum albumin (BSA; Millipore) solution for 30 minutes to passivate the surfaces.[73,109] Finally, devices were rinsed with basal differentiation media. Aggregates were collected and resuspended at a concentration of approximately 600 aggregates/mL in a solution of 1.05 g/mL Percoll (Sigma Aldrich) in phosphate-buffered saline (PBS) to prevent rapid settling. Then, aggregates were pipetted into the inlet and loaded into devices via gravity-driven flow. Once aggregates were loaded, sterile gas permeable adhesive membranes were used to seal device inlets ("Breathe-Easier", Electron Microscopy Services). Device outlets were connected to a syringe pump (PHD 2000; Harvard Apparatus) and the entire setup was placed in a humidified incubator (HERAcell 240i, Thermo Scientific). During culture, devices were kept in a shallow, sterile water bath to limit evaporation. Devices were perfused at a defined flow rate and frequency by withdrawing differentiation media from a reservoir at the device inlet using the syringe pump. For continuous media perfusion conditions, media was withdrawn at a constant flow rate. For discontinuous media perfusion, media was completely exchanged within the device at defined time intervals.

3.2.5 Immunofluorescent Staining

Immunofluorescent staining was performed in devices by perfusing all solutions through the pipette tip inlets by gravity-driven flow. For aggregates cultured in batch suspension, all steps were performed in 1.5 mL microcentrifuge tubes, and samples were continuously rotated on a tube rotator. First, samples were washed with PBS and fixed in 10% formalin at room temperature for 40 minutes. Following a wash in block buffer (2% BSA, 0.1% Tween 20, in PBS), samples were permeabilized in 1.5% Triton X 100 in PBS for 30 minutes. After washing in serum block buffer (2% goat serum, 0.1% Tween

20, in PBS) for 30 minutes, samples were incubated overnight at room temperature in the primary antibody solution: 1:20 Hb9 (81.5C10 from Developmental Studies Hybridoma Band) in block buffer or 1:5 Nkx2.2 (74.5A5 from Developmental Studies Hybridoma Band) in block buffer. The next day, samples were washed in serum block buffer for 30 minutes and then incubated in the secondary antibody solution (1:200 AlexaFluor®647 goat anti-mouse) at room temperature for 4 hours. Samples were washed a final time with serum block buffer for 30 minutes and imaged immediately. Device samples were imaged in devices; batch suspension culture samples were transferred to glass-bottom 24-well plates (MatTek Corporation) for imaging.

3.2.6 Confocal Microscopy

Samples were imaged on a confocal microscope (Zeiss LSM 700 Confocal Microscope) with a 20x objective. Z stacks were acquired to a depth of ~50 μm with spacings of 5 or 10 μm. For larger aggregates that did not fit in a single field of view, 2x2 tile scan images with 10% overlap were acquired and stitched together with the microscope software (ZEN, Zeiss). For live imaging in devices, device inlets were sealed with luer lock caps (McMaster-Carr) to maintain sterility.

3.2.7 Image Analysis

Confocal images from live and immunostained samples were quantified using custom-written MATLAB code. For each aggregate, 5 slices with 10 μm spacing were analyzed. Aggregates were first segmented manually from transmitted light images and the cross sectional area of each aggregate was measured. The aggregate diameter was calculated from the cross sectional area, assuming each cross section to be circular and using the formula for diameter of a circle. Eccentricity was calculated using the

"regionprops" function in MATLAB, defined as the ratio of the distance between the foci of the ellipse and the major axis length.

Individual cells were segmented based on Olig2, Nkx2.2, or Hb9 expression. The segmented aggregate image was first used to mask the image. To segment out individual cells, a modified version of a method developed by Lou et al. was used[110]. Starting from the greyscale image, contrast adjustment was performed as a preprocessing step. Next, we applied a Gaussian filter to the image, calculated the Hessian matrix of the resulting image, and calculated the first eigenvalue of the Hessian matrix. Then, a threshold was applied to the first eigenvalue of the Hessian matrix to eliminate dim pixel values that would otherwise result in poor segmentation. The resulting image was used as a mask to segment the contrast adjusted greyscale image. This typically yielded slightly under-segmented cells, so a watershed transform was applied to the masked greyscale cells to yield a final, binary image of segmented cells.

To quantify Olig2, Nkx2.2, or Hb9 expression for each aggregate, the total pixel area of cells expressing that marker for all five z slices was calculated. To yield a metric for expression that was normalized by aggregate size, this value was then divided by the approximate volume of the portion of the aggregate that was imaged. The volume was calculated according to the formula

$$V = \frac{\pi\, h^2}{3}(3r - h)$$

where h is the height of the sampled region (50 μm) and r is the calculated radius of the aggregate. Finally, to compare across multiple conditions, marker expression was normalized by the mean expression level in batch cultures yield the final "Normalized Olig2/Nkx2.2/Hb9 Expression".

To characterize asymmetry in Olig2 expression, the horizontal distance of each Olig2+ cell in an aggregate from the centerline of that aggregate was calculated. This value was normalized by the aggregate radius. To take into consideration the position of each aggregate within its trap, another metric was defined. For this metric, the horizontal distance of an Olig2+ cell from the trap entrance was calculated and was normalized by the total distance from the opening to back of the trap.

3.2.8 Statistical Analysis

Statistical analyses were performed using GraphPad Prism software. Statistical tests were performed using either a Mann-Whitney U test or non-parametric one-way ANOVA (with Kruskal-Wallis) combined with Dunn's multiple comparison's test for comparison of individual samples. P values less than 0.01 were considered significant.

3.3 Results and Discussion

3.3.1 Microfluidic Device Design

3.3.1.1 Overview of Device Design

To investigate the role of microfluidic culture parameters in differentiation of mESC aggregates to motor neurons, the microfluidic device developed in the previous chapter was used. This device provided the ability to observe individual stem cell aggregates over week-long cultures and to perturb the biochemical microenvironment by changing the frequency of media delivery. In this chapter, the device design and external fluid handling components were altered to improve device operation, reduce device failure rate, and provide additional experimental capabilities.

3.3.1.2 Device Design Modifications

The geometry of the device was altered to improve initial aggregate trapping (**Figure 3.1**). The original device design typically loaded with 50% of traps containing single aggregates, with remaining traps being empty or containing multiple aggregates[2]. It was observed experimentally that aggregates could deform and flow through the small resistance channel at the back of the trap, resulting in an empty trap. To address this, the resistance channel initial width was reduced from 60 μm to 40 μm, and the height was reduced from 200 μm to 100 μm (**Figure 3.1b**). A consequence of decreasing the resistance channel dimensions was that it increased the overall trap fluidic resistance, and the ratio of fluidic resistance through the traps in relation to the main channel must be balanced for loading of traps[112,113]. To offset the reduced resistance channel dimensions, the resistance channel shape was changed: the initial width of the channel was set to 40 μm and the maximum width to 80 μm (with height remaining constant) (**Figure 3.1b**). This design provided the narrow 40 μm opening needed to prevent aggregates from entering but with a lower overall fluidic resistance than a 40 μm rectangular channel.

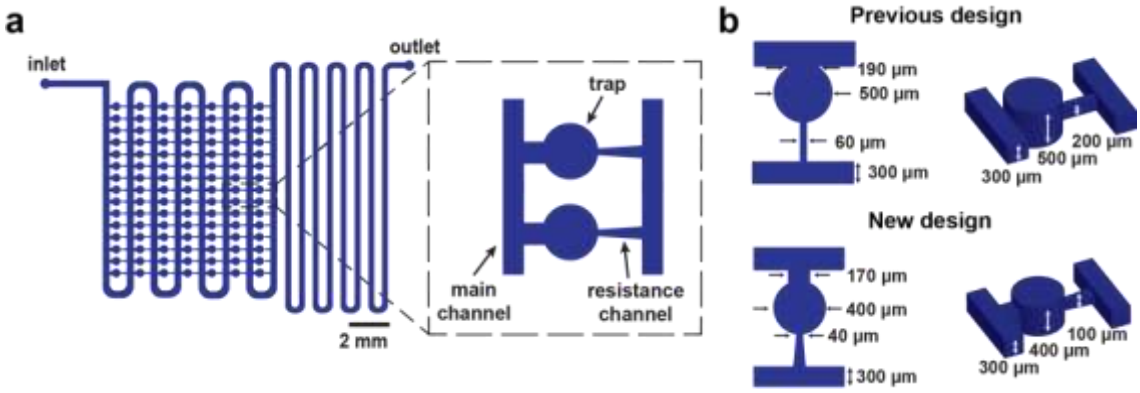

Figure 3.1. Microfluidic device design. a) Schematic illustrates the design of the new, modified microfluidic device, with inset depicting the main channel, trap, and resistance channel. b) Schematics show key geometries and dimensions of the new design, compared to the previous design.

A second design change was implemented to decrease the occurrence of aggregates flowing out of traps during culture if fluid flow disturbances occurred (for example, while attaching or detaching syringes to the device tubing). To address this, a narrowed rectangular region of width 170 μm and height 300 μm was added to the trap entrance (**Figure 3.1b**). The rationale was that as aggregates increased in size during culture, they would become physically constrained from exiting the trap upon exposure to minor flow disturbances.

In another design change, the diameter and height of the trap were reduced from 500 μm to 400 μm (**Figure 3.1b**). Over the culture time period needed for the studies in this chapter (one week), aggregates were not expected to grow larger than 400 μm. Reducing the trap size enabled a larger portion of the trap to be captured within the field of view of the microscope and more traps to be packed in a smaller device footprint.

A final design change was made to improve control over the flow rate during aggregate loading. Devices are loaded using gravity-driven flow based on a height difference between inlet and outlet, and the previous device design needed to be coupled in series with a second identical device to increase the overall fluidic resistance to achieve the desired flow rate. To avoid the need to use a second device, a serpentine channel region was added to the end of the device to increase the overall fluidic resistance (**Figure 3.1a**). The optimal flow rate for loading was determined experimentally to be ~ 1 ml/hr. Together with all of the design changes, the loading efficiency was increased from 50% to 70% singly-loaded traps. In the new design, the ratio of trap to main channel resistance of the new design is ~ 6, compared to ~ 20 with the old design.

3.3.1.3 External Fluid Handling Components

A number of external fluid handling components were added to the device to address experimental needs (**Figure 3.2**). These components addressed requirements associated with device priming, device loading, maintaining sterility, and performing microscopy on live samples. Importantly, all fluid handling components could be sterilized by autoclaving, by ethylene oxide treatment, or were purchased sterile.

The device inlet was chosen to satisfy requirements associated with priming, loading aggregates, and culture. In order to prime devices to remove bubbles prior to loading, devices were pressurized with fluid using a syringe screwed onto the luer lock connection of the inlet (**Figure 3.2**). For loading of aggregates and subsequent culture, a standard 3 mL syringe with the plunger removed was screwed on to the device inlet as a media reservoir. This provided a volume large enough that that the reservoir needed to be filled only once per day or less.

Two types of valves were used. The pinch valve was used during priming to maintain pressurization of the device. During aggregate loading and in all following device manipulations, the two-way valve was used to stop flow through the device as opposed to the pinch valve. The pinch valve displaced fluid back into the device that could dislodge trapped aggregates, whereas the two-way valve displaced a minimal amount of fluid.

To perfuse media at a defined rate and frequency during culture, the outlet tubing was connected to a syringe on a syringe pump. The pump was programmed to withdraw media from the media reservoir, through the device, at defined rate and frequency.

Finally, during experiments, devices containing live aggregates needed to be transported sterilely between biosafety cabinets, incubators, and microscopes. The syringe filter at the device outlet provided a sterile barrier, and sterile, gas-permeable adhesive film was used to create a sterile barrier at the opening to the media reservoir. For live microscopy, the media reservoir could be unscrewed from the device inlet and the device inlet sterilely sealed with a luer lock connector in order to fit on a confocal or epifluorescent microscope.

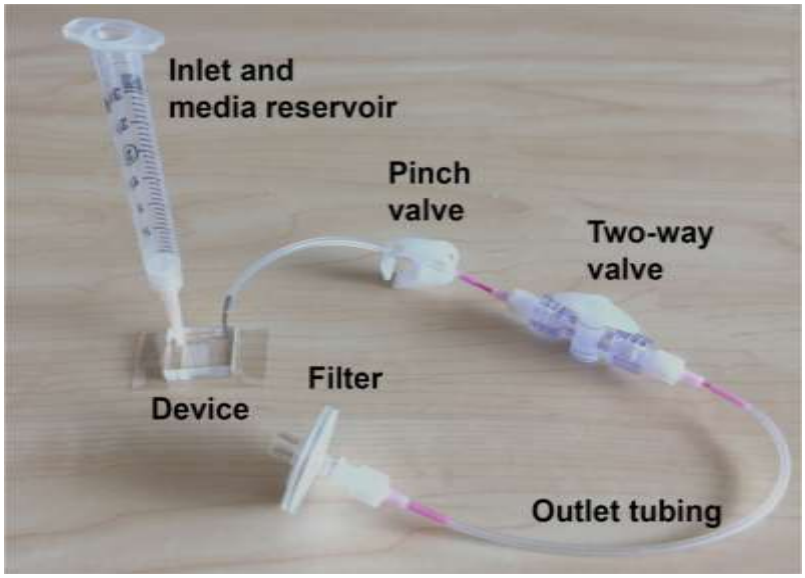

Figure 3.2. Device and external fluid handling components. Photograph depicts the microfluidic device and external components, including the inlet and media reservoir, valves, outlet tubing, and filter.

3.3.2 Differentiation under Continuous and Discontinuous Perfusion

3.3.2.1 Overview

To investigate the role of the microfluidic media exchange method on mESC motor neuron differentiation, we differentiated mESC aggregates according to an established protocol[35,44,127]. Aggregates were formed from G-Olig2 mESCs in basal differentiation media and cultured in devices or plate controls starting at day 1. Retinoic

acid (RA) and sonic hedgehog agonist purmorphamine (Pur) were added to the media starting at day 2 and with every successive media change to promote motor neuron differentiation (**Figure 3.3**). The fluorescent reporter cell line enabled assessment of Olig2 expression, a marker for progenitor motor neurons (pMNs), in live aggregates.

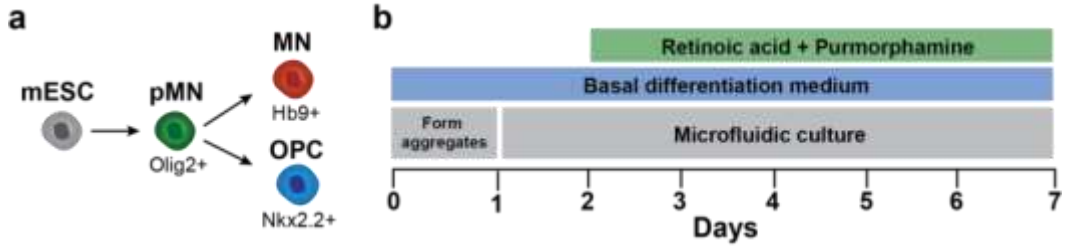

Figure 3.3. Differentiation of mESC aggregates to motor neurons. a) Cartoon depicts the differentiation of mESCs first to pMNs marked by Olig2 and then to either Hb9+ MNs or Nkx2.2+ OPCs. b) Schematic shows the differentiation protocol used.

We hypothesized that discontinuous media perfusion would be more effective at supporting cell growth than continuous media perfusion, due to the ability of continuous perfusion to alter diffusible cell signaling. To test this, we compared discontinuous perfusion at a frequency of $f = 1\ d^{-1}$ (e.g. exchanging media once per day) to continuous perfusion at a rate of 10 μL hr^{-1} and assessed cultures at day 7 of differentiation. For discontinuous perfusion, there was no media flow in devices except during media exchange. For this condition, every 24 hours media within devices was completely exchanged by manually flushing ~4 device volumes worth of media through each device. The day 7 time point was chosen based on preliminary experiments (not shown) indicating that this was when generation of Olig2+ pMNs could best be observed.

3.3.2.2 Aggregate Size and Morphology

To assess cell growth, we characterized aggregate size and morphology. Aggregate size was quantified by measuring the aggregate cross-sectional area in bright

field images (**Figure 3.4a**). Aggregates cultured at $f = 1\ d^{-1}$ were slightly smaller on average than plate controls, but this difference was not statistically significant. In contrast, aggregates cultured at 10 μL hr^{-1} were significantly smaller than plate controls ($p<0.0001$). As a descriptor of aggregate shape, eccentricity was calculated from bright field images (**Figure 3.4b**). Aggregates cultured at $f = 1\ d^{-1}$ had less circular morphologies than plate controls ($p<0.01$). This is likely explained by the observation that aggregates could conform to segments of the trap wall, resulting in non-circular shapes. In contrast, aggregates cultured at 10 μL hr^{-1} were similar in shape to controls. As aggregates in this condition remained small, influences of trap shape had little to no effect. Overall, this data indicates that cell growth was not statistically significantly different between cultures at $f = 1\ d^{-1}$ and plate controls, but growth under culture at 10 μL hr^{-1} was reduced. Two possible explanations for the reduced growth are that cells were nutrient limited or that continuous perfusion removed cell-secreted molecules necessary for growth. To explore which of these two possibilities explained the data, a transport modeling analysis was next performed.

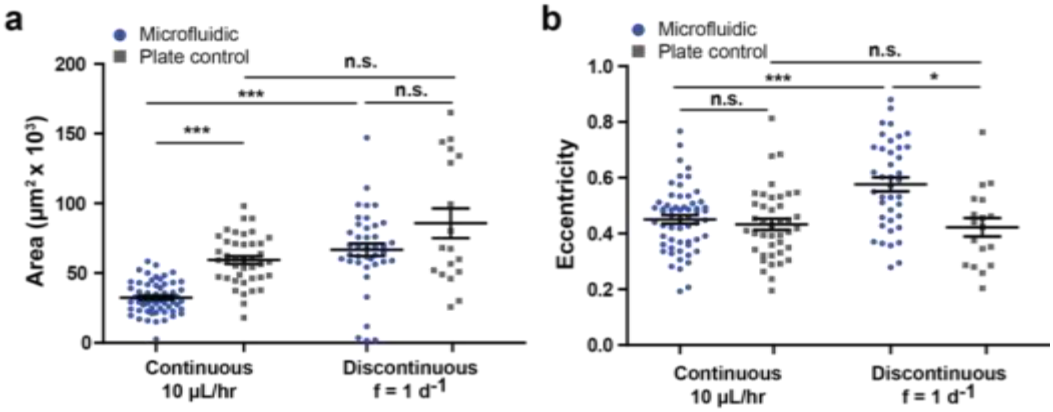

Figure 3.4. Effects of media perfusion method on morphology. a) Aggregate cross-sectional area was measured from bright field images at day 7. b) Aggregate eccentricity was measured from bright field images at day 7. Continuous: n = 58 from 2 devices; Plate control: n = 41. Discontinuous: n = 67 from 2 devices; Plate control: n = 18. Error bars

indicate SEM. Kruskal-Wallis test with Dunns multiple comparisons was used. * indicates $p < 0.01$; *** indicates $p < 0.0001$.

3.3.2.3 Transport modeling analysis

One possible explanation for reduced growth is that cells were nutrient limited. To investigate whether either of the media exchange conditions was likely nutrient limiting, relevant transport parameters were calculated. For continuous perfusion, we calculated the time scale, τ_{rxn}, for glucose to be completely consumed by all aggregates in the device. We defined $\tau_{rxn} = (C_{initial}V_{device})/(K_{glucose}N_{aggregates}N_{cells})$ where $C_{initial}$ is the initial glucose concentration, V_{device} is the device volume, $K_{glucose}$ is the cell consumption rate of glucose, $N_{aggregates}$ is the number of aggregates, and N_{cells} is the number of cells per aggregate[117]. Values for these parameters are listed in **Table 3.1**. We found that $\tau_{rxn} \approx 50$ hours. This time scale for glucose consumption was compared to the convective time scale, $\tau_{conv} = L_{device}/v_c$ where L_{device} is the linear length through the main serpentine channel of the device and v_c is average linear velocity for continuous perfusion. This convective time scale represents the residence time of a fluid element flowing through the main channel of the device. We found that $\tau_{conv} \approx 0.75$ hours. These calculations indicate that the time scale of convection is much faster than that of glucose consumption. Therefore, there is likely sufficient delivery of a nutrient such as glucose at this perfusion rate. Furthermore, nutrients are likely not depleted by aggregates upstream in the device before media reaches aggregates at the outlet.

To assess whether the time interval between media exchanges was sufficient for discontinuous perfusion, we again calculated the time scale, τ_{rxn}, for glucose to be completely consumed in the device. This value was the same as for continuous perfusion: $\tau_{rxn} \approx 50\ hours$, indicating that exchanging media once per day was likely sufficient.

As fluid shear stress can modulate cell behavior, we calculated the shear stress for all perfusion conditions tested. Shear stress is defined as $T = (6\mu Q)/(h^2 w)$ where T is fluid shear stress, μ is viscosity of water, Q is the volumetric flow rate, h is the main channel height, and w is the main channel width. For the range of device operating conditions, shear stress was within $T \approx 0.005 - 0.01\ dyn\ cm^{-2}$. As operation at shear stresses $\ll 1\ dyn\ cm^{-2}$ is considered not likely to affect cell phenotype[100], we assumed shear did not have effects in our system.

Based on these transport calculations, we concluded that reduced aggregate growth in culture under continuous perfusion was not due to nutrient restrictions, but rather due to perfusion-based removal of cell-secreted factors necessary for growth. To assess whether continuous perfusion can remove cell-secreted factors, we calculated the Peclet number, Pe, which represents the ratio between convection and diffusion. We defined $Pe = (L_{trap,depth} v_c)/D_{growth\ factor}$ where $L_{trap,depth}$ is the trap depth, v_c is the average linear fluid velocity, and $D_{growth\ factor}$ is the diffusion coefficient of a growth factor. For this calculation, we used v_c for the main channel—a simplified assumption, as velocity changes with position in the device. Expected actual variations in this velocity ultimately did not impact the calculated Peclet number significantly. For continuous perfusion, we calculated $Pe \gg 1$ for transport of a cell-secreted molecule such as a growth factor, indicating that convection dominates and can indeed perturb cell-secreted signaling. This conclusion is supported by previous work that demonstrated inhibition of cell growth under continuous perfusion conditions[99]. These results highlight how nutrient delivery and letting cell-secreted factors accumulate are inherently conflicting

requirements that ultimately need to be balanced in designing operating conditions for a microfluidic device.

Table 3.1: Transport modeling parameters

Parameter Name	Symbol	Value
Diffusion coefficient, glucose[128]	$D_{glucose}$	$6 \times 10^{-10}\ m^2\ s^{-1}$
Diffusion coefficient, growth factor[129]	$D_{growth\ factor}$	$2 \times 10^{-11}\ m^2\ s^{-1}$
Viscosity, water	μ_{water}	$8.9 \times 10^{-3}\ dyn\ s\ cm^{-2}$
Consumption rate, glucose[128]	$K_{glucose}$	$1 \times 10^{-17}\ mol\ cell^{-1} s^{-1}$
Consumption rate, growth factor[129]	$K_{growth\ factor}$	$2 \times 10^{-22}\ mol\ cell^{-1} s^{-1}$
Initial concentration, glucose	$C_{initial,glucose}$	$25\ mol\ m^{-3}$
Trap depth	$L_{trap,depth}$	$550\ \mu m$
Trap height	$L_{trap,height}$	$400\ \mu m$
Channel width and height	$h_{channel}$	$300\ \mu m$
Total channel length	$L_{channel}$	80 mm
Volume of trap	V_{trap}	$0.06\ \mu L$
Volume of device	V_{device}	$20\ \mu L$
Number of cells per aggregate	N_{cells}	4000
Number of aggregates per device	$N_{aggregates}$	70
Average linear velocity, continuous perfusion	v_c	$30\ \mu m\ s^{-1}$
Average linear velocity, discontinuous perfusion	v_d	$600\ \mu m\ s^{-1}$

3.3.2.4 Differentiation of pMNs

To assess how media perfusion method impacted differentiation of mESCs to pMNs, we next assessed Olig2 expression at day 7 of culture under the same two conditions. With this differentiation protocol, generation of Olig2+ pMNs is expected at

this time point. Preliminary experiments (not shown) with this differentiation protocol in batch culture indicated that day 7 was a relevant time point for assessments. As seen in the representative confocal microscopy images (**Figure 3.5a**), little Olig2 expression was observed in both the $f = 1\ d^{-1}$ and 10 μL hr^{-1} conditions, whereas many Olig2+ cells were observed in plate controls. The amount of Olig2 expression for individual aggregates in each condition was quantified using image processing (**Figure 3.5b**). Quantification revealed that there was no Olig2 expression in 10 μL hr^{-1} cultures, which the exception of three outliers. Examination of the data provided no explanation for the existence of these outliers. Olig2 expression was slightly higher in $f = 1\ d^{-1}$ cultures, but the difference compared to 10 μL hr^{-1} was not statistically significant, likely due to the three outlying aggregates. For both perfusion conditions, Olig2 expression was significantly lower than plate controls ($p < 0.0001$).

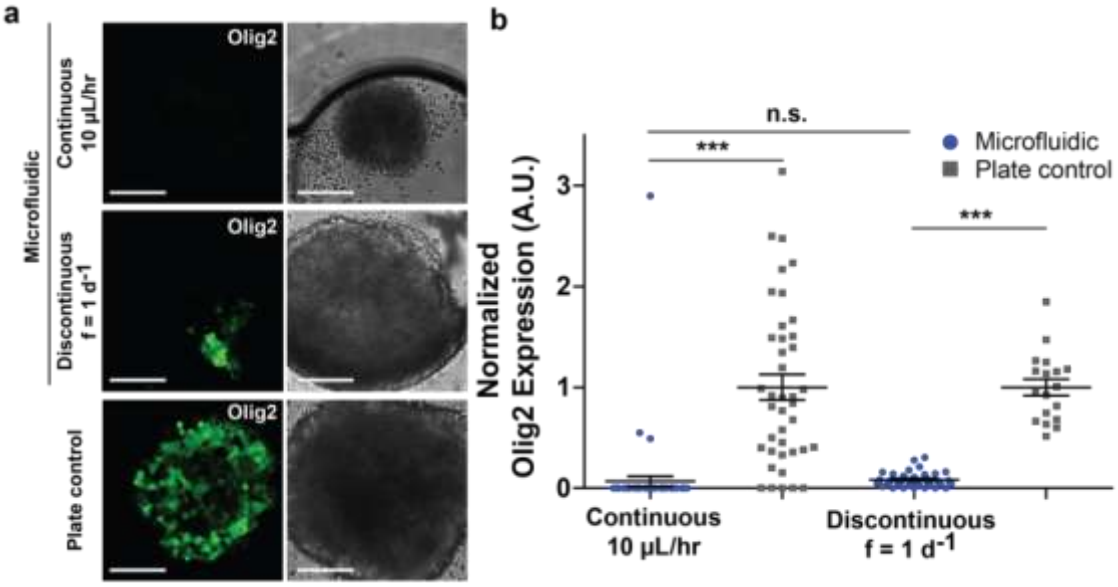

Figure 3.5. Effect of media perfusion method on differentiation of pMNs. a) Representative images from a single confocal slice of Olig2 expression at day 7 and corresponding bright field images. All scale bars are 100 μm. b) Normalized Olig2 expression quantified for each condition. Continuous: n = 58 from 2 devices; Plate control: n = 41 aggregates. Discontinuous: n = 37 from 1 device; Plate control: n = 18.

Error bars represent SEM. Kruskal-Wallis test with Dunns multiple comparisons was used. *** indicates p < 0.0001. Plate controls were n.s.

3.3.2.5 Effects of Aggregate Size and Device Position on pMN Differentiation

We next investigated whether there were any trends between Olig2 expression and other parameters for $f = 1\ d^{-1}$ cultures. We did not assess 10 μL hr^{-1} cultures since expression levels were so low. We measured the correlation between Olig2 expression and aggregate size (**Figure 3.6a**) by calculating the Spearman rank correlation. The Spearman correlation coefficient ranges from -1 to +1; values of +1, 0, and -1 indicate total positive, no, and total negative correlations, respectively. As summarized in **Table 3.2**, aggregate size and Olig2 expression was not significantly correlated for device cultures (R=0.033; n.s.) but was positively correlated for plate controls (R=0.66; p<0.001).

Table 3.2: Spearman Rank Correlation Analysis of Olig2 Expression and Aggregate Size

Condition	Spearman correlation coefficient	P value
$f = 1\ d^{-1}$	R = 0.033	n.s.
Plate control	R = 0.66	P < 0.001

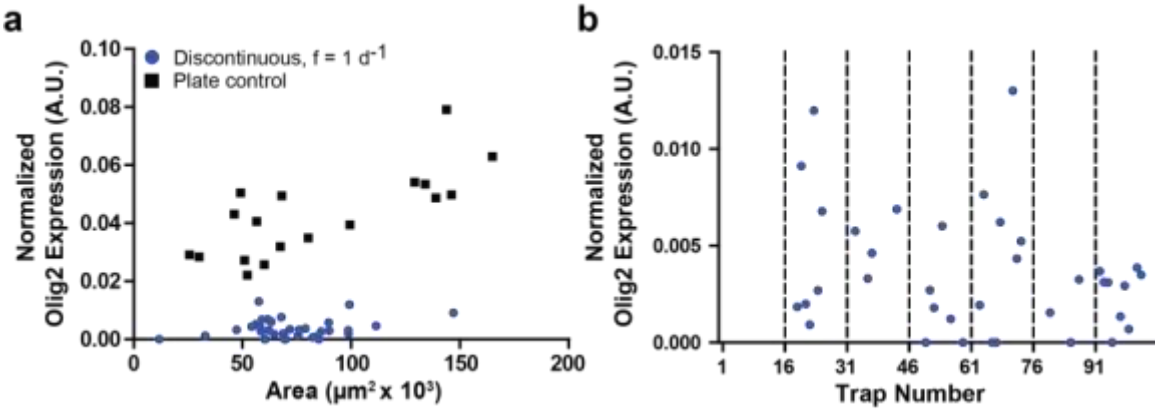

Figure 3.6. Effects of aggregate size and device position on pMN differentiation. a) Correlation between aggregate area and normalized Olig2 expression at day 7. b) Normalized Olig2 expression for aggregates in a single representative device plotted based on position in the device. Traps are numbered with respect to position along the serpentine channel, with trap 1 at the inlet and trap 105 at the outlet.

Next, we assessed if there was a relationship between Olig2 expression of a given aggregate and its location in the device. In **Figure 3.6b**, Olig2 expression for a given aggregate is plotted in relation to that aggregate's position. Traps are numbered sequentially based on position following the main channel, with trap 1 at the inlet and trap 105 at the outlet. Although there is variability in Olig2 expression among aggregates, there is no clear correlation with position.

3.3.2.6 Discussion

Overall, these data indicate that both of these media exchange conditions do not promote differentiation of large populations of pMNs. For the reduced cell growth and minimal pMN differentiation observed for the 10 μL hr^{-1} condition, transport modeling and previous literature supports a proposed mechanism that continuous perfusion alters autocrine/paracrine signaling required both for growth and differentiation. The minimal pMN differentiation observed for $f = 1\,d^{-1}$ was an unexpected result. Transport modeling suggested that this was likely not due to nutrient limitations, so we next explored how additional perturbations of endogenous and exogenous signaling would influence pMN differentiation.

3.3.3. Effects of increasing RA and Pur Delivery on pMN Differentiation

3.3.3.1 Overview

Following the initial assessment of pMN differentiation under continuous and discontinuous perfusion, we hypothesized that lower effective concentrations of RA and Pur in microfluidic devices may have contributed to the minimal differentiation that was observed. It is known that PDMS absorbs small molecules and hydrophobic molecules in

particular[130,131]. The tendency of PDMS to absorb a given molecule (the partition coefficient) is related to the logarithm of the octanol-water partition coefficient (logP) of that molecule[132]. In a study conducted by Wang et al.[132], molecules with logP < 2.5 exhibited low absorption into PDMS (<25% after 4.5 hours) and molecules with logP>2.5 exhibited high absorption (>75% after 0.5 hours). RA and Pur have logP values of 6.30 (source: Sigma-Aldrich) and 7.58 (source: EPA[133]), respectively, and therefore are potentially highly absorbed by PDMS.

To evaluate whether increased delivery of RA and Pur to microfluidic cultures could promote increased pMN differentiation, we differentiated mESC aggregates under discontinuous perfusion at $f = 3\ d^{-1}$ (e.g. exchange media every 8 hours) at three-fold increased RA and Pur concentrations (6 μM and 3 μM, respectively). This condition was chosen to increase both nutrient and RA/Pur delivery. Media was exchanged in devices at this discontinuous perfusion frequency by flushing media through devices once every 8 hours at a flow rate of 200 μL hr^{-1} for a duration of 24 minutes. For comparison, we differentiated plate controls at both the original (2 μM RA; 1.5 μM Pur) and new concentrations (6 μM RA; 3 μM Pur).

3.3.3.2 Aggregate Size and Morphology

To assess aggregate growth and morphology, we quantified aggregate cross-sectional area and eccentricity. Aggregate size in $f = 3\ d^{-1}$ cultures was comparable to plate controls cultured at the same concentration but lower than plate controls cultured at the original RA and Pur concentrations (**Figure 3.7a**). This suggests that both the culture format and concentrations of RA and Pur affect cell growth. Quantification of eccentricity showed that aggregates cultured in devices displayed a less round

morphology than both sets of plate controls (**Figure 3.7b**). This observation matched that for $f = 1\ d^{-1}$ cultures—that aggregates tend to adopt the shape of portions of the trap as they grow, resulting in increased non-circular morphologies.

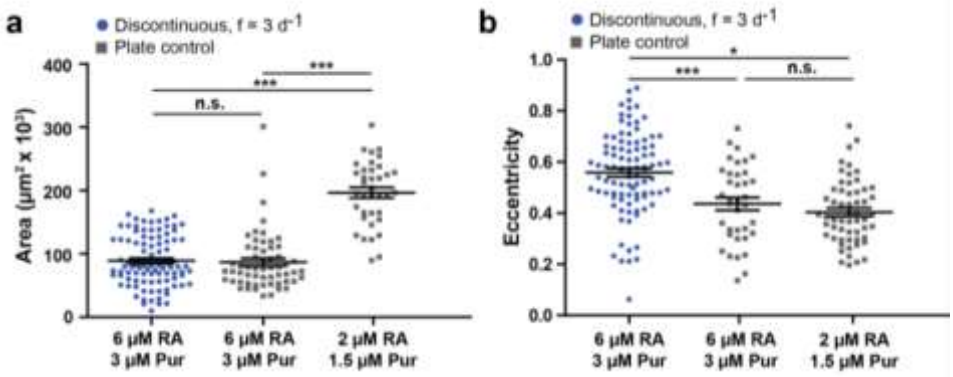

Figure 3.7. Effects of discontinuous perfusion and RA and Pur concentrations on morphology. a) Aggregate cross-sectional area was measured from bright field images at day 7. b) Aggregate eccentricity was measured from bright field images at day 7. Discontinuous device: n = 94 from 2 devices. Plate control (6 μM/3 μM): n = 58. Plate control (2 μM/1.5 μM): n = 37. Error bars indicate SEM. Kruskal-Wallis test with Dunns multiple comparisons was used. * indicates < 0.01; *** indicates p < 0.0001.

3.3.3.3 Differentiation of pMNs

We next assessed the effects of increasing RA and Pur delivery on differentiation of pMNs at day 7. We observed increased Olig2 expression in $f = 3\ d^{-1}$ cultures compared to $f = 1\ d^{-1}$ cultures, as shown in the representative images (**Figure 3.8a**). Quantification of Olig2 expression indicated that in $f = 3\ d^{-1}$ the mean expression level was comparable to plate controls cultured at the same concentration (6 μM RA; 3 μM Pur) but lower than the mean level of expression in plate controls cultured at the original RA and Pur concentrations (2 μM RA; 1.5 μM Pur) ($p<0.0001$; **Figure 3.8b**). Variability in the amount of Olig2 expression was observed across all experimental groups. Aggregates cultured in devices at $f = 3\ d^{-1}$ displayed a range of expression levels,

including a sub-population of aggregates with no Olig2 expression (**Figure 3.8b**). Plate controls also exhibited a range of expression levels.

The increase in pMN differentiation in microfluidic cultures with increased delivery of RA and Pur supports the hypothesis that effective concentrations of these exogenous factors were likely lower in devices compared to plate controls. These small molecules are likely absorbed by PDMS, as literature suggests[130,131], and the data presented here suggests that this effect can be partially compensated for by increasing concentration and delivery frequency. In plate controls, we observed that the amount of pMN differentiation in plate controls was reduced by increasing concentrations of RA and Pur to 6 μM and 3 μM respectively. During embryonic development, gradients of Shh signaling produce different progenitor domains, one of which consists of pMNs[35]. Previous work has shown that changing the concentration of Pur, a Shh agonist, affects numbers of Olig2+ pMNs generated[44]. Although this was not characterized in these experiments, it is likely that increasing the Pur concentration in plate controls shifted differentiation to other neural progenitor domains.

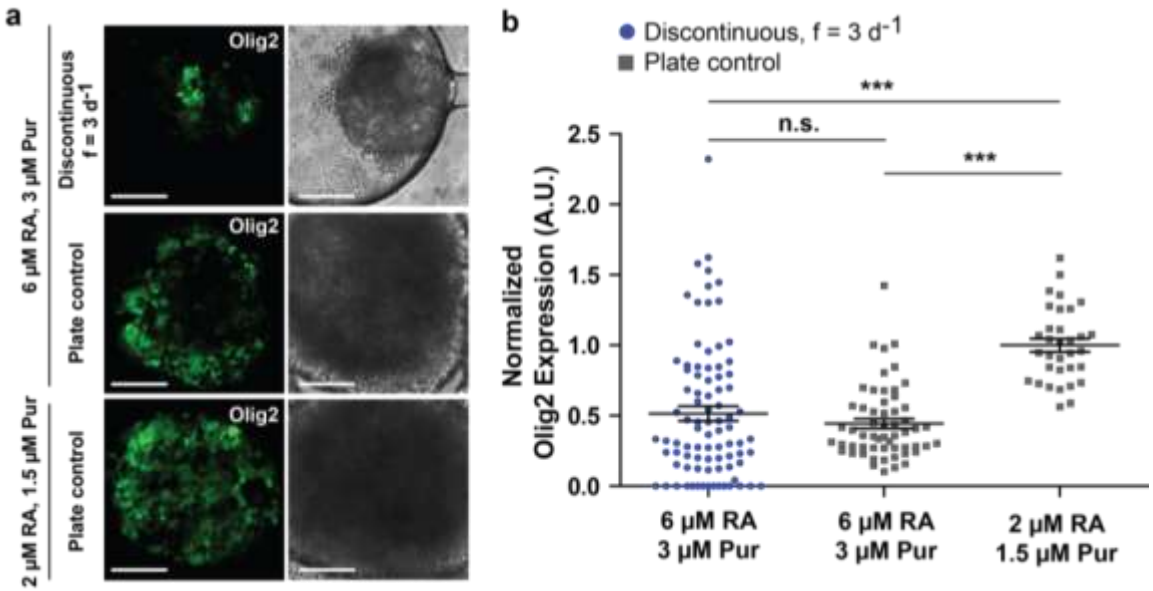

Figure 3.8. Effects of discontinuous perfusion and RA and Pur concentration on differentiation of pMNs. a) Representative images from a single confocal slice of Olig2 expression at day 7 and corresponding bright field images. All scale bars are 100 µm. b) Normalized Olig2 expression quantified for each condition. Discontinuous device: n = 91 from 2 devices. Plate control (6 µM/3 µM): n = 58. Plate control (2 µM/1.5 µM): n = 33. Error bars represent SEM. Kruskal-Wallis test with Dunns multiple comparisons was used. *** indicates $p < 0.0001$.

3.3.3.4 Effects of Aggregate Size and Device Position on pMN Differentiation

We next investigated whether there were any trends between Olig2 expression and other parameters for $f = 3\ d^{-1}$ cultures. As before, we measured the correlation between Olig2 expression and aggregate size (**Figure 3.9a**) by calculating the Spearman rank correlation. As summarized in **Table 3.3**, aggregate size and Olig2 expression was significantly correlated for all three experimental groups: device cultures (R=0.34; p<0.001), plate controls at the same supplemented concentration (R=0.35; p<0.001), and plate controls at the lower concentration (R=0.44; p<0.01).

Table 3.3: Spearman Rank Correlation Analysis of Olig2 Expression and Aggregate Size

Condition	Spearman correlation coefficient	P value

$f = 3\ d^{-1}$ *6 μM RA, 3 μM Pur*	R = 0.34	P < 0.001
Plate control *6 μM RA, 3 μM Pur*	R = 0.35	P < 0.001
Plate control *2 μM RA, 1.5 μM Pur*	R = 0.44	P < 0.01

We also assessed if there was a relationship between Olig2 expression of a given aggregate and its location in the device. In **Figure 3.9b**, Olig2 expression for a given aggregate is plotted in relation to that aggregate's position. Traps are numbered sequentially based on position following the main channel, with trap 1 at the inlet and trap 105 at the outlet. Although there is variability in Olig2 expression among aggregates, as with $f = 1\ d^{-1}$ cultures. There is no clear correlation with position.

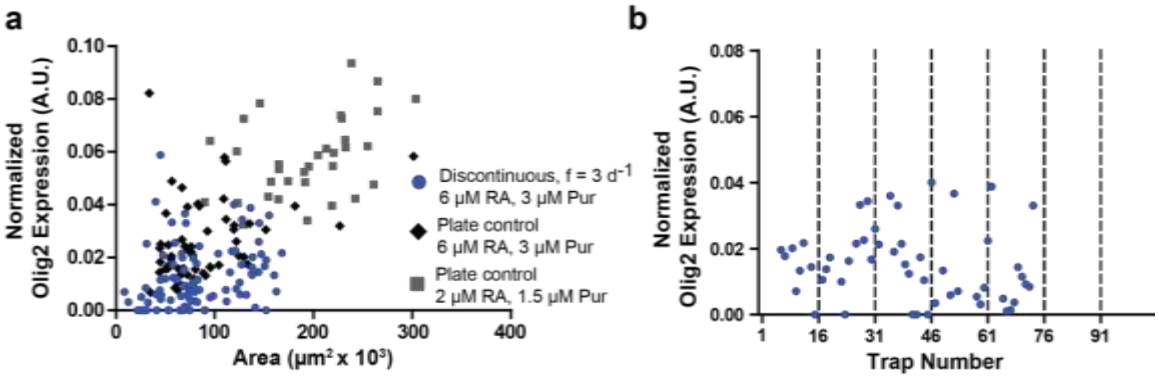

Figure 3.9. Effects of aggregate size and device position on pMN differentiation. a) Relationship between aggregate area and normalized Olig2 expression at day 7. b) Normalized Olig2 expression for aggregates in a single representative device plotted based on position in the device. Traps are numbered with respect to position along the serpentine channel, with trap 1 at the inlet and trap 105 at the outlet.

3.3.3.5 Differentiation of MNs and OPCs

As it is known that during differentiation pMNs generate both MNs and OPCs, we next wanted to investigate whether these cell types were generated in the $f = 3\ d^{-1}$ microfluidic cultures. To assess generation of MNs, we performed immunostaining for

the MN marker Hb9. Hb9 expression was observed both in microfluidic cultures and in plate controls, as seen in the representative images (**Figure 3.10a**). Quantification of Hb9 expression using image analysis showed culture format and concentration dependent effects (**Figure 3.10b**). Microfluidic cultures ($f = 3\ d^{-1}$; 6 μM RA, 3 μM Pur) on average expressed Hb9 at low levels, with some variability in amount of expression. Plate controls at the same supplemented concentration of small molecules (6 μM RA, 3 μM Pur) had slightly higher levels of Hb9 expresison ($p<0.0001$). Plate controls at lower small molecule concentrations (2 μM RA, 1.5 μM Pur) had the highest levels of Hb9 expression ($p<0.001$).

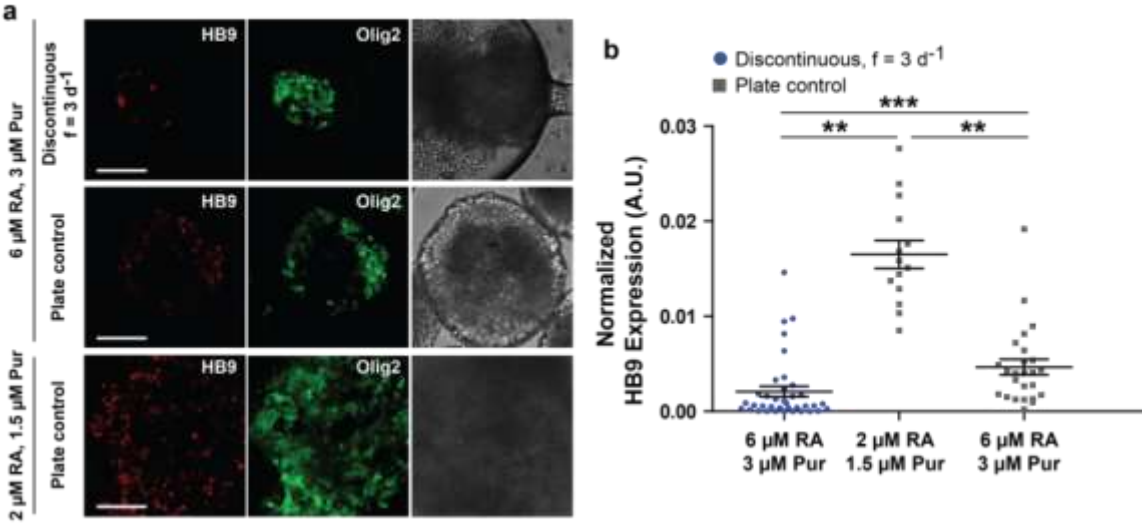

Figure 3.10. Effects of discontinuous perfusion and RA and Pur concentration on differentiation of committed MNs. a) Representative images from a single confocal slice of normalized Hb9 and Olig2 expression at day 7 and corresponding bright field images. All scale bars are 100 μm. b) Normalized Hb9 expression quantified for each condition. Discontinuous device: n = 37 from 1 device. Plate control (6 μM/3 μM): n = 25. Plate control (2 μM/1.5 μM): n = 14. Error bars represent SEM. Kruskal-Wallis test with Dunns multiple comparisons was used. ** indicates $p < 0.001$; *** indicates $p < 0.0001$.

In the same experiment, we assessed generation of OPCs by performing immunostaining for Nkx2.2. As depicted in the representative images (**Figure 3.11a**) and confirmed by quantification (**Figure 3.11b**), Nkx2.2 expression was observed at low

levels in microfluidic cultures and plate controls at the same supplemented RA and Pur concentration. Nkx2.2 expression was much higher in plate controls at the higher RA and Pur concentrations ($p<0.0001$ versus microfluidic culture; $p<0.01$ versus plate controls at the higher concentration).

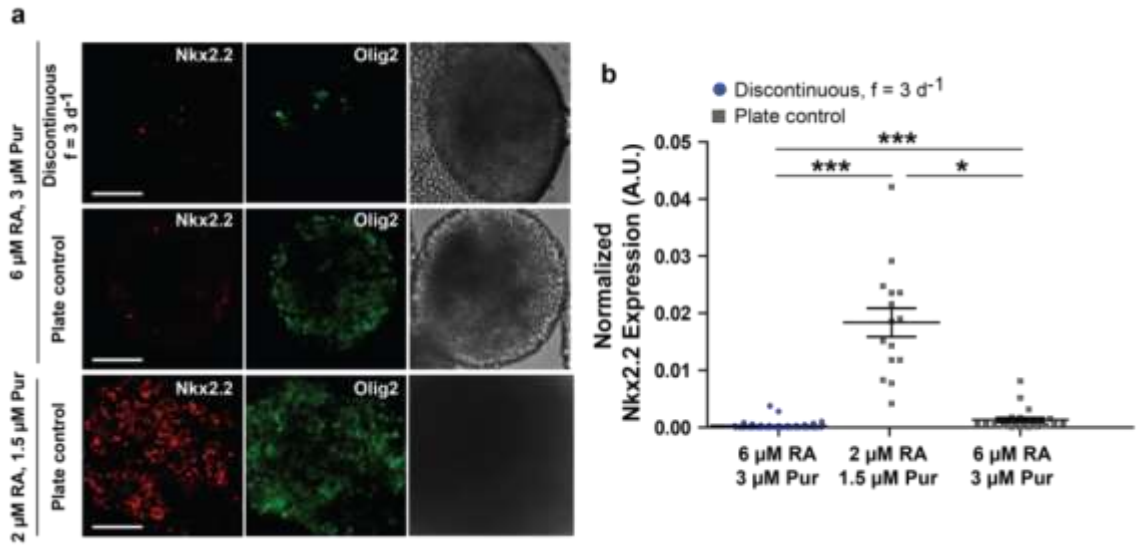

Figure 3.11. Effects of discontinuous perfusion and RA and Pur concentration on differentiation of OPCs. a) Representative images from a single confocal slice of normalized Nkx2.2 and Olig2 expression at day 7 and corresponding bright field images. All scale bars are 100 µm. b) Normalized Nkx2.2 expression quantified for each condition. Discontinuous device: n = 56 from 1 device. Plate control (6 µM/3 µM): n = 23. Plate control (2 µM/1.5 µM): n = 15. Error bars represent SEM. Kruskal-Wallis test with Dunns multiple comparisons was used. * indicates $p < 0.01$; *** indicates $p < 0.0001$.

3.3.3.6 Discussion

Together, this data demonstrates that pMNs give rise to both MNs and OPCs in these cultures. In the microfluidic cultures, amounts of both cell types are lower than in plate controls, and in particular, microfluidic cultures show very little differentiation of Nkx2.2+ OPCs.

3.3.4 Influence of Device Asymmetry on Microenvironment and pMN Differentiation

3.3.4.1 Rationale

For microfluidic-based culture and analysis of stem cell aggregates, device designs that incorporate physical traps or chambers[76,86,87] to isolate aggregates, such as the design used in this chapter, are common. The advantage of these types of designs is that they can be used to prevent physical interactions between aggregates and they enable observation of phenotypes through time. However, geometries of traps or chambers can influence the biochemical microenvironment, based on how they influence media exchange characteristics. Indeed, Khoury et al.[86] has shown how culturing hESC aggregates in microfluidic traps allowed for the formation of biochemical gradients. Given the potential for interactions among device asymmetrical geometries and media transport properties to produce differences in the biochemical microenvironment, we sought to characterize these for our system.

Due to the design of the microfluidic platform, there is potential for trapped aggregates to be asymmetrically exposed to media flow. At earlier time points, when aggregate diameter is much less than the trap size, media exchange through the trap is convection-based. However, as aggregate diameter increases throughout culture, aggregates can grow large enough to partially or completely block flow through the traps. When flow through a trap is completely blocked, media is exchanged solely by diffusion. In this case, gradients of both nutrients and cell-secreted factors can form that potentially affect cell growth and differentiation and even create spatially patterned phenotypes.

3.3.4.2 Spatial Characterization of pMN Differentiation

To investigate whether biochemical gradients were present in our microfluidic system that affected differentiation of pMNs, we assessed spatial patterns of Olig2 expression. We examined data from two microfluidic culture conditions: discontinuous perfusion at $f = 1\ d^{-1}$ (with 3 μM RA, 1.5 μM Pur) and discontinuous perfusion at $f = 3\ d^{-1}$ (with 6 μM RA, 3 μM Pur).

To first assess if flow of media through traps was hindered by aggregates, we manually curated bright field images of aggregates at day 7 of differentiation, the day that pMN expression was measured. For each culture condition, we counted the number of aggregates that were large enough or positioned such that they likely at least partially reduced media flow through the trap. We found that 65% of aggregates in $f = 1\ d^{-1}$ cultures and 79% of aggregates in $f = 3\ d^{-1}$ cultures likely reduced media flow through the traps (**Table 3.4**). This indicated that it was possible by day 7 of differentiation that there was reduced media flow through the traps.

Table 3.4: Percentages of aggregates blocking flow through traps

Condition	% aggregates reducing flow through traps
$f = 1\ d^{-1}$ *3 μM RA, 1.5 μM Pur*	65%
$f = 3\ d^{-1}$ *6 μM RA, 3 μM Pur*	79%

To assess if reduced media flow through traps could produce biochemical gradients of cell-secreted molecules, we calculated the diffusion time scale for a representative growth factor, using parameters available for the growth factor EGF. Time scale of diffusion is represented by the equation $\tau = L^2/D$ where L is the trap depth

and D is the diffusion coefficient. Using values from **Table 3.1**, we calculated the time scale of diffusion of a growth factor to be ~4 hours. Given that media was exchanged every 8 hours or every 24 hours for the two conditions tested, this diffusion time scale suggested that gradients of cell-secreted factors could potentially form between media exchanges.

We hypothesized that if biochemical gradients were present, they would alter cell phenotypes in aggregates according to spatial proximity to the main channel, where media was exchanged. To assess if this was indeed the reason, we quantified the horizontal distance of each Olig2+ cell in an aggregate from the centerline of that aggregate (**Figure 3.12a**). This value was normalized the aggregate radius, calculated from the measured cross-sectional area. In **Figure 3.12b-e**, the histograms show the relative frequency of Olig2+ cells at a given horizontal differentiation from the aggregate centerline, where 0 is the aggregate centerline, positive x values indicate cells closer to the trap entrance, and negative x values indicate cells closer to the back of the trap. Each plot reflects population-level data from all aggregates for that condition. For aggregates cultured at $f = 1\ d^{-1}$, Olig2+ cells appeared to be localized in regions on both sides of the aggregate centerline, with a slightly larger peak of cells in regions closer to the backs of traps (**Figure 3.12b**). Assessment of histograms for individual aggregates (**Appendix B.1**) showed that individual aggregate spatial distributions were varied. Some had Olig2 expression in regions closer to the trap entrance, some had expression closer to the trap back, and some had expression throughout. For aggregates cultured at $f = 3\ d^{-1}$, a larger proportion of Olig2+ cells were located in regions of aggregates closer to the backs of traps (**Figure 3.12c**). This trend was also observed in individual aggregate distributions

(**Appendix B.3,4**), despite there being some variability. In contrast to microfluidic cultures, in plate controls at both RA and Pur concentrations Olig2+ cells were distributed symmetrically through aggregates (**Figure 3.12d,e**). The slight asymmetry in the distributions appeared to be a result of individual aggregate heterogeneity (**Appendix B.7,8**).

Manual curation of this data was performed to identify potential correlations between spatial location of Olig2 expression and aggregate size, aggregate position within trap, or aggregate position within the device. However, this analysis revealed no clear trends. Additionally, to assess any effects associated with position of an aggregate within a trap, we quantified positions of Olig2+ cells in a given aggregate with respect to the reference frame of the trap. Measuring the horizontal distance of each Olig2+ cell from the trap centerline, normalized by the total trap depth, revealed no new information (**Appendix B.2,5,6**).

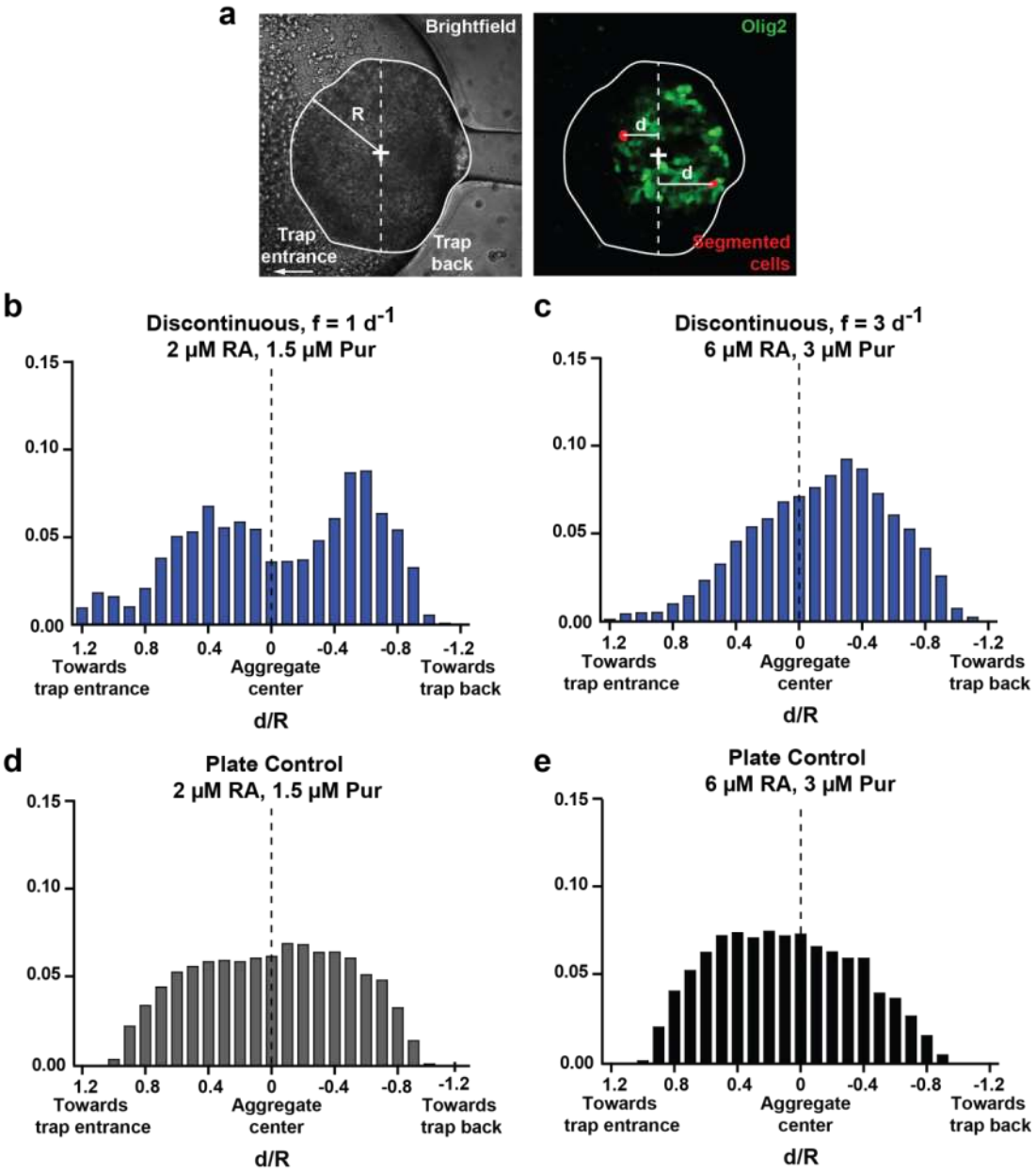

Figure 3.12. Effects of discontinuous perfusion frequency on spatial characteristics of Olig2 expression. a) Image describes how metric is quantified. Histograms show population-level data for horizontal position of Olig2+ cells with respect to aggregate center line for (b) discontinuous perfusion (f = 1 d^{-1}) with 2 μM RA and 1.5 μM Pur (n = 31 from 1 device), (c) discontinuous perfusion (f = 3 d^{-1}) with 6 μM RA and 3 μM Pur (n = 47, representative of 2 devices), (d) plate controls with 2 μM RA and 1.5 μM Pur (n = 13), and (e) plate controls with 6 μM RA and 3 μM Pur (n = 25).

3.3.4.3 Discussion

Spatial characterization of Olig2 expression revealed differences in aggregates cultured under different conditions. Aggregates cultured at $f = 1\ d^{-1}$ showed variability

in where Olig2 expression was localized in relation to the trap geometry. If there were local gradients in cell-secreted factors for this media exchange condition, these did not produce clear trends in the data. In contrast, in aggregates cultured at $f = 3\,d^{-1}$ and increased RA and Pur concentrations, there was more Olig2 expression in regions of aggregates further away from the main channel. This data supports our hypothesis that when aggregates restrict media flow through traps, local gradients of cell-secreted factors or other soluble molecules are created, and these result in asymmetric patterns of differentiation.

3.4 Conclusions

This chapter explored how key parameters of microfluidic culture of stem cell aggregates influenced cell growth and differentiation. Media exchange strategy was found to be a key parameter in modulating cell growth and differentiation of mESCs to pMNs. Continuous media perfusion resulted in less cell growth and minimal generation of pMNs, which we proposed was due to modulation of diffusible autocrine/paracrine signaling and not a consequence of nutrient limitations. This finding is in agreement with previous work[98,99,126]. Differentiation under discontinuous media perfusion was shown to promote differentiation of pMNs, MNs, and OPCs, although not to the level of plate controls. In addition, the discontinuous media perfusion frequency and concentrations of small molecules added to the media were identified as parameters influencing the amount of pMNs generated. We proposed that discontinuous media perfusion better supported differentiation by allowing accumulation of cell-secreted factors required for cellular processes associated with growth and differentiation. These findings provide a basis of

understanding how microfluidic media exchange conditions modulate growth and differentiation of mESC aggregates.

These studies also highlighted a disadvantage of using PDMS as a material for microfluidic cell culture. It is well-known that PDMS can absorb small molecules, particularly hydrophobic molecules[131]. However, the many advantages of using PDMS, including optical clarity, ease of fabrication, and cost still make it an attractive material for use in microfluidic devices for cell culture. Thus, care should be taken in design of any PDMS-based cell culture system to address this particular disadvantage of PDMS. Our results demonstrate that PDMS absorption of small hydrophobic molecules can be partially compensated for by altering concentration and delivery frequency of those molecules.

Finally, these studies revealed how asymmetrical microfluidic device geometries can be used to create local gradients of soluble factors and influence phenotypes spatially. The data demonstrated that diffusion-dominated media exchange in aggregate traps could create local concentration differences in soluble molecules and that these could influence spatial patterns of pMN differentiation. This effect was dependent on media perfusion frequency. This finding has implications for applications in spatial patterning of tissues and understanding how symmetry-breaking events occur during embryonic development.

CHAPTER 4 : DESIGN AND VALIDATION OF A PLATFORM FOR CULTURE AND ASSESSMENTS OF BRAIN ORGANOIDS

In this chapter, miniaturized platforms for culture and assessments of forebrain organoids were developed. The platforms enable culture of organoids in individual chambers, controlled delivery of media and reagents, access for imaging-based assays, and retrieval of organoids for end-point based assays. Use of the platforms for generation of forebrain organoids was validated through characterization of growth, morphology, cell types, and structural features following up to 42 days of culture. This work was performed in collaboration with the lab of Dr. Zhexing Wen at Emory University.

4.1 Introduction

Studying human brain development and disease is challenging because of the lack of robust human-specific models. Animal models have been used widely to gain insights into brain development; however, many diseases are difficult to recapitulate in animal models, and the lack of human-specific physiology has limited translation of findings from animal models to the development of therapeutics. Recently, methods have been developed to generate three-dimensional (3D) models of human brain tissues from induced pluripotent stem cells (iPSCs)[52]. These models, termed cerebral organoids, rely on the self-organizing capabilities of iPSCs and recapitulate key tissue-specific features of cellular assembly, integration, and organization. Because of their unique properties, cerebral organoids provide an exciting opportunity to model human brain development and disease.

Despite the exciting potential of cerebral organoids, there are a number of major challenges that limit their wide applicability. One challenge is the low-throughput, time-

consuming, and costly nature of organoid culture procedures. Protocols for organoid formation and culture require manual manipulations, such as the embedding of individual organoids in Matrigel. Commonly used culture formats include spinning bioreactors[52], tissue culture plates, miniaturized spinning bioreactors[56], and multiwell plates. Spinning bioreactors require large volumes of costly media and take up significant space, which is prohibitive for screening. Alternatives such as miniaturized spinning bioreactors, tissue culture plates, and multiwell plates allow use of smaller media volumes and multiplexing but still present cost and space issues for large-scale screening.

A second challenge is the extensive heterogeneity observed among cerebral organoids. Within cultures, organoids vary widely in terms of features such as size, diversity of cell types present, and structural features. This variability complicates quantitative analyses and limits applicability of cerebral organoids in screening. Understanding how to generate cerebral organoids more robustly is an active area of research, but there is still a lack of understanding of the mechanisms governing organoid formation and how heterogeneity can be controlled.

A third challenge associated with current cerebral organoid technologies is the inability to perform *in situ* phenotypic and functional assays. Typically organoids are assessed in end-point based assays. These include immunostaining in intact organoids or slices to assess protein expression, cell types, and structural features. Techniques such as RNA sequencing to assess transcriptomic information are also used. Imaging-based end-point assays are currently not incorporated in culture platforms. However, doing so would save time and labor associated with manipulating individual organoids and make it easier to correlate information collected at multiple time points during culture. Additionally,

development of imaging-based methods to assess development of live organoids during culture is necessary for betting assessing organoid development and performing large scale screens.

Micro- and mesoscale technologies are well-suited to address many of the challenges associated with generation and study of cerebral organoids. Reducing the size of the culture platform improves scalability: more experimental conditions can be assessed at once because conditions can be multiplexed, and less space is required to scale the number of cultures performed in parallel. The capabilities of microfluidics for spatiotemporal control of the cell culture environment can also be leveraged. Microfluidics provides the ability to precisely control delivery of media and reagents to cell cultures at defined rates and frequencies—something that cannot be done with conventional culture methods. Microfluidic technologies are also compatible with almost all modes of microscopy, and microscopy and immunocytochemistry are particularly useful for assessments of organoids.

Although there is a large body of literature in microfluidic technologies for culture of cell aggregates, culture of cerebral organoids presents unique considerations. Organoids grow much larger than other types of cell aggregates, up to a few millimeters in diameter, requiring meso-scale geometries. Additionally, method of media exchange is important in order to delivery sufficient nutrients to these large tissues[128,134]. To date, very few publications have reported development of a microfluidic platform for cerebral organoid culture, or culture of any organoid type. Zhu et al.[89] developed an array of micropillars in which they could both form and culture cerebral organoids. A key feature of the platform is the ability to embed the organoids in Matrigel in the platform without

the need for manual manipulations required by conventional embedding methods. One drawback of this culture system, however, is that individual organoids cannot be exposed to different conditions, a feature which is desired for screening of different drugs or compounds. Additionally, while the pillar distance can be tuned for formation of organoids of defined sizes, the pillar spacing required for formation will constrict size of organoids during long-term culture. Wang et al.[90,91] developed a microfluidic platform in which organoids could be cultured in a center chamber, embedded in Matrigel, surrounded by two side channels for diffusive delivery of media and drugs. The disadvantage of this platform design is also that organoids are not individually addressable for screening.

In this chapter, we present a microfluidic platform for culture and screening of brain organoids. We focused specifically on culture of forebrain organoids which can be used to study a variety of developmental disorders.[56] A close collaboration with Dr. Zhexing Wen at Emory University, who studies brain and forebrain organoids, motivated this decision. The platform developed in this chapter enables culture of organoids in individual chambers, controlled delivery of media and reagents, access for imaging-based assays, and retrieval of organoids for end-point based assays. With the first iteration of the platform design, we demonstrated culture of forebrain organoids for up to 42 days. Characterization of organoid size, morphology, cell types, and structural features revealed that organoids cultured in the microfluidic platform developed comparably to conventional methods. We then developed a second iteration of the platform design, which provides the ability to fluidically isolate individual organoids, is easily configurable for screening of multiple compounds in a single device, and has a scalable

design based on the footprint of a 96-well plate. We validated forebrain organoid culture in this second design and characterized organoid size and morphology. Together, the work presented in this chapter establishes a novel microfluidic-based platform technology for culture and assessments of forebrain organoids. This technology sets an important basis for future work focusing on developing ways to more robustly generate organoids and on large-scale screens of organoids for studying human brain development and disease.

4.2 Materials and Methods

4.2.1 Device Fabrication

4.2.1.1 General Fabrication Method

Device designs were drawn in SolidWorks, and molds for the devices were made using 3D printing by the company Protolabs. Protolabs was consulted in choosing the materials for the molds, based on minimum feature size and size of the entire device footprint. Molds for the first generation design were printed in the material MicroFine Green to accommodate the minimum ~200 μm feature size of the design. Molds for the second generation design, which had a minimum 600 μm feature size, were printed in the material Accura SL 5530, which was cheaper and could accommodate the larger device footprint.

Using the 3D printed molds, microfluidic devices were fabricated in polydimethylsiloxane (PDMS) (Dow Corning Sylgard 184, Midland, MI) by soft lithography.[71] Molds were not pre-treated prior to use. PDMS was mixed in a 10:1 ratio of pre-polymer and crosslinker, degassed to remove air bubbles, poured on the master mold, degassed a second time to remove remaining bubbles, and cured for approximately 24 hours at 40°C. This lower curing temperature was conservatively chosen to avoid

warping of the molds over time. The heat deflection temperatures of MicroFine Green and Accura SL 5530 are 59°C and 70°C, respectively. Following curing, PDMS devices were peeled off of the master molds.

4.2.1.2 Fabrication Specific to the First Device Design

For the first device design, PDMS was poured on the mold to a height of 5 mm to define the height of the culture chamber. Following curing and peeling, the cylindrical chambers were made by manually punching holes with a 5 mm biopsy punch (VWR). Inlet and outlet holes were punched with a 1 mm biopsy punch (VWR). Devices were thermally bonded to a piece of PDMS to seal the side of the culture chambers opposite the fluidic channels.

4.2.1.3 Fabrication Specific to the Second Device Design

The second device design required two-layer PDMS fabrication. The mold for both layers was identical, however. For the bottom layer of features, PDMS was poured on the mold to a height of 5 mm to define the height of the culture chamber. For the top layer of features, the height of the PDMS was not critical but was typically poured to ~2 mm in height. Following curing and peeling, cylindrical chambers were made in the bottom feature layer by manually punching holes with a 5 mm biopsy punch (VWR). The top and bottom PDMS layers were then plasma bonded together and left in an oven at 75°C overnight to strengthen the bond. Inlet and outlet holes were punched with a 1 mm biopsy punch (VWR).

4.3.1.4 Fabrication of Clamp for Device Sealing

Clamps used to seal devices were fabricated from acrylic. Sheets of clear, 3 mm thick acrylic (McMaster-Carr) were cut with a laser cutter. Clamps were fabricated with holes for screws to tighten and holes to allow device tubing connections to pass through one side.

4.2.3 Transport Modeling

COMSOL computational fluid dynamic (CFD) software was used to model laminar flow and mass transport within the devices. In all simulations, the 2D steady state solution for the incompressible Navier-Stokes equation was first solved for. This solution was then used in the 2D steady state model for combined convection and diffusion mass transport of a dilute species. Fluid properties were assumed to be those of water. For laminar flow, a no slip boundary condition was assumed at all channel walls. The inlet velocity was calculated based on the volumetric perfusion rate used. The outlet boundary condition was set as an open boundary condition with pressure equal to zero. For mass transport, a no flux boundary condition was assumed at all walls. The initial concentration and inlet concentration of a species was set as the concentration of that species in cell culture media. Finally, to take into account the reaction/consumption of a given species by an organoid, this was was described as the flux of that species through a 2D circular surface, representative of the organoid.

4.2.4 Forebrain Organoid Culture

Forebrain organoids were formed and cultured according to published protocols[56]. EBs were first formed from hiPSC cultures maintained in the Wen lab at University. EBs were formed by detaching hiPSC colonies with Collagenase Type IV and were cultured in ultra-low attachement 6-well plates (Corning) in media containing DMEM/F12 (Life

Technologies), 20% Knockout Serum Replacement (Life Technologies), 1X Glutamax (Life Technologies), 1X non-essential amino acids (Life Technologies), 0.1 mM 2-mercaptoethanol (Life Technologies), 2 µM A-83 (Tocris), and 2 µM Dorsomorphin (Sigma). On days 5-6, half of the media was replaced with induction media containing DMEM/F12 (Life Technologies), 1X Glutamax (Life Technologies), 1X non-essential amino acids (Life Technologies), 1X Penicillin/Streptomycin (ThermoFisher), 1X N2 Supplement (ThermoFisher), 1 µM CHIR 99021 (Cellagen Tech), and 1 µM SB-431542 (Cellagen Tech). At day 7, organoids were embedded in individual drops of Matrigel (Corning) and cultured in induction media in 6-well plates until day 14. At day 14, Matrigel was mechanically dissociated from organoids by pipetting with a 5 mL serological pipette. Organoids were then transferred to microfluidic devices or low attachment tissue culture plates for the remainder of culture. From day 14 on, organoids were cultured in differentiation media containing DMEM/F12 (Life Technologies), 1X N2 and B27 Supplements (ThermoFisher), 1X Glutamax (Life Technologies), 1X non-essential amino acids (Life Technologies), 1X Penicillin/Streptomycin (ThermoFisher), 0.1 mM 2-mercaptoethanol (Life Technologies), and 2.5 µg/mL insulin (Sigma Aldrich). For culture in plates, approximately 50 organoids were cultured per plate with 10 mL of media. Media was exchanged every other day.

4.2.5 Organoid Culture in Microfluidic Devices

Prior to each experiment devices, fittings (blunt 16 gauge needles; McMaster-Carr), and tubing (1/32" ID silicone tubing; Cole Parmer) were sterilized by autoclaving. The day prior to organoid loading, devices were treated with air plasma to render the PDMS hydrophilic. After treatment, devices were immediately primed with PBS to

maintain the hydrophilicity and then re-sterilized with UV light for 30 minutes. Devices were then placed in a cell culture incubator overnight.

Prior to organoid loading, devices were primed with differentiation media. Organoids were loaded into individual chambers of the device by pipetting. Following loading of organoids into individual chambers, devices were pressed against a sterile glass slide (VWR) to seal the chambers and channels. The device and glass slide were then placed between two laser cut pieces of acrylic, and screws and nuts were used to tighten the entire assembly. Finally, primed tubing and fittings were connected to the device inlet and outlet. A 0.2 µm syringe filter was connected at the end of the outlet tubing to maintain sterility. Device inlets were connected to syringes and a syringe pump (PHD 2000; Harvard Apparatus), and the entire setup was placed in a humidified incubator (HERAcell 240i, Thermo Scientific for culture.

4.2.6 Live Imaging and Quantification

Bright field and phase contrast images of devices were acquired at weekly time points during culture using either a dissecting scope or an EVOS microscope. Organoid size and eccentricity were quantified from images using manual segmentation in ImageJ.

4.2.7 Immunohistology, Imaging, and Quantification

Organoids were prepared for immunohistology and imaging as described previously.[56] Organoids were collected from microfluidic devices or tissue culture plates and fixed in 4% Paraformaldehyde in PBS for 1 hour at room temperature. Organoids were then washed in PBS and incubated in 30% sucrose overnight. Organoids were embedded in optimal cutting temperature compound (OCT) and sectioned with a cryostat. For immunostaining, slices were permeabilized with 0.2% Triton-X for 1 hour and then

washed with blocking buffer containing 10% donkey serum and 0.1% Tween-20 in PBS for 30 minutes. Next, slices were incubated in primary antibodies in blocking buffer overnight at 4°C. Slices were washed with PBS and incubated with secondary antibodies in block buffer for 1 hour. Slices there then washed in PBS and incubated with DAPI. Images were collected on an epifluorescent microscope. Quantification of imaging data was performed both manually and with custom code in the Wen lab.

4.3 Results and Discussion

4.3.1 Design of First Generation, Diffusion-Based Microfluidic Device

The device consists of an array of 30 culture chambers, connected by channels for delivering media and reagents (**Figure 4.1a**). The culture chambers are 5 mm in diameter and 5 mm in height, large enough to support the maximum size that forebrain organoids reach at 80 days of culture and longer. The media delivery channels connect to the top of the culture chambers (**Figure 4.1b**), so mass transport between the channels and the culture chambers is primarily diffusion-based. The value of having the channels connect to the top of the chambers is that it enables the device to be fabricated in a single layer. The media delivery channels are designed such that all organoids are exposed to the same media composition. A large, 0.7mm wide serpentine channel connects all of the chambers, and smaller, 0.2 mm wide cross-flow channels connect adjacent columns of the device (**Figure 4.1a)**. Transport modeling analysis showed, as will be described in the following section, that with this channel configuration organoids were not exposed to significantly different concentrations of nutrients or metabolites. Therefore, we deemed this channel configuration acceptable for the purposes of validating the platform.

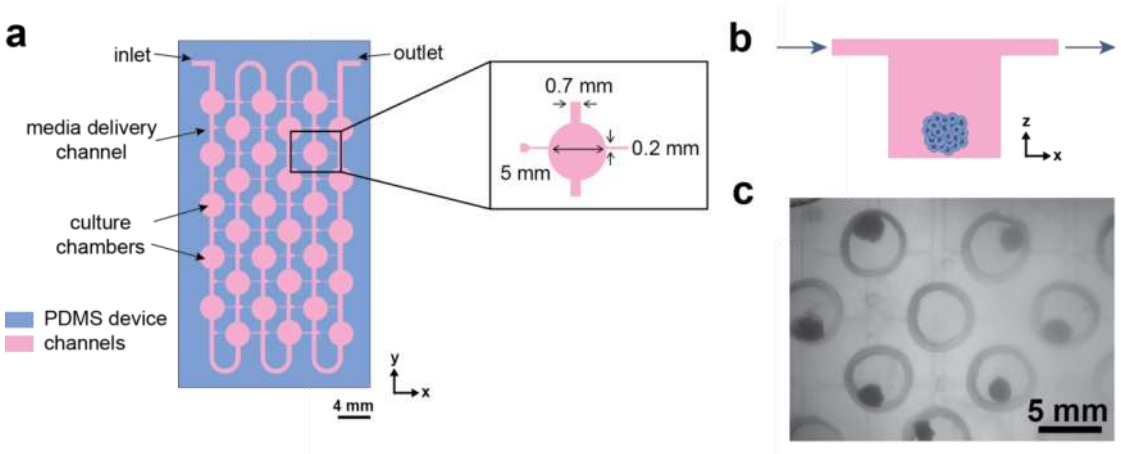

Figure 4.1. Design of the microfluidic platform for organoid culture. a) Schematic illustrates the design of organoid culture device in a top-down view, with inset depicting key trap and channel geometries. b) Schematic depicts a side view of a single chamber and channels for media delivery. c) Bright field image of chambers with organoids.

Organoids were manually loaded into the individual chambers of devices using a pipette (**Figure 4.2**). Devices were then reversibly sealed to a glass slide using two outer pieces of acrylic tightened with screws. Live imaging during culture could be performed through the acrylic and glass. The entire device assembly was kept in a standard cell culture incubator during culture, and media was delivered at defined rates or frequencies using a syringe pump.

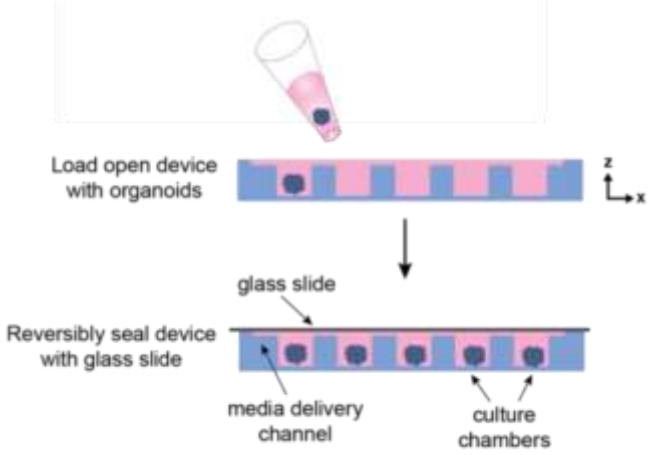

Figure 4.2. Device loading and assembly. Schematic depicts a side view of the device. Aggregates are loaded into devices with a pipette tip, and then devices are clamped against a glass slide for culture.

4.3.2 Transport Modeling in First Generation Device Design to Inform Optimization Operating Conditions

4.3.2.1 Overview

Since forebrain organoids grow to millimeters in size, they consume significant amounts of nutrients and oxygen and require frequent media changes. In order to understand how device operating conditions could be optimized for sufficient delivery of nutrients and removal of waste, an approach using computational fluid dynamic (CFD) modeling in COMSOL was performed. We modeled conditions within the organoid culture device and compared those to conditions in a miniaturized spinning bioreactor, the SpinΩ[56]. The SpinΩ consists of a 12-well plate modified to include spinning impellers in each well to agitate the media. It is the current state-of-the-art platform for culture of forebrain organoids. In choosing what operating conditions to model in the organoid culture device, we hypothesized that continuous perfusion of media through the device would best support organoid growth. In this design, mass transfer is diffusion-dominated, so effects of continuous perfusion on removing cell-secreted factors are minimal. Overall, the modeling results presented in the following sections should be interpreted as general guidelines for ranges of operating conditions that support organoid survival and growth. Experimental validation was essential to confirming appropriate operating conditions.

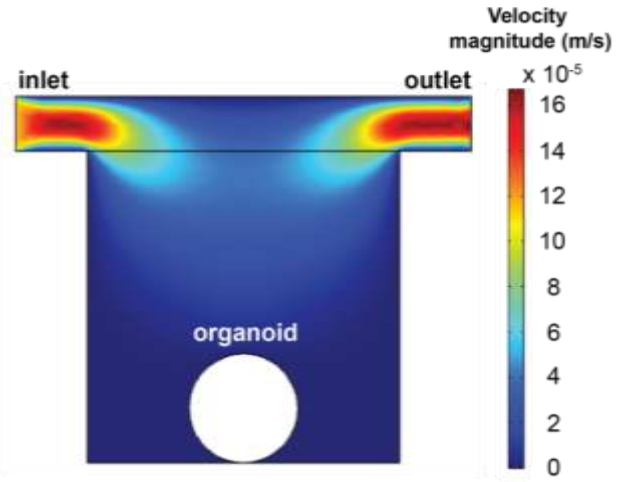

Figure 4.3. Depiction of how one chamber of the device was modeled. The geometry reflects a 2D side view of a single chamber with inlet and outlet channels. The organoid is modeled as a 2D circle centered at the bottom of the chamber. The heat map shows the velocity profile in the chamber for an inlet flow rate of 100 µL/hr.

A 2D cross-section of an individual culture chamber was modeled with a single inlet and outlet (**Figure 4.3**). The organoid was modeled as a circle located at the bottom of the culture chamber, and cell secretion and consumption were modeled as flux through the perimeter of the circle. We selected a few representative species to model: glucose, oxygen, a small molecule media additive, and lactate. Transport properties for each species were obtained from literature. Cell consumption and production rates of the different species were also obtained from or estimated based on literature. Values for each of these and corresponding references are shown in **Table 4.1**. To estimate the cell density within a forebrain organoid for calculating consumption and production rates, we used a value reported in literature for cerebral organoids: 4.8×10^{14} cells m^{-3} [128]. This value corresponded with our own measurements of cell densities in forebrain organoids at day 21 (data not shown).

Table 4.1. Values for transport and reaction of key species.

Species	Diffusion Coefficient ($m^2\ s^{-1}$)	Initial Concentration ($mol\ m^{-3}$)	Consumption/ Production Rate ($mol\ cell^{-1}\ s^{-1}$)	References
Glucose	6×10^{-10}	17.49	2×10^{-18}	128,135
Oxygen	3×10^{-9}	0.2	2×10^{-18}	128,136
Lactate	3.5×10^{-10}	0	2×10^{-16}	136-138
Small molecule	3.8×10^{-10}	2×10^{-3}	1×10^{-22}	129

4.3.2.2 Glucose Transport and Consumption

In order to assess what media perfusion rate was needed to supply organoids with sufficient amounts of nutrients, we modeled transport and consumption of glucose. We assessed media flow rates ranging from 25 - 400 μL hr^{-1} and organoid sizes from 0.6 mm to 2.0 mm in diameter. These organoid sizes were within the range expected for culture time periods of ~40 days or more. As shown in **Figure 4.4a**, modeling indicates that organoids up to 1.6 mm in diameter experience steady state glucose concentrations within 90% of the initial concentration for all media flow rates modeled. These results indicate that relatively low media perfusion rates can be used for organoids up to 1.8 mm in diameter.

For comparison, glucose consumption in the state of the art culture system for forebrain organoids, the SpinΩ bioreactor, was also modeled. To model this geometry, we modeled 2 mL of media in a single well of a 12-well plate, assuming it to be well-mixed. For glucose consumption rates, we assumed there to be 20 organoids in the well. Calculating the glucose concentration in the SpinΩ over the 48 hour period between media changes (**Figure 4.4b**) showed that the glucose concentration drops below 90% of

the initial concentration by 24 hours for organoids that are 1.6 mm in diameter or larger. These modeling results indicate that organoids in the SpinΩ (and likely in similar culture formats) see large variances in glucose concentration between media changes, particularly for organoids 1.6 mm and larger. Remaining within 90% of the initial concentration is therefore perhaps an overly stringent requirement for the microfluidic platform. Additionally, these results suggest that microfluidic culture has the potential to maintain better consistency in nutrient concentrations over culture periods.

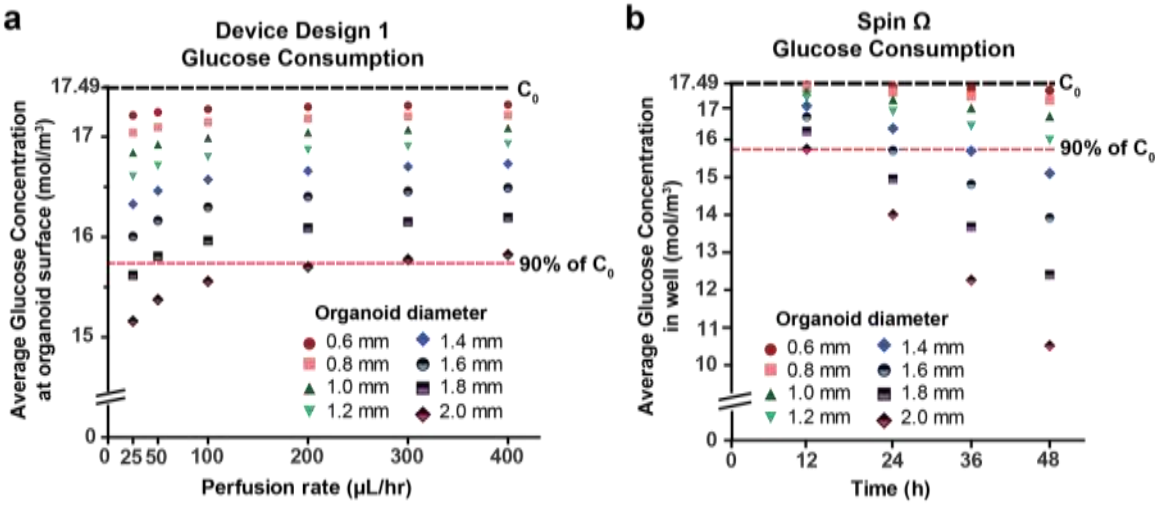

Figure 4.4. Glucose transport and consumption. a) Graph shows average glucose concentration at organoid surface for a range of organoid sizes and media perfusion rates. b) Graph shows the change in average glucose concentration in one well of the SpinΩ bioreactor over a 48-hour period for a range of organoid sizes.

4.3.2.3 Oxygen Transport and Consumption

We next modeled transport and consumption of oxygen in the microfluidic device. PDMS is oxygen permeable, so diffusion of oxygen through the PDMS was considered. The geometry of the CFD model in COMSOL was altered to consider oxygen transport in the PDMS, as shown in **Figure 4.5a**. A single column of the device, with five culture chambers in series was modeled. The device is clamped to glass with an acrylic clamp, so the only portions of the PDMS assumed to have oxygen exchange with the

atmosphere were the left and right edges. Results from the center chamber are reported here, as the "worst case scenario" of oxygen concentration, since that chamber is the farthest from the edges of PDMS exposed to the atmosphere. For modeling oxygen transport in the SpinΩ bioreactor, diffusion of oxygen from air to the media was considered. The well of the bioreactor was assumed to be well-mixed.

Results from modeling oxygen transport and consumption for the center chamber, as shown in (**Figure 4.5b**), indicate that organoids experience oxygen concentrations below 90% of atmospheric oxygen for all perfusion rates modeled. In particular, the modeling results suggest that organoids greater than 1.4 mm completely deplete oxygen at their surface. It is important to note that organoids approximately 1.0 mm in diameter and smaller do experience oxygen concentrations above what is considered hypoxic conditions (5% oxygen, equivalent to 0.065 mol m^{-3}) for perfusion rates of 100 μL hr^{-1} and higher. Many reports in literature suggest that hypoxic conditions are preferential for culture of many cell types[139-141] including stem cells. Therefore oxygen conditions experience by smaller organoids (< 1.0 mm) may be sufficient for supporting growth and differentiation. In comparison, in the SpinΩ organoids all experience oxygen concentrations below 90% of the initial value (**Figure 4.5c**). However, oxygen concentrations remain relatively constant between media exchanges after an initial decrease, and organoids up to 1.8 mm do not experience conditions below what is considered hypoxia.

Overall, these results suggest that oxygen is potentially a limiting nutrient in the microfluidic culture platform, and organoids may experience hypoxic conditions. It is likely that the CFD model somewhat over-estimates oxygen consumption because the

organoid geometry is assumed to be that of an infinite cylinder in the model. In the future, 3D CFD models could be used to reduce this over-estimation. Nevertheless, these results suggest that potential effects of oxygen limitations on organoid phenotypes need to be monitored. Various strategies could also be used to increase oxygen delivery in the device. One method to increase oxygen delivery would be to dissolve a higher concentration of oxygen in the media before infusion into the device.

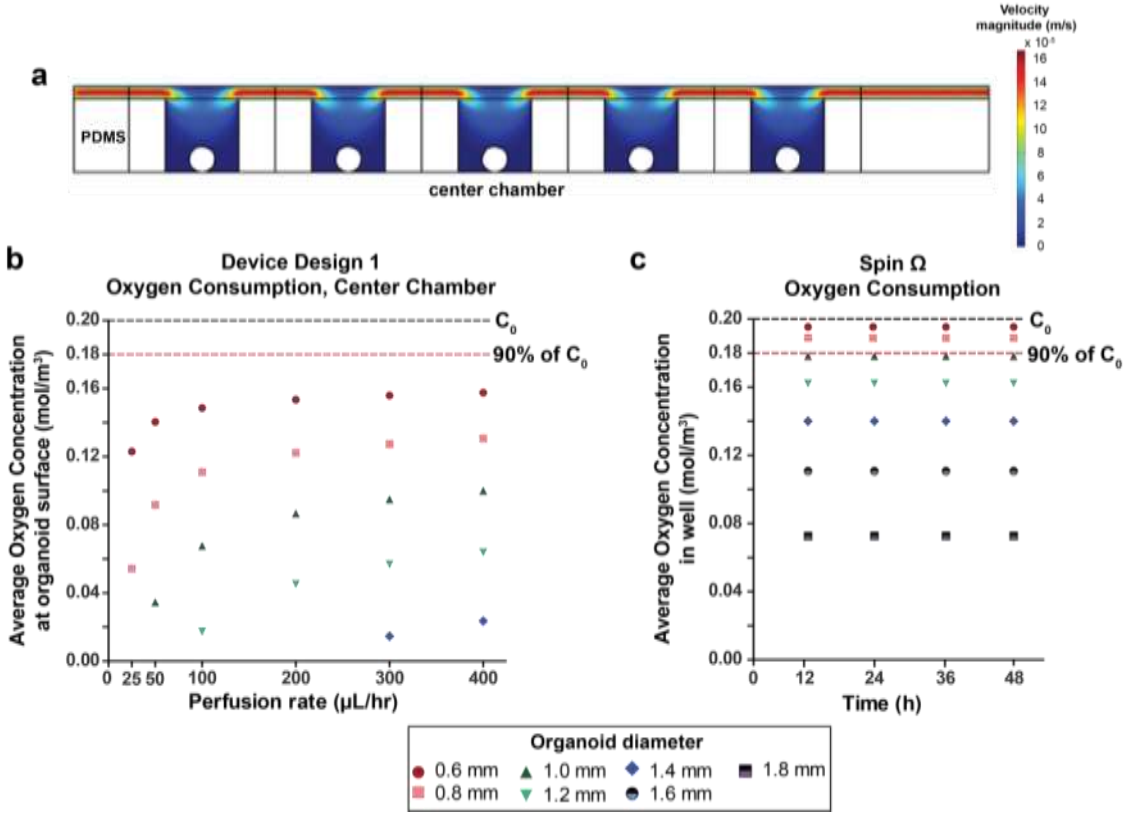

Figure 4.5. Modeling oxygen transport and consumption. a) Geometry used to model oxygen transport and consumption in the first generation microfluidic device. The heat map shows the velocity profile for a flow rate of 100 µL/hr. b) Graph shows average oxygen concentration at organoid surface in the center of five chambers in series for a range of organoid sizes and media perfusion rates. c) Graph shows the change in average oxygen concentration in one well of the SpinΩ bioreactor over a 48-hour period for a range of organoid sizes.

4.3.2.4 Small Molecule Media Additive Transport and Consumption

We next assessed transport and consumption of a small molecule media additives. Small molecules are typically added to media to activate or inhibit signaling pathways to promote differentiation. Examples of small molecules used in the forebrain organoid differentiation protocols include CHIR 99021, as glycogen synthase kinase 3beta (GSK3β) inhibitor, and SB-431542, a transforming growth factor beta (TGFβ) pathway inhibitor. The same approach as used for glucose was used for modeling transport and consumption of a small molecule. For all perfusion rates and organoid sizes modeled, organoids in the microfluidic device experience within 90% of the inlet concentration of a representative small molecule (**Figure 4.6a**). In comparison, in the SpinΩ, the concentration drops below 90% of the inlet concentration for 1.6 mm and 2.0 mm organoids towards the end of each media exchange (**Figure 4.6b**). These results indicate that microfluidic perfusion at a range of rates is sufficient for delivery small molecules to the organoids, and that microfluidic perfusion can be used to maintain more temporally uniform concentrations compared to the SpinΩ.

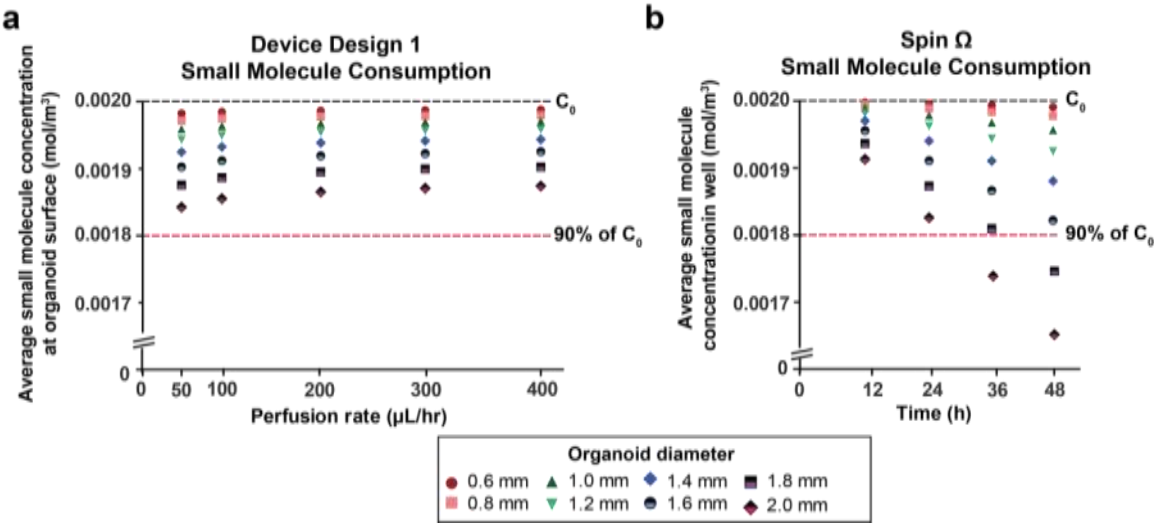

Figure 4.6. Small molecule transport and consumption. a) Graph shows average small molecule concentration at organoid surface for a range of organoid sizes and media perfusion rates. b) Graph shows the change in average small molecule concentration in one well of the SpinΩ bioreactor over a 48-hour period for a range of organoid sizes.

4.3.2.5 Lactate Transport and Secretion

Lactate is one type of metabolic waste produced by cells, so we next assessed whether microfluidic perfusion could adequately remove lactate from the culture chambers. We modeled lactate transport and secretion as with the other types of molecules assessed, but with a cellular production term instead of consumption. In microfluidic devices, steady state lactate concentrations range from 300 – 400 mol m^{-3} for 2.0 mm aggregates (**Figure 4.7a**). In comparison, in the SpinΩ lactate levels can reach as high as 700 mol m^{-3} by 48 hours after a media exchange (**Figure 4.7b**). Based on the comparison of maximum lactate levels in the device versus SpinΩ culture, we concluded that microfluidic perfusion sufficiently removes lactate.

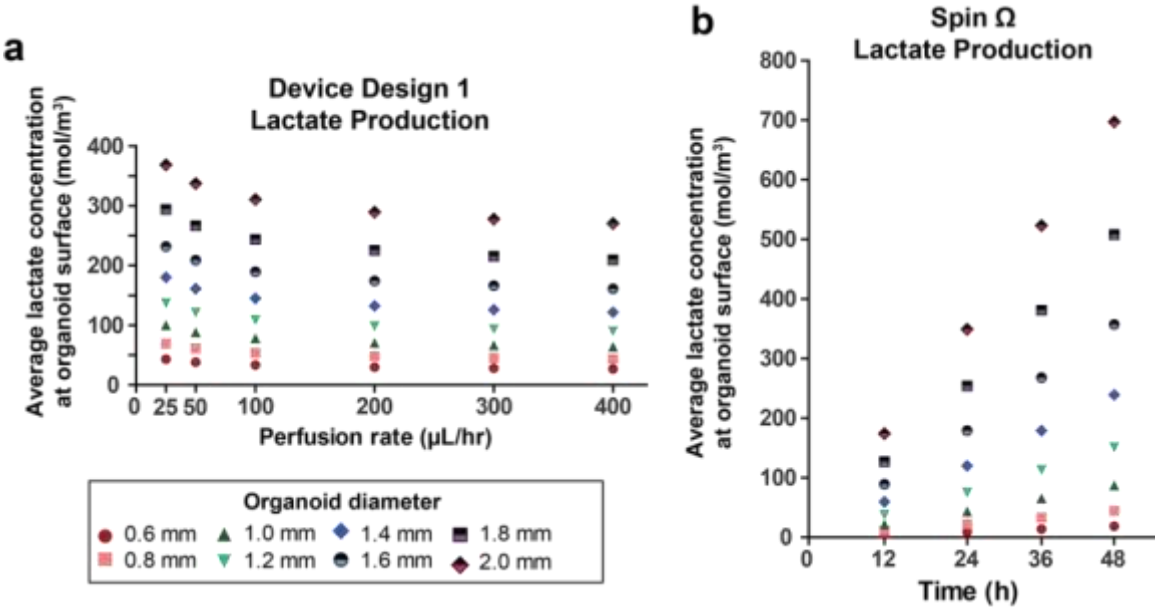

Figure 4.7. Lactate transport and secretion. a) Graph shows average lactate concentration at organoid surface for a range of organoid sizes and media perfusion rates. b) Graph shows the change in average lactate concentration in one well of the SpinΩ bioreactor over a 48-hour period for a range of organoid sizes.

4.3.2.6 Differences in Species Concentrations Among Culture Chambers

One element of the first generation organoid culture device design is that media passes serially through the culture chambers. The implication of this is that organoids downstream in the device could potentially experience lower concentrations of molecules that are consumed and higher concentrations of molecules that are secreted. To assess this, the 30 chambers of the device were modeled in series. We made the assumption that media only flowed through the main serpentine channel. This assumption describes the worst case scenario: while the majority of the volumetric flow travels through the main serpentine channel, a small portion travels through the narrow channels between adjacent columns in the device. Based on this model, we assessed the average concentration of glucose, a small molecule, and lactate in each of the 30 culture chambers of the device. In **Figure 4.8**, the concentrations of these species at the organoid surface, in the entire chamber, and at the chamber outlet are shown for a 1.6 mm organoid and a 200 μL hr^{-1} flow rate. For glucose and a small molecule, the concentration difference between the first and last chamber is less than 10%. For lactate, the maximum concentration reached, in chamber 30, is still well below what organoids experience in the SpinΩ. Based on these results, we conclude that variations of concentrations of nutrients, small molecules, and metabolites across the device were not significant.

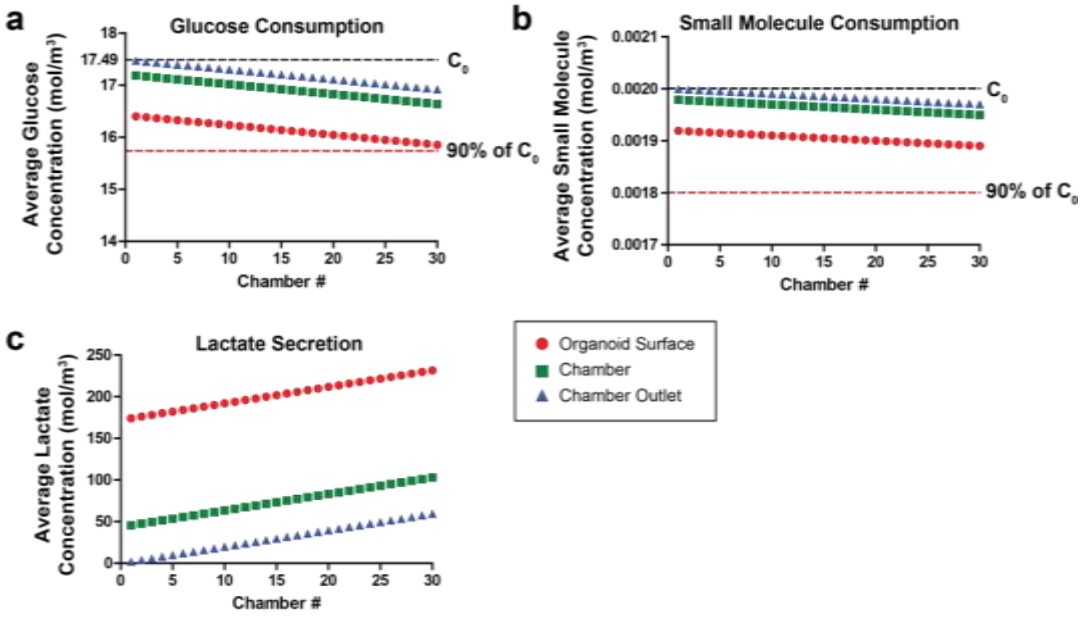

Figure 4.8. Differences in glucose, small molecule, and lactate concentrations among culture chambers. Graphs show the modeled average (a) glucose, (b) small molecule, and (c) lactate concentrations at the organoid surface, within the chamber, and at the chamber outlet for every chamber in a given device. These were modeled for a 1.6 mm diameter organoid and a 200 μL hr^{-1} media perfusion rate.

4.3.3 Testing Organoid Culture in First Generation Device Design

4.3.3.1 Overview

In order to test use of the microfluidic device for forebrain organoid culture, day 14 organoids were loaded into devices and cultured under continuous perfusion at 200 μL hr^{-1}. Day 14 was chosen for beginning microfluidic culture, as it is the point in the culture protocol at which organoids are removed from individual beads of Matrigel. The perfusion rate of 200 μL hr^{-1} was chosen based on results from the transport modeling analysis that indicated that further increasing the flow rate resulted in only small changes in concentrations of nutrients, small molecules, and metabolites. Additionally, there is a tradeoff in that higher perfusion rates use larger volumes of expensive media. As a control, forebrain organoids were cultured in tissue culture plates in static (non-agitated

media). For some time points, organoids cultured in a SpinΩ bioreactor in the Wen lab at Emory University were also available for comparison.

4.3.3.2 Organoid Size and Gross Morphology

In order to assess organoid development, size and gross morphology were assessed from bright field images acquired at weekly time points. **Figure 4.9** shows the same two representative organoids at each time point in microfluidic devices and different representative organoids at each time point in tissue culture plate controls. Organoids appeared to grow normally in devices: they displayed expected size increases, maintained a round morphology, and exhibited expected morphological features. In particular, organoids exhibited neural epithelium/neural tube-like structures that are a key feature of forebrain organoids[56] (**Figure 4.9c**). Heterogeneity was observed in terms of organoid size and morphology both in devices and in tissue culture plate controls, and this was expected.

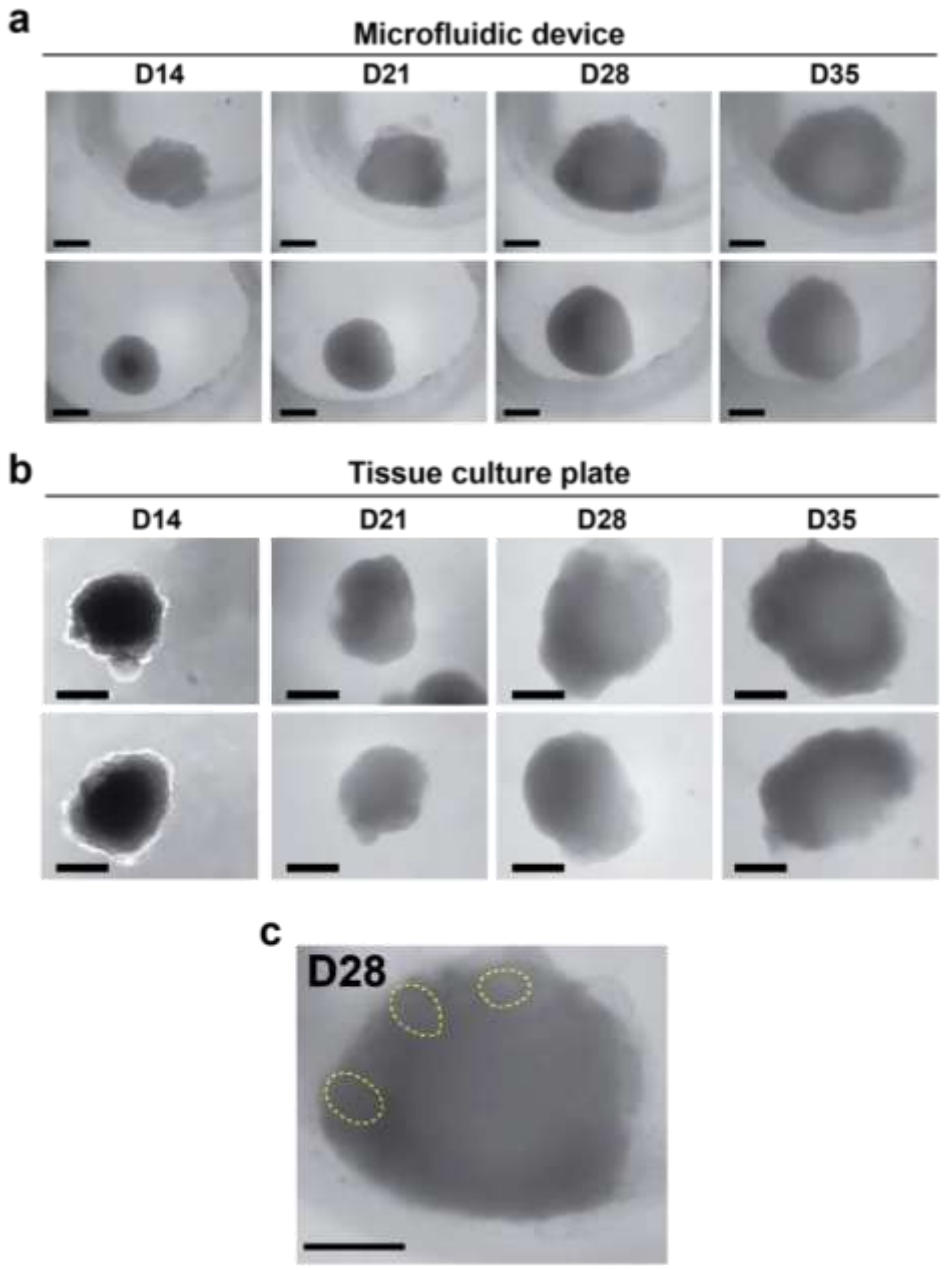

Figure 4.9. Representative bright field images of forebrain organoids. a) Images of two representative forebrain organoids culture in devices. b) Images of different representative forebrain organoids culture in tissue culture plates. c) Image of a D28 organoid cultured in device with round, neuroepithelial structures faintly visible and outlined in yellow. All scale bars: 100 µm.

In order to assess growth, organoid diameter was quantified. The cross-sectional area was measured from bright field images and then used to calculate an equivalent diameter. As shown in **Figure 4.10a**, organoids increased in size over the 35 days of

culture. Organoids cultured in devices were, on average, slightly smaller than plate controls at days 21, 28, and 35, although this difference was only statistically significant at days 28 and 35. Organoid circularity was also assessed, with a value of 1 representing a perfect circle (**Figure 4.10b**). Organoids across all conditions tended to be round, and there were no statistically significant differences between days or conditions. Growth rate was also calculated by quantifying the difference in size between two time points and normalizing the by the size at the first of the two time points (**Figure 4.10c**). Plate controls showed a higher growth rate at days 21 and 28 compared to organoids cultured in devices, but by day 35 there was little difference in growth rate. Together, based on size, morphology, and growth rate assessments, these results indicated that organoids cultured in devices developed similarly to plate controls, but with some reduction in size and growth. The size difference could be due to reduced cellular proliferation or increased cell death, and this was investigated further in the next section.

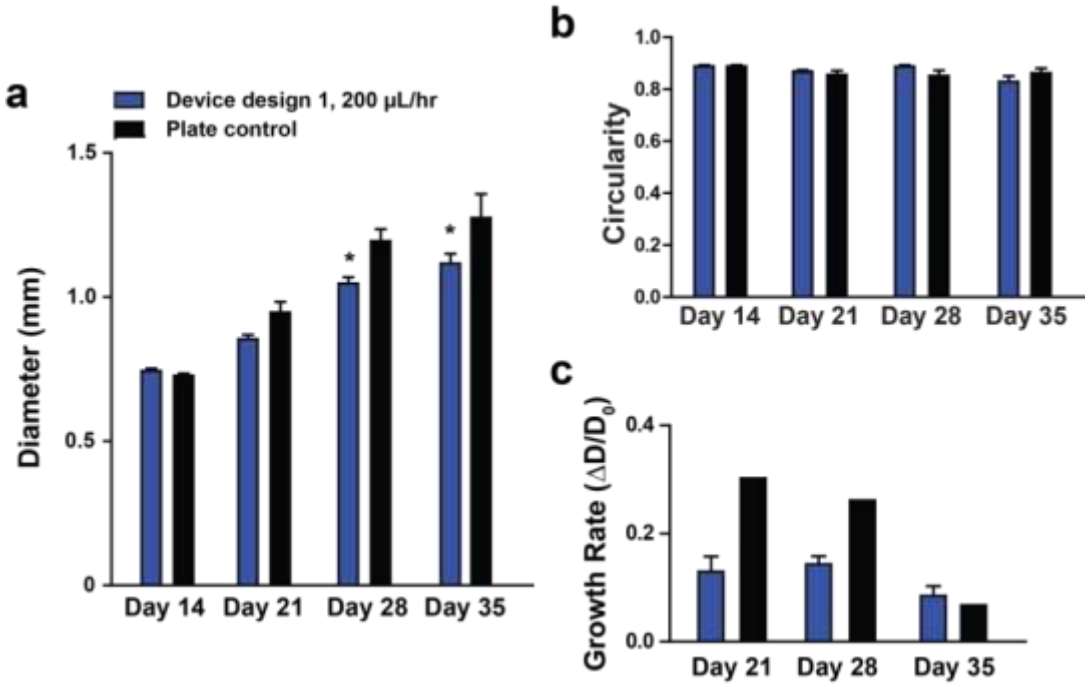

Figure 4.10. Organoid size, morphology, and growth rate. a) Organoid diameter measured at days 14, 21, 28, and 35 of culture. Diameter was calculated from the cross-sectional area of organoids in brightfield images. Two-way ANOVA with Bonferroni posttests was used; * indicates $p < 0.01$. b) Organoid circularity at days 14, 21, 28, and 35 of culture was calculated from brightfield images. Two-way ANOVA with Bonferroni posttests was used; all samples n.s. c) Growth rate was calculated, defined as the difference in size between two time points and normalized by the size at the first of the two time points. Two-way ANOVA with Bonferroni posttests was used for devices only, as plate control growth rate was calculated from population averages. For all graphs, error bars indicate SEM.

We investigated whether there was any correlation between location in the device and organoid size, even though transport modeling results suggested that different types of molecules had minimal concentration differences across the device. **Figure 4.11** shows organoid diameter plotted as a function of culture chamber number for 7 different devices from 4 independent experiments. Numbering denotes position along the main serpentine channel with chamber 1 at the device inlet and chamber 30 at the device outlet. Based on the Spearman correlation coefficient, there was no correlation between size and position. This further supports the assertion that perfusion of the media serially through the culture chambers did not have observable effects on organoid phenotype.

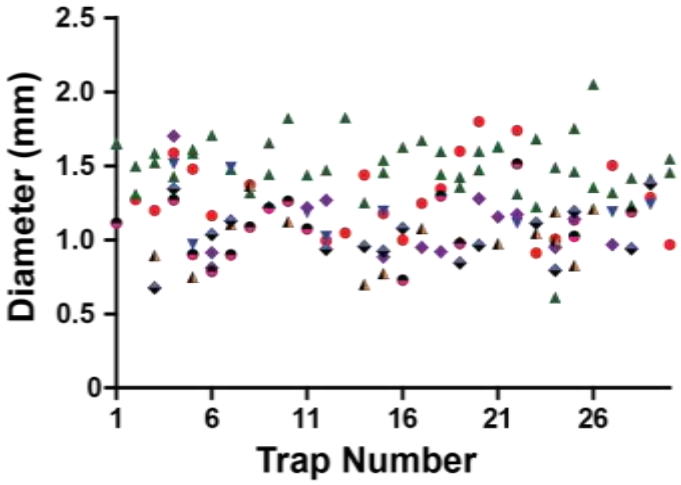

Figure 4.11. Organoid size as a function of position in the device at D35. Diameters of day 35 forebrain organoids from 7 devices from 4 independent experiments are shown, with each device indicated by a different symbol. Numbering denotes position along the main serpentine channel with chamber 1 at the device inlet and chamber 30 at the device outlet.

4.3.3.3 Immunohistological Characterization of Forebrain Organoids

We next characterized organoids by immunohistological analysis to assess if cell types and structural features characteristic of forebrain organoids were present. All immunohistology, imaging, and image analysis steps were performed by collaborators in Dr. Zhexing Wen's lab at Emory University. We first assessed the generation and proliferation of neural progenitor cells (NPCs) at days 21, 35, and 42. At all time points, organoids cultured in microfluidic devices exhibited polarized neuroepithelium-like structures resembling neural tubes containing SOX2+ NPCs (**Figure 4.12**). SOX2+ neural tube structures were also observed in plate controls at all time points and in SpinΩ cultures at day 42 (the one time point that samples were available for assessment). Interestingly, organoids cultured in plates appeared be less differentiated evidenced by the larger, less complex neural tube structures visible at day 21 and as late as day 42 (**Figure 4.12a,c**). In contrast, organoids cultured in devices and SpinΩ cultures had

smaller neural tube structures more integrated with surrounding cells, which is indicative of more mature forebrain organoid structures.

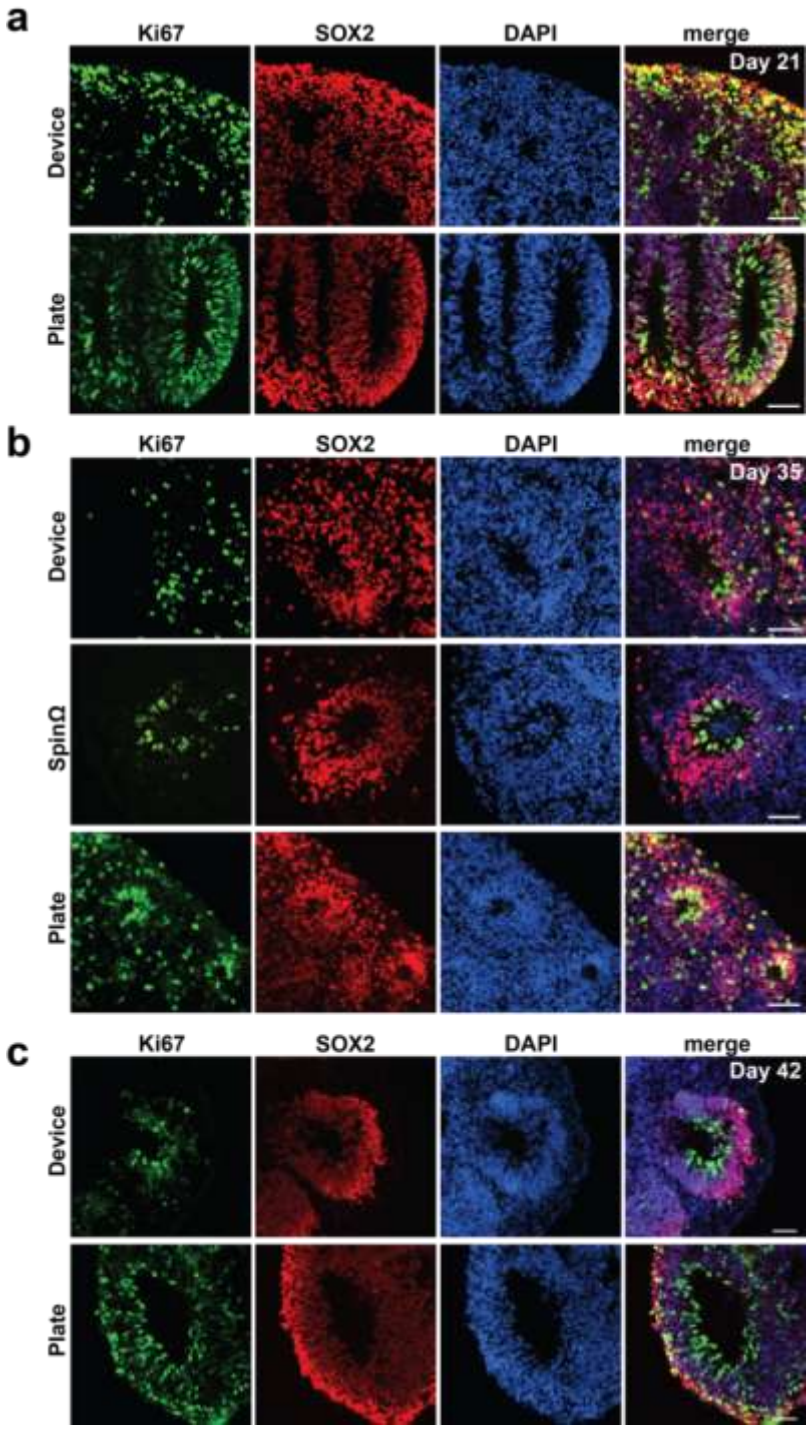

Figure 4.12. Characterization of cellular proliferation. Immunohistological analysis was performed for (a) day 21, (b) day 35, and (c) day 42 forebrain organoids cultured in devices, plate controls, or the SpinΩ bioreactor. Representative images show staining for cellular proliferation (Ki67), NPCs (SOX2), and cell nuclei (DAPI). All scale bars are

100 µm. Images are representative of 20-40 organoids per time point. 3 independent experiments for day 21, 4 independent experiments for day 35, one experiment for day 42.

As organoids mature, dividing SOX2+ NPCs start to exit the cell cycle. Ki67 staining at days 21, 35, and 42 indicated that some but not all SOX2+ cells in device organoids were mitotic (**Figure 4.12**). In contrast, in plate controls, a larger proportion of SOX2+ cells were still Ki67+. These observations were confirmed by quantification of the proportion of SOX2+ cells that were also Ki67+, as shown in **Figure 4.13**. Organoids cultured in devices had lower proportions of dividing NPCs at days 21, 35, and 42, indicating that they were more differentiated than plate controls.

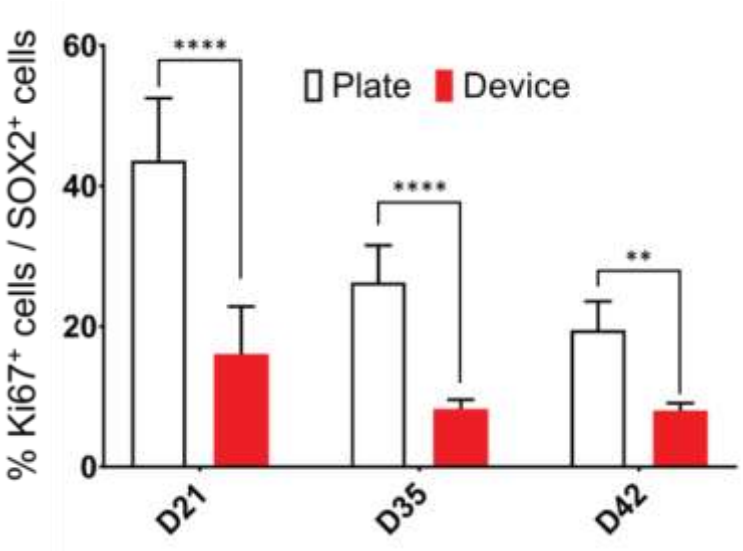

Figure 4.13. Quantification of proliferation of NPCs. The percentage of proliferating (Ki67+) NPCs (SOX2+) was quantified from immunohistology images. Data is shown for device and plate cultures at days 21, 35, and 42. Error bars indicate S.D. ANOVA was used; ** indicates $p < 0.001$; *** indicates $p < 0.0001$. Data is representative of 20-40 organoids per time point. 3 independent experiments for day 21, 4 independent experiments for day 35, one experiment for day 42.

Next, we examined differentiation of forebrain organoids by assessing expression of cortical plate layer (CP) markers TBR1 and MAP2 in addition to NPC/ventricular zone (VZ) marker SOX2 at days 21, 35, and 42. Organoids cultured in devices showed multi-

layer stratified neural tube like structures with TBR1+/MAP2+ CP structures surrounding SOX2+ VZ structures at all three time points assessed (**Figure 4.14**). These structures were also robustly observed in SpinΩ cultures at the day 35 time point that was assessed (**Figure 4.14b**). In contrast, organoids cultured in plates at day 21 had not yet developed TBR1+/MAP2+ CP layers (**Figure 4.14a**). These structures were not observed until day 35 and were also seen at day 42. (**Figure 4.14b,c**). To quantify these observations, the relative thicknesses of the VZ and CP layers were measured from images of organoids at days 21, 35, and 42. Yellow outlines in the merged images in **Figure 4.14b** shows how the regions were defined and measured. The two graphs in **Figure 4.15** plot the relative layer thickness of TBR1+ CP to SOX2+ VZ at days 21, 25, and 42. Forebrain organoids cultured both in devices and plate controls had increasing CP layer thicknesses over the three time points assessed, as expected. Additionally, device organoids had thicker CP layers at all three time points, indicative of more mature, differentiated organoids.

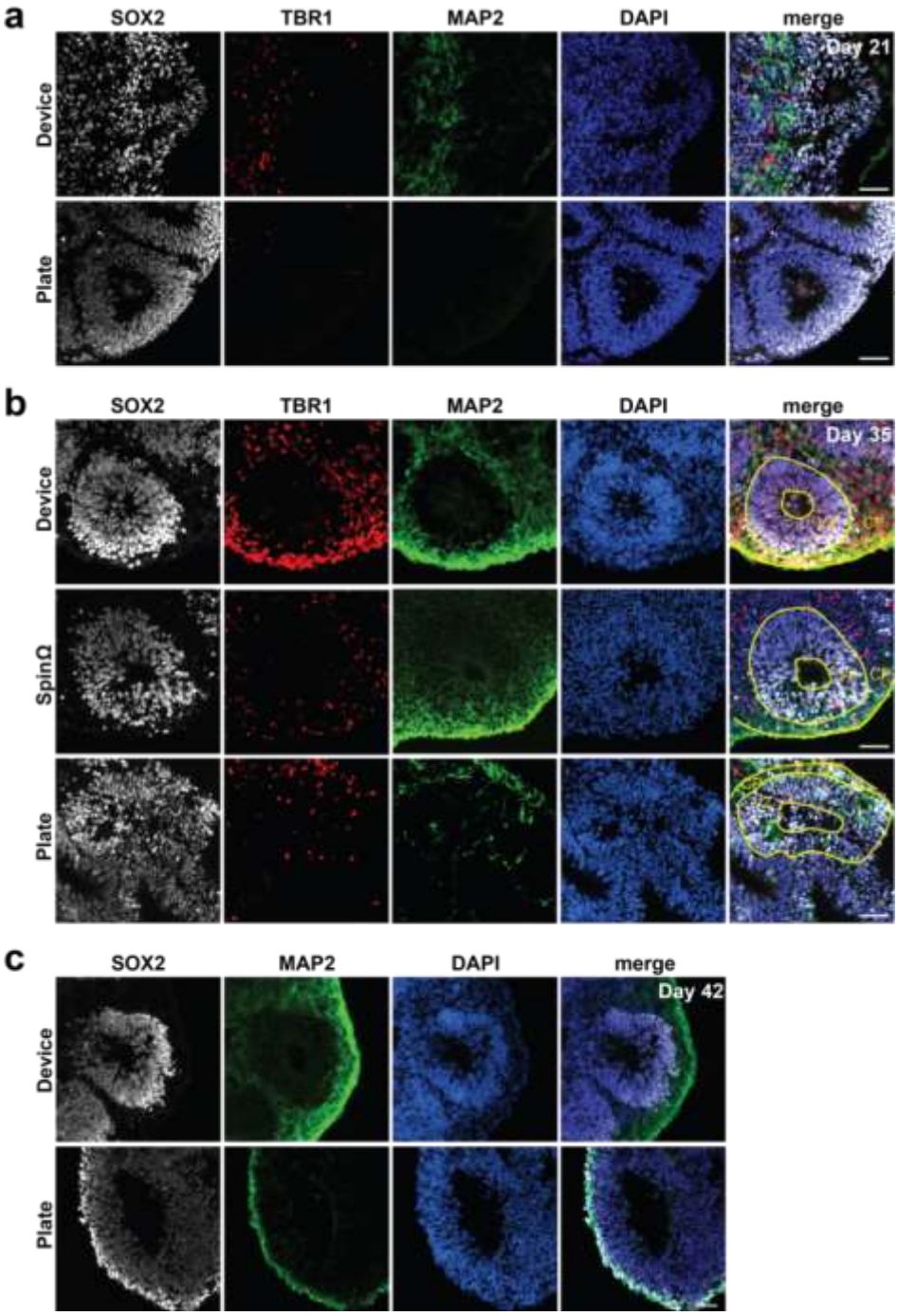

Figure 4.14. Characterization of forebrain organoid differentiation. Immunohistological analysis was performed for (a) day 21, (b) day 35, and (c) day 42 forebrain organoids cultured in devices, plate controls, or the SpinΩ bioreactor. Representative images show staining for NPCs (SOX2), cortical plate layer markers (TBR1, MAP2) and cell nuclei (DAPI). All scale bars are 100 µm. Images are representative of 20-40 organoids per time point. 3 independent experiments for day 21, 4 independent experiments for day 35, one experiment for day 42.

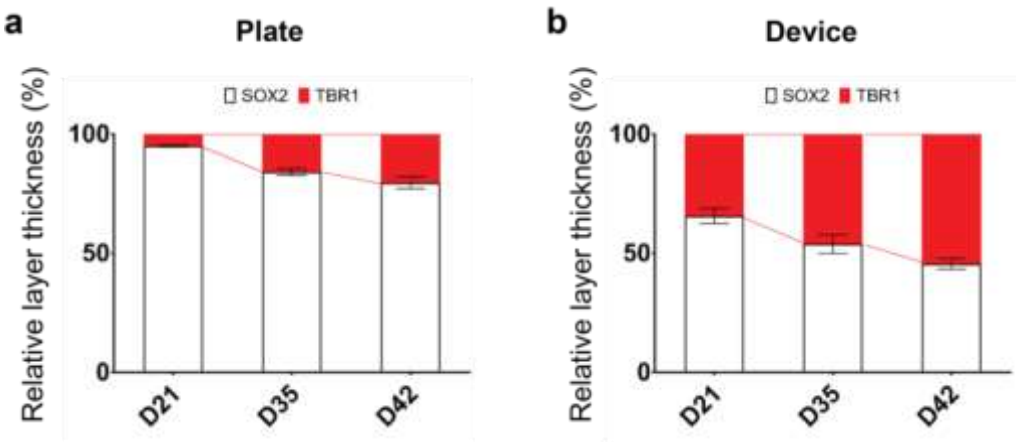

Figure 4.15. Quantification of VZ and CP layer thickness. The relative thicknesses of VZ (SOX2+) and CP (TBR1+) layers were quantified from immunohistology images. Data is shown for (a) device and (b) plate cultures at days 21, 35, and 42. Error bars indicate S.D. Data is representative of 20-40 organoids per time point. 3 independent experiments for day 21, 4 independent experiments for day 35, one experiment for day 42.

We next examined cell death in forebrain organoids through assessment of both bright field images and caspase-3 (CASP3) staining. Organoids were assessed by bright field microscopy at days 21, 35, and 42 and manually categorized as "intact", indicating that they were structurally intact, or "non-intact", indicating that there were large amounts of cell death causing the overall organoid structure to disintegrate. A subset of organoids both in devices and plate controls were characterized as non-intact and displayed large amounts of cell death. There was a slightly larger percentage of "intact" organoids in plate controls compared to devices (n.s., **Figure 4.17a**). For the intact organoids in devices and plate controls, cell death was assessed by CASP3 staining at days 21, 35, and 42. Small numbers of CASP3+ cells were observed in both device and plate control at all time points (**Figure 4.16**). Quantification of the percentage of CASP3+ cells in relation to the total number of cells (DAPI+) confirmed that all organoids had low levels of cell death (**Figure 4.17b**). Device organoids did have

increased proportions of CASP3+ cells compared to plate controls, but this difference was not statistically significant (**Figure 4.17b**).

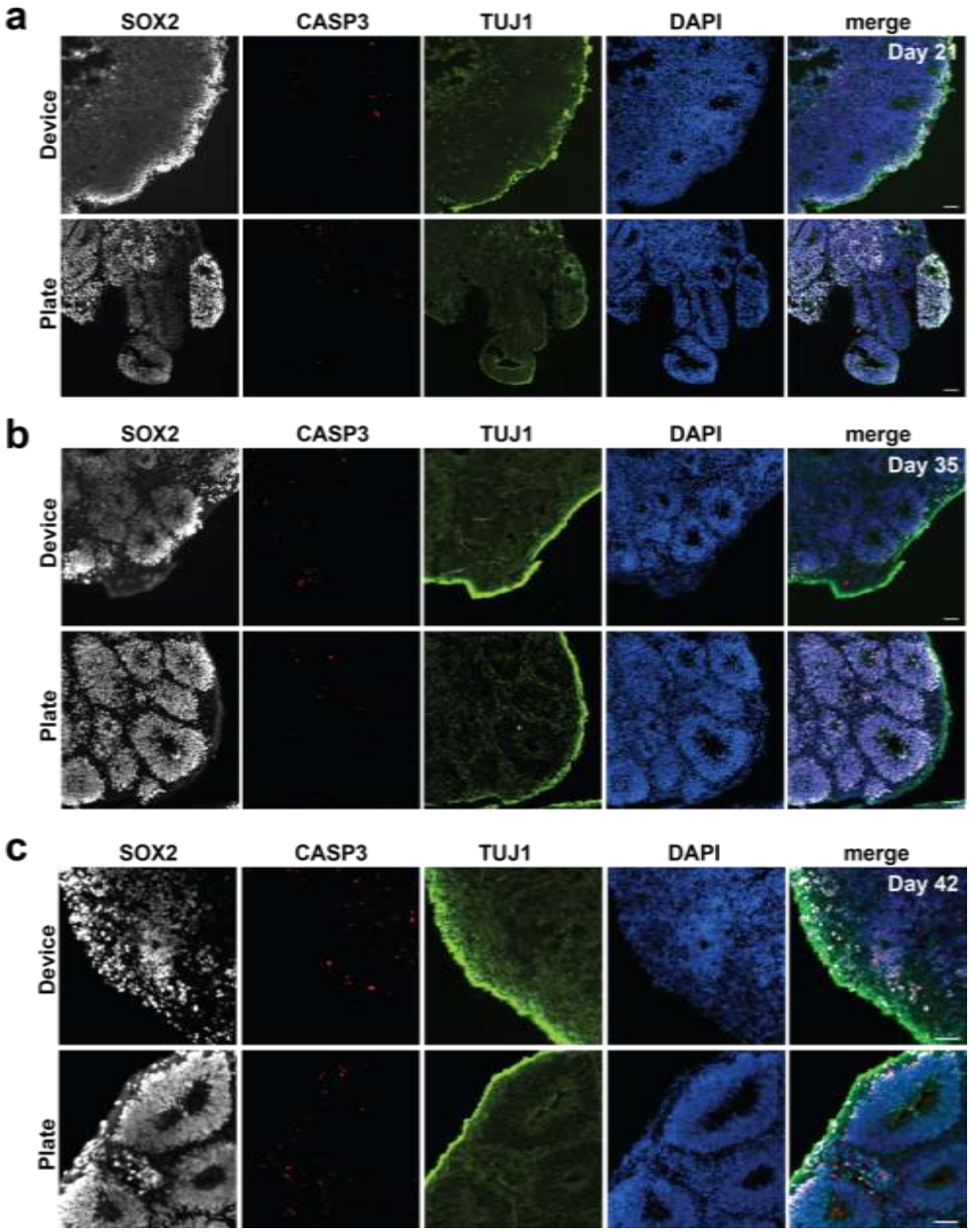

Figure 4.16. Characterization of cell death within forebrain organoids. Immunohistological analysis was performed for (a) day 21, (b) day 35, and (c) day 42 forebrain organoids cultured in devices or plate controls. Representative images show staining for NPCs (SOX2), the cell death marker caspase-3 (CASP3), a CP layer marker (TUJ1), and cell nuclei (DAPI). All scale bars are 100 μm. Images are representative of

20-40 organoids per time point. 3 independent experiments for day 21, 4 independent experiments for day 35, one experiment for day 42.

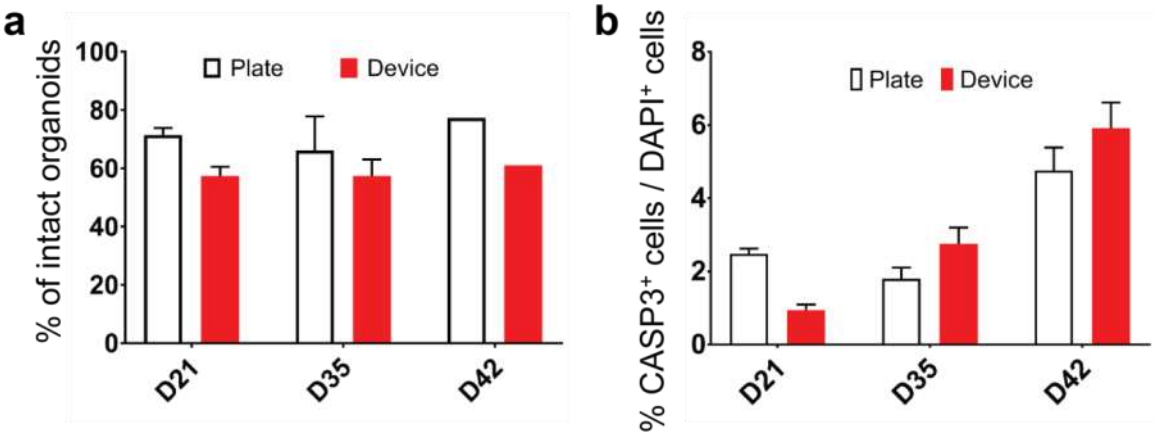

Figure 4.17. Quantification of cell death in organoids. a) The percentage of organoids with intact overall structure was manually quantified from bright field images for organoids cultured in devices and plate controls at days 21, 35, and 42. b) The percentage of dead cells (CASP3+) was quantified from immunohistology images for devices and plate controls at days 21, 35, and 42. Error bars indicate S.D. ANOVA was used; all groups: n.s. Data is representative of 20-40 organoids per time point. 3 independent experiments for day 21, 4 independent experiments for day 35, one experiment for day 42.

4.3.3.4 Discussion

Characterization of forebrain organoids cultured in the first generation microfluidic device revealed that organoids developed as expected in terms of generating stratified neural tube like structures with a VZ composed of SOX2+ NPCs and a CP layer with TBR1+/MAP2+ cells. At day 35, these structures were similar between organoids cultured in devices versus in a SpinΩ bioreactor. Interestingly, organoids cultured in devices were less heterogeneous and more differentiated than organoids observed in static plate cultures. Organoids cultured in plates had simpler, less differentiated neural tube structures, particularly at the day 21 time point. Previous work has shown that agitating the culture media can result in better organoid differentiation due to mixing-facilitated nutrient delivery[56], and this is a possible explanation for the less differentiated phenotypes observed in our static plate cultures. Together, the results suggest that the

microfluidic platform supports generation of forebrain organoids with cell types and structures comparable to what has been demonstrated in previous work.

We did observe that organoids cultured in devices tended to be smaller and had increased cell death. The specific cause of this is unclear, but it could be due to nutrient and/or oxygen limitations. In this first generation microfluidic design, media exchange is diffusion-dominated because the media perfusion channels are located above each culture chamber. Although this design enables the device to fabricated in a single layer, it results in less efficient media exchange in each culture chamber. The largest organoid diameter reached in device cultures was ~ 1.1 mm. Based on the transport modeling analysis described in **Section 4.3.2**, organoids of this size were likely not nutrient-limited for a nutrient such as glucose but may have experienced lower oxygen concentrations. To address any possible issues with nutrient/oxygen delivery, in the next portion of this chapter, we explored modifying the device design to enable better media exchange in the culture chambers.

4.3.4 Design of Second Generation, Flow-Through Microfluidic Device

Following design and testing of the first generation, diffusion-based device for forebrain organoid culture, a number of improvements were identified and implemented in a second generation device design (**Figure 4.18**). First, the media delivery channel configuration was re-designed to provide each culture chamber with a separate inlet and outlet (**Figure 4.18a**). This allows each culture chamber to be perfused with media in parallel—e.g. media does not flow serially from one chamber to the other, as with the first device design. Media is perfused from a single inlet in this design, and bifurcating channels deliver the media to each of the four columns of chambers. This configuration is

easily modified by reconfiguration the inlet and bifurcating channels so that each column of the device can be perfused with different media compositions. A key modification in this is design is the method by which media is exchanged in each culture chamber. As shown in the perspective view in **Figure 4.18b**, there is convective flow of media through each culture chamber through an inlet channel at the top of the chamber and an outlet channel at the bottom. This design better exchanges fluid in the culture chambers, compared to the previous, diffusion-dominated device design. A final change was to alter the culture chamber spacing so that it conforms to a 96-well plate footprint. This makes the platform compatible with other laboratory equipment, for example a multichannel pipette.

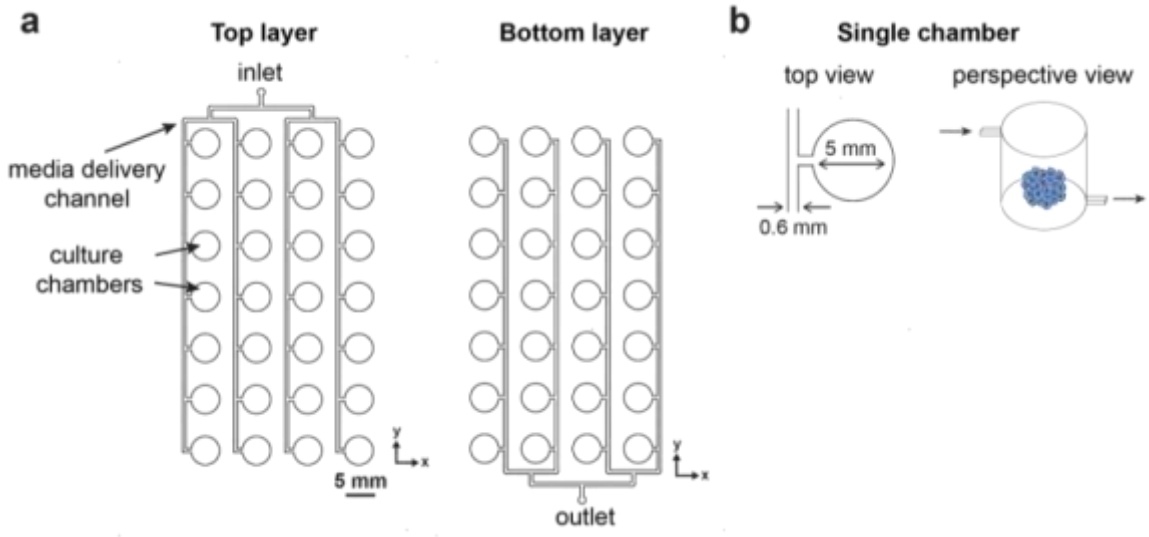

Figure 4.18. Design of the second generation, flow-through microfluidic device for organoid culture. a) Schematic illustrates the design of both device layers in a top-down view. b) Schematic depicts enlarged top view and perspective views of a single chamber with key dimensions noted.

The microfluidic platform is assembled similarly to the first generation design , as shown in **Figure 4.19**. The two device layers are fabricated from PDMS and bonded together with air plasma treatment prior to experiments. Organoids are manually loaded

into the device, and the device is then reversibly sealed to a glass slide using acrylic clamps and screws.

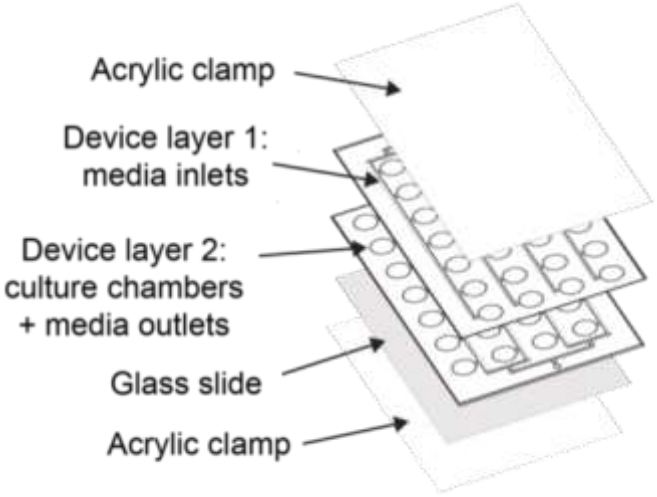

Figure 4.19. Assembly of the device. Schematic shows each of the device layers and order of assembly.

4.3.5 Transport Modeling in Second Generation Device Design to Inform Optimization of Operating Conditions

As with the first device design, we performed CFD modeling to assess how device operating conditions would impact delivery of nutrients and small molecules and removal of metabolites. We expected this through-flow chamber design to be more effective at exchanging media in each chamber because of the presence of convective flow. Transport modeling indicated that the previous device design adequately maintained concentrations of small molecules and removed metabolites such as lactate across a range of organoid sizes and operating conditions (Sections 4.3.2.4 and 4.3.2.5). Therefore, for the purpose of identifying appropriate operating conditions for this design, we focused on transport and consumption of glucose and oxygen.

As before, a 2D cross-section of an individual culture chamber was modeled with a single inlet and outlet, with the organoid represented as a circle centered in the chamber (**Figure 4.20**). All transport properties, concentrations, production/consumption rates, and cell densities used were the same as those used previously. Modeling results for the organoid culture device were again compared to those modeled for the SpinΩ.

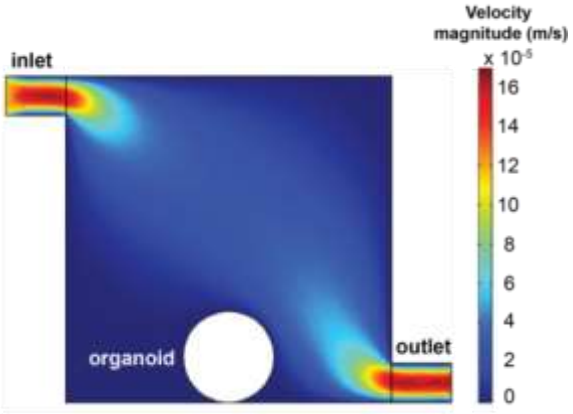

Figure 4.20. Depiction of how one chamber of the device was modeled. The geometry reflects a 2D side view of a single chamber with inlet and outlet channels. The organoid is modeled as a 2D circle centered at the bottom of the chamber. The heat map shows the velocity profile in the chamber for an inlet flow rate of 100 μL/hr.

We first assessed what media perfusion rate was needed to supply organoids with sufficient amounts of glucose. We modeled continuous media flow rates ranging from 50 - 400 μL hr^{-1} and organoid sizes from 0.6 mm to 2.6 mm in diameter. Although organoids typically only reached ~1.3 mm in diameter by day 35 in plate controls (**Figure 4.10a**), we wanted to assess if devices could also be used for longer culture times with larger organoids. As shown in **Figure 4.21**, for media perfusion rates of 200 μL hr^{-1} and higher, organoids up to 2.6 mm in diameter experienced glucose concentrations within 90% of the initial concentration. This reflected an improvement over the initial, diffusion-based device design, in which media perfusion at 200 μL hr^{-1} could maintain glucose concentrations within 90% of initial only for organoids of 2.0 mm in diameter and

smaller (**Figure 4.4a**). Overall, these results indicate that this device design delivers a nutrient such as glucose more efficiently and that glucose is not likely a limiting nutrient for organoids up to 2.6 mm.

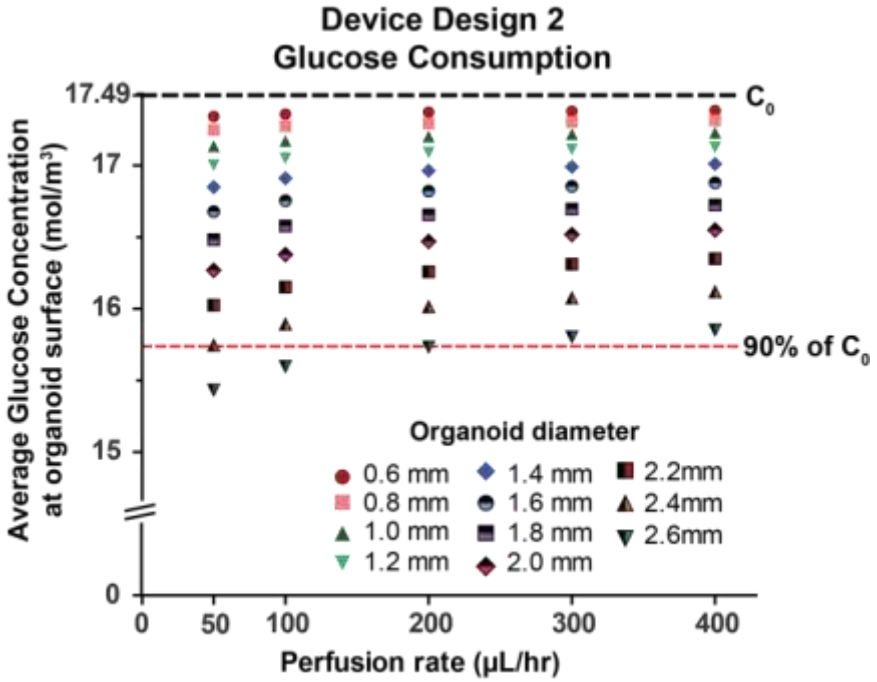

Figure 4.21. Glucose transport and consumption. a) Graph shows average glucose concentration at organoid surface for a range of organoid sizes and media perfusion rates.

We next modeled oxygen transport and consumption in the device. A similar geometry as before was specified for the model, with a column of seven chambers modeled and diffusion of oxygen through the PDMS taken into account (**Figure 4.22a**). Results from the center chamber are reported here to represent the "worst case scenario" of oxygen concentrations. **Figure 4.22b** shows the average oxygen concentration at the organoid surface in the center chamber for a range of organoid sizes and media perfusion rates. The modeling results show that oxygen concentrations fall below 90% of the initial concentration for all flow rates and organoid sizes modeled. Organoids approximately 1.4 mm in diameter and smaller experience hypoxic conditions (5% oxygen, equivalent to 0.065 mol m^{-3}) for perfusion rates of 200 µL hr^{-1} and higher. Increasing the flow rate has

minimal effect on increasing the oxygen concentration at steady state. Overall, these modeling results show improvement over the previous design, in which a maximum organoid size of 1.0 mm experience hypoxic oxygen concentrations or greater.

As discussed previously, oxygen consumption may be over-estimated in this 2D model because the organoid geometry is assumed to be an infinite cylinder. However, these results suggest that oxygen is potentially a limiting nutrient. Future work is needed to assess if potentially hypoxic conditions in devices have undesired effects on organoid growth and differentiation. In our studies, we did not implement additional design or experimental protocol changes to increase oxygen delivery, but this is a parameter that could be addressed in future work.

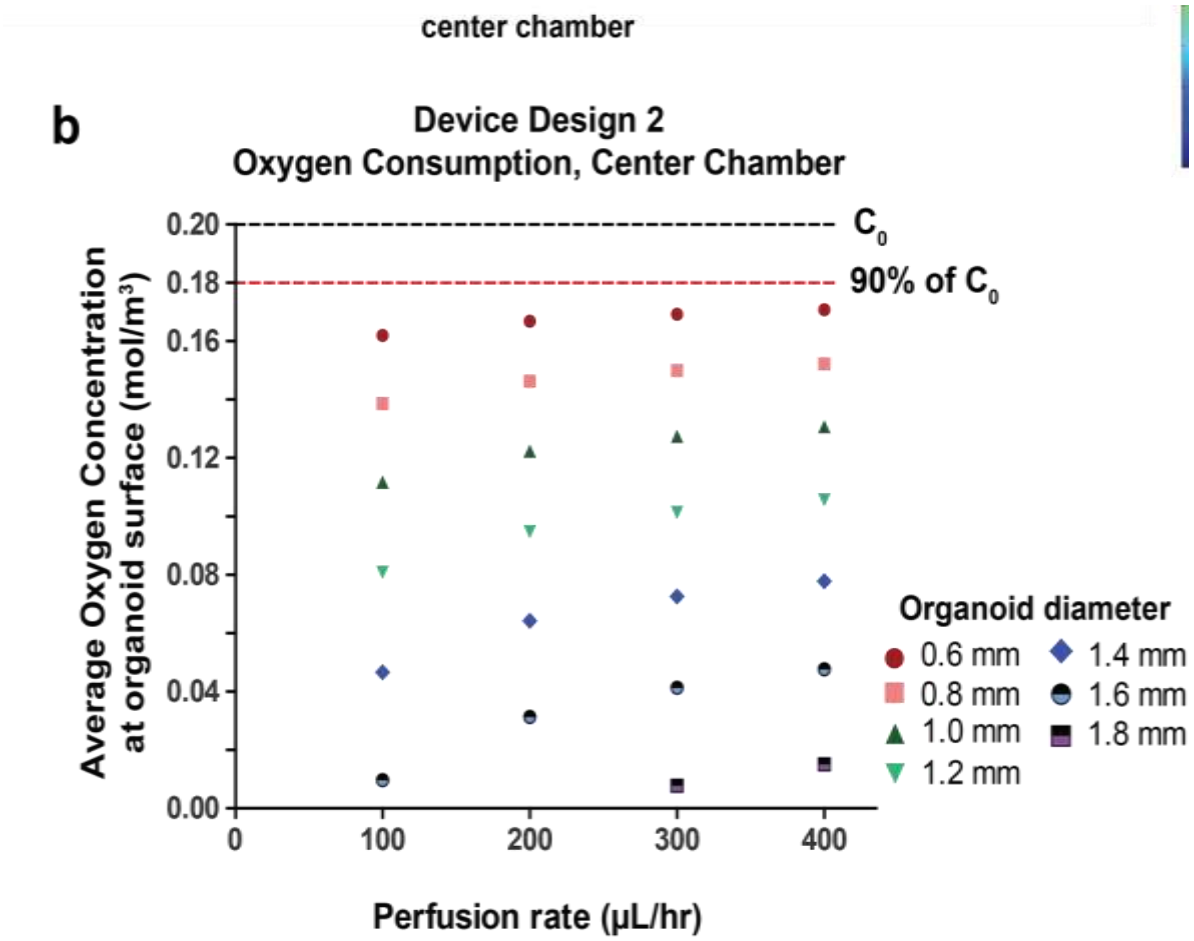

Figure 4.22. Modeling oxygen transport and consumption. a) Geometry used to model oxygen transport and consumption. Heat map shows the velocity profile for a flow rate of 100 µL/hr. b) Graph shows average oxygen concentration at organoid surface in the center of seven chambers in series for a range of organoid sizes and media perfusion rates.

4.3.6 Testing Organoid Culture in the Second Generation Device Design

4.3.6.1 Overview

In order to test the use of the second generation microfluidic device for forebrain organoid culture, day 14 organoids were cultured in devices up to day 35. It was expected that organoids would remain viable and develop normally, based on results obtained in the first device design. However, it was anticipated that there could be subtle differences in organoid growth and phenotypes as a result of the design changes affecting media perfusion. The results reported in this section are preliminary, in that they focus on

characterization of organoid growth and gross morphology only. Future work will be needed to assess cell types and structural features of organoids to confirm that they develop normally in the devices.

For testing of the devices, two different media exchange conditions were chosen. In the first condition, organoids were cultured with continuous perfusion at 200 μL hr^{-1}. This perfusion rate maintained glucose concentrations within 90% of the initial concentration for a large range of organoid sizes (up to 2.6 mm; **Figure 4.21**), and increasing the flow rate above this did not significantly increase steady state oxygen concentrations (**Figure 4.22b**).

The second condition chosen was culture of organoids under static media conditions with exchange of media once every 24 hours (24 hr^{-1}). A discontinuous media perfusion condition was chosen to help assess if continuous perfusion had any negative effects on organoid development. Continuous perfusion is known to down-regulate autocrine/paracrine signaling, as extensively discussed in Chapter 3 of this thesis. We hypothesized that this might be less of a concern for organoids than for smaller cell aggregates; the rationale was that the larger size and higher cell numbers of organoids could be better able to maintain cell-signaling environments within organoids. Nevertheless, we thought it prudent to include a static media control. The media exchange frequency of 24 hours was chosen based on a comparison to the volume of media per organoid and media exchange frequency used in SpinΩ culture. SpinΩ culture and the microfluidic device operate with the same volume of media per organoid: 2 mL for 20 organoids in the SpinΩ, and 0.1 mL for one organoid in the device. Media is

exchanged in the SpinΩ every 48 hours, so as a conservative estimate, we chose to exchange media in devices every 24 hours.

4.3.6.2 Organoid Size and Morphology

In order to evaluate organoid development, size and gross morphology were assessed from bright field images acquired at weekly time points. **Figure 4.23** shows representative images of organoids at days 14, 21, 28, and 35 for both microfluidic culture conditions (24 hr^{-1} and 200 μL hr^{-1}) and static plate controls. The same organoid is shown at each time point in devices, whereas different organoids are shown at each time point for plate controls. Overall, organoids appeared to grow normally in devices with expected size increases, maintenance of round morphologies, and expected morphological features visible. Neural epithelium/neural tube like structures were observed in organoids cultured in all three conditions, characterized by the round rosette- or bud-like morphologies features in the representative images (**Figure 4.23**). Some cell death was observed in both microfluidic culture conditions starting at day 21. This was characterized by dead cells separating from the main organoid structure. Interestingly, the majority of organoids with large amounts of dead cells present in the culture chamber still remained intact with morphological features characteristic of forebrain organoids present.

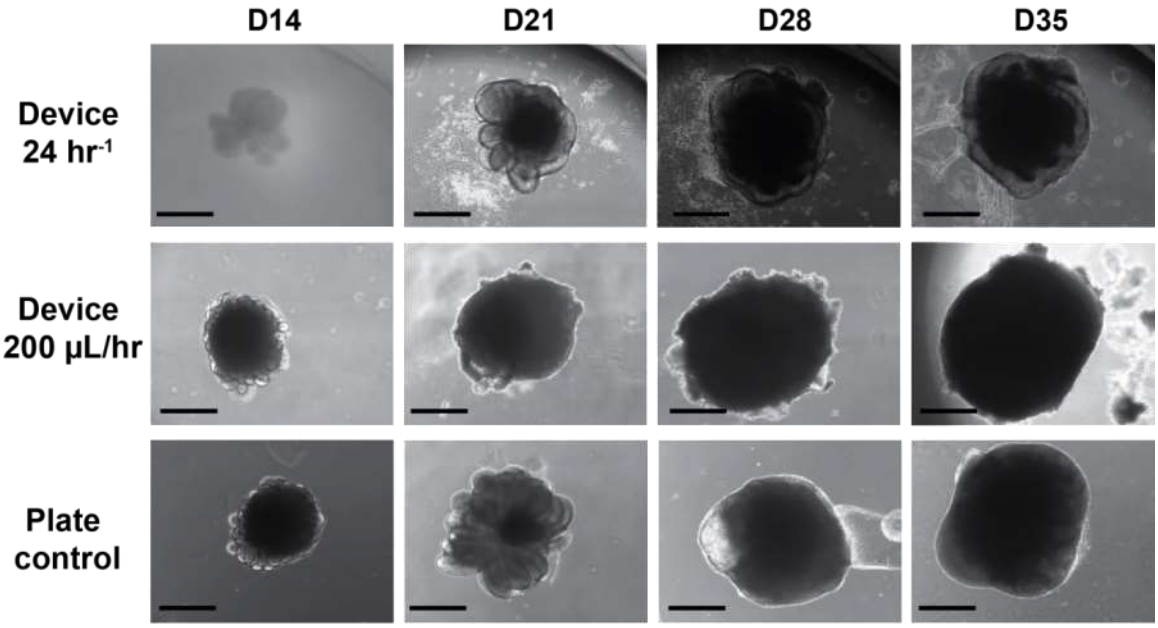

Figure 4.23. Representative bright field images of forebrain organoids. a) Images of representative forebrain organoids cultured in devices or static plate controls at days 14, 21, 28, and 35. Devices were operated with media exchange every 24 hours (24 hr^{-1}) or continuous perfusion at 200 µL hr^{-1}. All scale bars: 100 µm.

We quantified organoid size, circularity, and growth rate for both microfluidic device conditions and plate controls. As shown in **Figure 4.24a**, organoids increased in size over 35 days of culture. Organoids cultured at 200 µL hr^{-1} were slightly large in size than plate controls at all time points, but this difference was not statistically significant. In comparison, organoids cultured at 24 hr^{-1} were similar in size to the other conditions at days 14 and 21 but were significantly smaller than 200 µL hr^{-1} devices and plate controls at days 28 and 35. These results suggest that the 200 µL hr^{-1} device condition supports growth similar to plate controls. Slightly smaller organoid sizes for the 24 hr^{-1} device condition may suggest that this media exchange frequency is not sufficient. Organoid circularity was also assessed, as shown in **Figure 4.24b**. There were subtle differences in organoid circularity at days 14, 21, and 28, but these differences were not statistically significant by day 35. Growth rate was also assessed by quantifying the difference in size

between two time points and normalizing the by the size at the first of the two time points (**Figure 4.24c**). Organoids cultured at 200 μL hr^{-1} had a reduced growth rate compared to plate controls at days 14 and 21 but had a slightly higher growth rate at day 35. Organoids cultured at 24 hr^{-1} had similar growth rates to 200 μL hr^{-1} devices at days 21 and 25 but, interestingly had a lower growth rate at day 28. Together, this data suggests that of the two microfluidic culture conditions tested, continuous perfusion at 200 μL hr^{-1} may better support organoid growth. Exchanging media once per day may not sufficient for delivering nutrients. Additionally, there were subtle differences in organoid size and growth rate between microfluidic cultures at 200 μL hr^{-1} perfusion and plate controls.

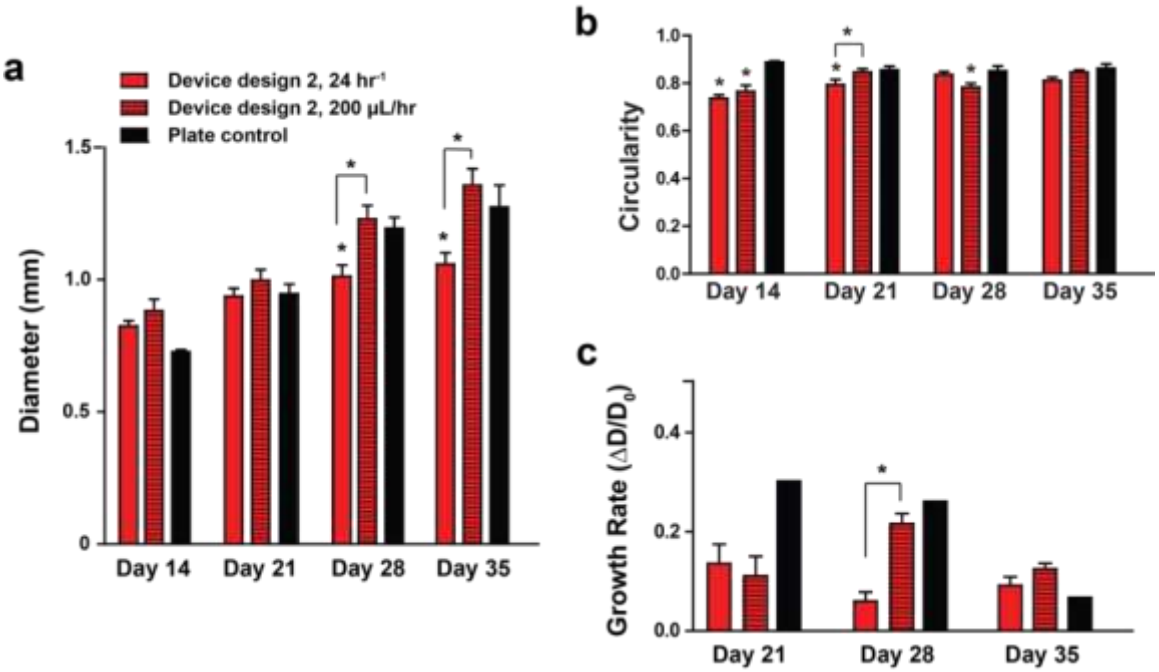

Figure 4.24. Organoid size, morphology, and growth rate. a) Organoid diameter measured at days 14, 21, 28, and 35 of culture. Diameter was calculated from the cross-sectional area of organoids in bright field images. Two-way ANOVA with Bonferroni posttests was used; * indicates $p < 0.01$. b) Organoid circularity at days 14, 21, 28, and 35 of culture was calculated from bright field images. Two-way ANOVA with Bonferroni posttests was used; * indicates $p < 0.01$. c) Growth rate was calculated, defined as the difference in size between two time points and normalized by the size at the first of the two time points. Two-way ANOVA with Bonferroni posttests was used for devices only, as plate control growth rate was calculated from population averages. * indicates $p < 0.01$. For all graphs, error bars indicate SEM.

4.3.6.3 Discussion

Assessments of organoid size and morphology over 35 days of culture in the second generation device design suggested that organoids develop normally in devices. Although some amounts of cell death were observed, organoids maintained intact structures and grew larger in this design by day 35 (average diameter ~ 1.4 mm) compared to the previous design (average diameter ~ 1.1 mm). Detailed characterization of organoid cell types and structures is still needed to fully validate this device design and culture conditions. However, the results described here provide preliminary evidence that this device design supports culture of forebrain organoids. Forebrain organoid features such as neural tube like structures were present in organoids culture both in devices and plate controls. In future work, immunohistological analysis can be used to evaluate the presence of a VZ layer containing SOX2+ NPCs and a CP layer containing TBR1+ and MAP2+ cells within these structures. Additionally, further analysis of cell death, for example with CASP-3 staining, will help assess how microfluidic culture conditions can be optimized to increase cell viability.

4.4 Conclusions

In this chapter, I designed and validated two versions of a microfluidic platform for culture and analysis of forebrain organoids. The microfluidic platform addresses current challenges associated with multiplexing and scaling of current organoid culture systems. It also provides the ability to observe and assess organoids throughout culture, enabling the collection of information that can be used to better understand parameters governing forebrain organoid development and assessing different organoid features during screening. In conjunction with development of the microfluidic platform, a

quantitative transport modeling analysis was used to assess how microfluidic culture conditions impact delivery and removal of key nutrients, media additives, and metabolites. This analysis provides a framework for understanding how to optimize device geometries and media exchange conditions.

Forebrain organoid development was validated in the first generation, diffusion-based microfluidic platform through morphological and immunohistological assessments. Importantly, the results of these analyses demonstrated that forebrain organoids developed as expected, with cell types and structures comparable to those obtained in a SpinΩ bioreactor for culture times up to 42 days. Interestingly, organoids cultured in microfluidic devices were more differentiated with better defined VZ and CP layers than organoids cultured in static media in tissue culture plates. This suggests that microfluidic perfusion culture can replicate effects of a miniaturized spinning bioreactor in supporting forebrain organoid differentiation.

Following validation of forebrain organoid culture in the initial device, we implemented design improvements in a second generation, flow-through microfluidic device design. This design is based on a 96 well plate footprint and can easily be modified and scaled up to screen multiple conditions in a single device. We validated forebrain organoid culture in this version of the design by characterizing organoid size and morphology. Organoids grew slightly larger in this design than previously, likely due to improved delivery of nutrients and removal of waste with the new channel design. While full characterization is still needed of forebrain organoid cell types and structures generated in this device, this work provides a preliminary validation of this microfluidic design.

Overall, the work performed in this chapter establishes a novel microfluidic platform for culture of forebrain organoids. This platform technology will serve as a valuable tool for understanding how to more robustly generate forebrain organoids, studying developmental disorders, and performing drug screening. Additionally, this technology can be applied to other organoid types. Further opportunities for development and application of this technology will be discussed in Chapter 5 of this thesis.

CHAPTER 5 : CONCLUSIONS AND FUTURE WORK

5.1 Thesis Contributions

The overall objective of this thesis was to develop microfluidics-based technologies for culture and assessments of PSC aggregates. The work presented here addresses technological gaps associated with current conventional and microfluidic culture systems: namely, the lack of ability to culture and assess individual aggregates without sacrificing throughput, experimental ease, or imaging capabilities. The microfluidics-based technologies developed in this thesis enable collection of single-aggregate and single-cell level phenotypic information. The ability to observe individual samples at multiple time points is highly informative for studying stem cell differentiation and tissue morphogenesis, particularly with the use of reporter cell lines. This work incorporated interdisciplinary knowledge and techniques. Microfabrication methods, computational fluid modeling, and qualitative transport modeling analyses were used to design the microfluidic platforms and optimize operating conditions. To collect and quantify cellular phenotypic information, techniques including immunocytochemistry, microscopy, and image processing were used.

The microfluidic platforms described in this thesis allow for culture of stem cell aggregates at two size scales: ~200 - 500 μm diameter (Chapters 2 and 3) and ~0.6 - 5 mm diameter (Chapter 4). Both sets of platforms enable culture of individual aggregates and imaging-based assessments during culture. Although these technologies were developed and validated specifically for mESC aggregates and iPSC-derived forebrain organoids, they can readily be applied and adapted for culture of other types of cell

aggregates. Examples include tumor spheroids, other stem cell aggregates types, and other organoid types.

In Chapters 3 and 4, computational and qualitative transport modeling were used to optimize microfluidic media exchange conditions. The microscale culture environment varies from that of macroscale culture in many critical aspects, such as the density of cells per media volume and the relative roles played by convective and diffusive mass transport. Thus, modeling-based approaches were important in understanding how to design microfluidic culture conditions to support cell growth and differentiation. The work in Chapter 3 explored how to design media exchange strategies to balance requirements for nutrient delivery with the need to maintain concentrations of cell-secreted factors. This was shown in the context of motor neuron differentiation of mESC aggregates. Results indicated that discontinuous media perfusion better supported differentiation by allowing accumulation of cell-secreted factors required for cellular processes associated with growth and differentiation. In Chapter 4, in the context of forebrain organoid culture, transport modeling enabled identification of ranges of operating conditions that would support organoid growth and survival. Selected conditions were then validated experimentally by characterization of organoid growth, morphology, cell types, and structures at up to 8 weeks of culture.

Throughout this thesis, microfluidic techniques were leveraged to control and perturb cell and aggregate phenotypes. The work in Chapter 3 demonstrated that microfluidic culture could be used to perturb the cell microenvironment in ways that conventional batch culture methods could not. Specifically, this work showed how asymmetrical microfluidic device geometries could be used to created local gradients of

soluble factors and influence spatial patterns of pMN differentiation. This effect was dependent on media perfusion frequency. This finding has implications for applications in spatial patterning of tissues and understanding how symmetry-breaking events occur during embryonic development. In Chapter 4, long-term microfluidic culture was shown to produce forebrain organoids comparable to those generated with state-of-the-art methods, in terms of morphology, cell types, and structural features. Interestingly, forebrain organoids cultured in microfluidic devices were more differentiated with better defined VZ and CP layers than organoids cultured in static media in plates, but were comparable to organoids cultured in the SpinΩ bioreactor. This suggests that microfluidic perfusion culture can replicate effects of a miniaturized spinning bioreactor in supporting better organoid differentiation.

Overall, the technologies developed in this thesis provide new capabilities for culture, manipulation, and assessment of PSC-derived tissues ranging in size from small aggregates to large organoid tissues. I envision that these tools can be broadly applied by our lab and others for studying mechanisms of stem cell differentiation and tissue morphogenesis. Specifically for PSC-derived organoids, the tools we have developed will enable studies in learning how to more robustly generate forebrain organoids, studying developmental disorders, and performing drug screening.

5.2 Future Directions

The microfluidic platforms developed in this thesis facilitate culture and assessment of different types of 3D stem cell derived tissues. In this section, I discuss opportunities for further development and applications of these technologies.

5.2.1 Investigating Roles of Autocrine and Paracrine Signaling in 3D Stem Cell Differentiation

Autocrine and paracrine signaling play important roles in stem cell self-renewal[119,120], growth[121,122], and differentiation[123]. While the roles of cell-secreted signaling are difficult to probe using conventional culture methods, a number of microfluidic techniques have been developed for this purpose[98,99,126]. However, these studies have focused on 2D cell cultures and not 3D cell aggregate cultures. The microfluidic platform developed in Chapters 2 and 3 can be used to modulate cell-secreted signaling in 3D aggregate cultures by changing media exchange rate and frequency. This could be applied in studying how autocrine/paracrine signaling regulate specific differentiation events, in a similar approach used by Blagovic et al.[98] For example, Notch-Delta and TGFβ signaling play roles in cell fate decisions during motor neuron differentiation[127,142], but some aspects of this regulation are still not completely understood. Operating devices under continuous perfusion could be used to observe effects of down-regulating endogenous signaling (ensuring aggregates are small enough not to block media exchange through traps). Then, conditioned media and supplementation experiments could be used to identify key signaling molecules and their roles in cell fate decisions. Overall, experiments such as this could be performed to reveal novel mechanisms that regulate stem cell behavior and differentiation.

5.2.2 Generation of Asymmetrically Patterned Stem Cell Tissues

The platform developed in Chapters 2 and 3 can also be applied in generating stem cell tissues with asymmetric patterns of differentiation. In Chapter 3, it was demonstrated that, while operating under diffusion-dominated conditions, device features could be exploited to induce asymmetric differentiation in aggregates. This has a range of

applications, including in understanding how symmetry-breaking events occur during embryonic development. Examples of approaches currently used to induce spatial patterning in stem cell colonies or aggregates include geometrical confinement[143], mechanical stimulation[144], or merging multiple pre-patterned cell aggregates[63,88,145]. More recently, work has demonstrated that symmetry-breaking events can be generated endogenously through self-organization processes in EBs[146], organoids[48], and gastruloid tissues[147]. The technology developed in Chapter 3 offers a complementary approach to inducing spatial patterning: the platform can potentially be used to create gradients of exogenously delivered molecules or endogenously produced cell signaling molecules, depending on if the microfluidic device is operated in a convection- or diffusion-dominated regime. Overall, this approach can be used to investigate spatial patterning of tissues and the roles that different mechanisms play in symmetry breaking during tissue morphogenesis.

5.2.3 Improvements to Brain Organoid Culture Platform

A number of further characterizations and improvements can be made to the platform developed in Chapter 4 for culture and assessments of brain organoids. First, further characterization of organoid culture in the second generation, flow-through device design is still needed. This design incorporated convective media flow through each culture chamber to improve delivery of nutrients and removal of waste. Based on characterization of organoid gross morphology, size, and growth rate, it is expected that the device supports forebrain organoid generation. However, full immunohistological characterization is still needed of organoid cell types and structures. This characterization can also be used to optimize the media exchange rate used.

Modifications to the way that the organoid platforms are assembled will better enable *in situ* high resolution imaging during culture. Currently, the PDMS devices are sealed against a glass slide and clamped with pieces of acrylic. While this allows for low magnification and relatively low-resolution imaging, the ultimate goal is to perform confocal imaging in the platform. Confocal imaging can be used to perform functional calcium imaging of neural activity in organoids as well as to assess cell phenotypes in conjunction with tissue clearing and immunocytochemistry. One way to enable confocal imaging is to reversibly seal the PDMS devices to coverslip-thickness glass using biocompatible adhesive tape. Glass coverslips likely cannot be clamped to the PDMS device, as they are more prone to breakage, so adhesive tapes are a possible alternative for sealing. If adhesive sealing of glass coverslips is too prone to breakage as well, then alternative materials such as cyclic olefin copolymer (COC) films can potentially be used as an imaging surface. COC films are optically transparent, particularly in the ultraviolet range, and are increasingly used as imaging surfaces in cell biology and microfluidics[148-150].

5.2.4 Drug Screening with Forebrain Organoids

There is much interest in using forebrain organoids to screen potential therapeutics for developmental disorders and diseases[54,61]. The platform developed in Chapter 4 can be used to address limitations of current organoid culture methods in screening. The design of the device is based on a 96 well plate footprint, making it easier to incorporate with existing workflows and laboratory equipment. The design can also be configured to screen different numbers of independent conditions, with replicates for each, on the same device. It is envisioned that this platform can be applied in screening

libraries of drug candidates for effects on organoid disease phenotypes, using organoid structures and cell types as metrics for assessment. For screening assays in the short term, organoid phenotypes can be assessed by end point based assays such as tissue clearing with immunocytochemistry. However, in the longer term, it would be valuable to develop methods for assessing phenotypes in live organoids—for example, using organoid morphological features from bright field images. Ultimately, the organoid culture platform can serve as a novel tool for identifying and screening new therapeutics for neurodevelopmental disorders and diseases.

APPENDIX A: CHAPTER 3 SUPPLEMENTARY MATERIAL

These figures are adapted from a research article entitled "A microfluidic trap array for longitudinal and multi-modal phenotypic analysis of individual stem cell aggregates" published in Lab on a Chip in 2017[2].

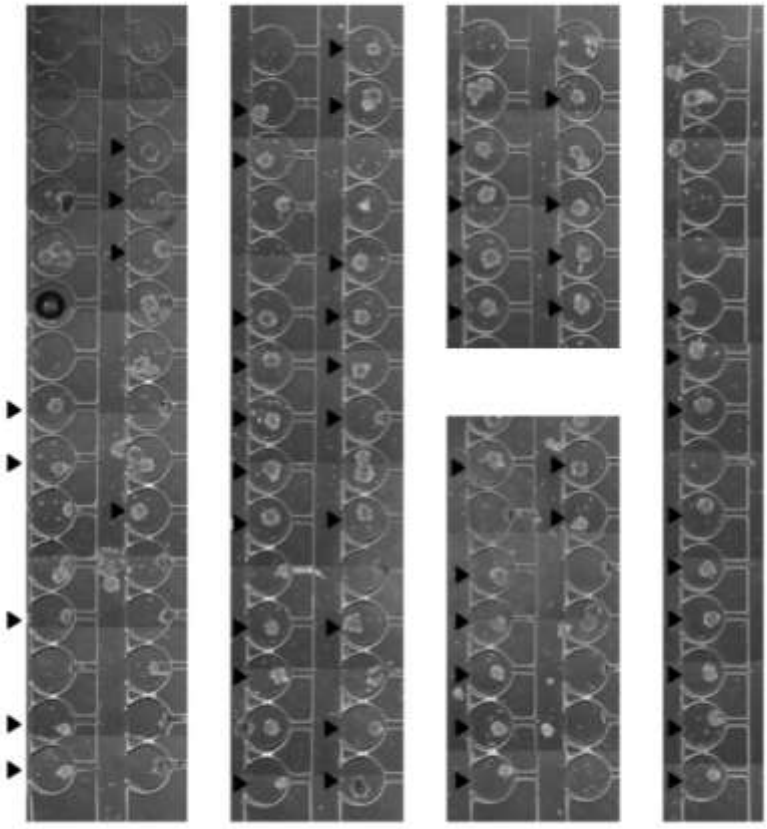

Appendix A.1. Stitched representative image of a device loaded with 1000 cell aggregates. Black arrows indicate singly loaded traps.

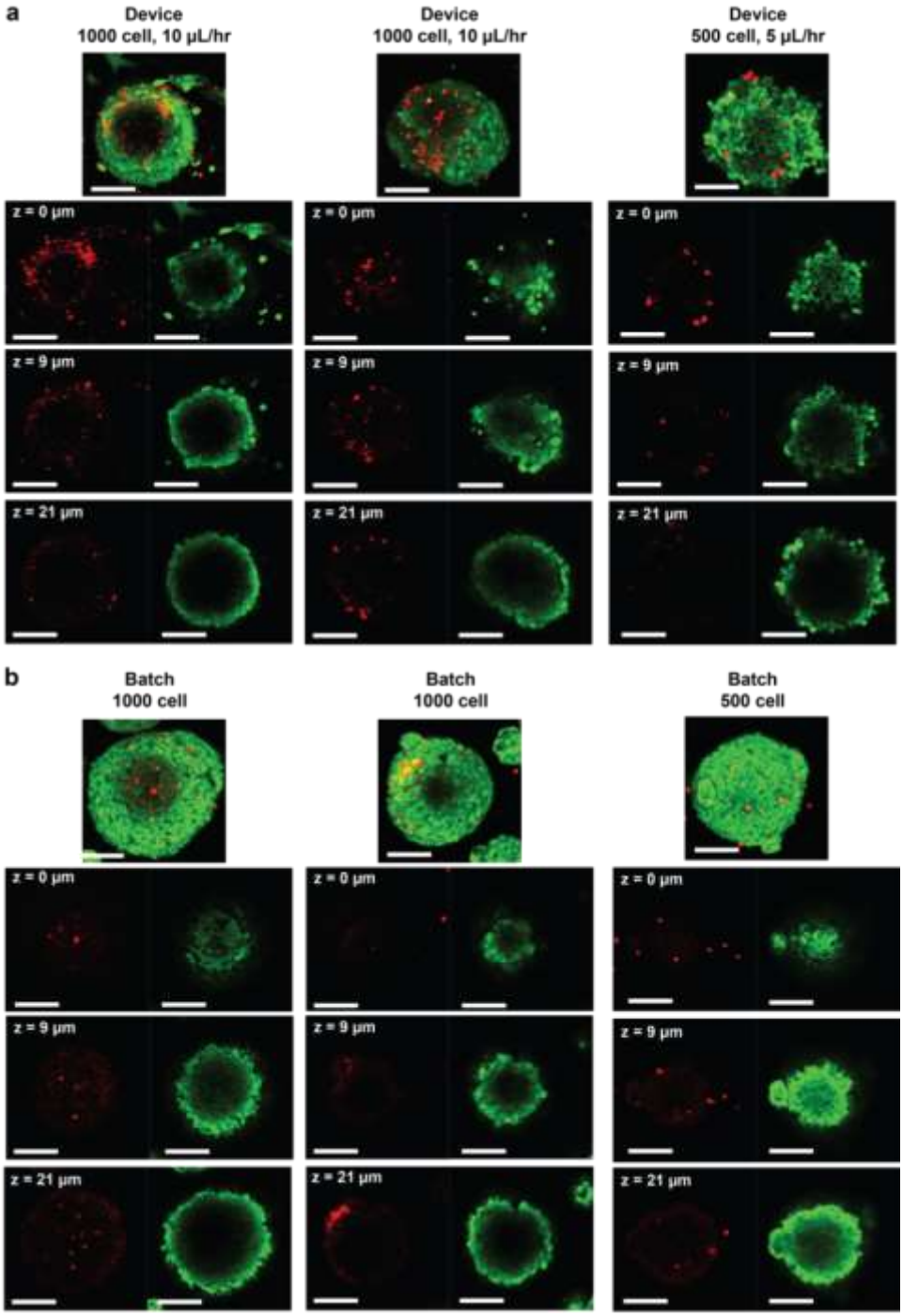

Appendix A.2. Additional viability data. Representative confocal images of day 4 aggregates treated with a LIVE/DEAD stain (live cells: green; dead cells: red). For each condition, the top image is a maximum intensity projection of all z slices imaged for a given aggregate. Underneath, three z slices are shown. a) Images for both 1000 cell starting size aggregates cultured at 10 µL/hr and for 500 cell starting size aggregates cultured at 5 µL/hr. b) Images for 100 cell starting size and 500 cell starting size aggregates cultured in batch. All scale bars: 100 µm.

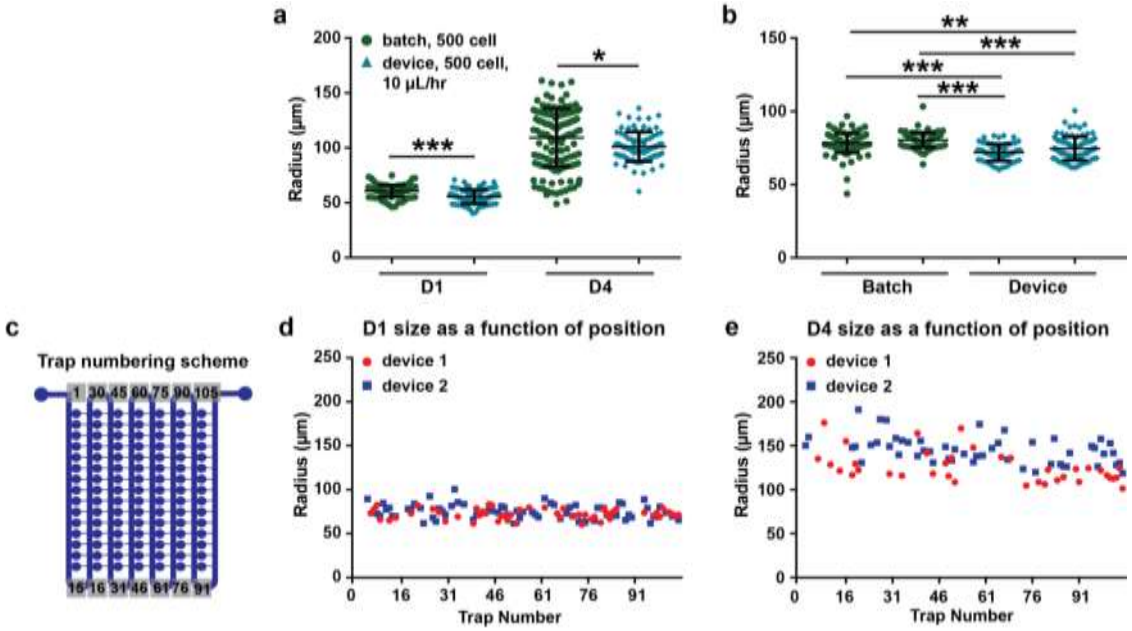

Appendix A.3. a) Device culture reduces variability in size for 500 cell starting size aggregates. Aggregate radii were quantified from phase contrast images at day 1 and day 4 of differentiation for 500 cell aggregates cultured under 10 µL/hr media perfusion). Two independent samples are shown for each condition, with $n \geq 100$ for batch samples and $n \geq 85$ for device samples. * $P < 0.01$; *** $P < 0.0001$. b) Size distributions of aggregates captured in devices are similar to batch aggregates. Two replicates per condition are shown for 1000 cell aggregates (device culture: 10 µL/hr media perfusion). ** $P < 0.001$; *** $P < 0.0001$ c) Schematic of trap numbering convention used in c and d. c,d) Aggregate radii is plotted as a function of position within the device, for 1000 cell aggregates cultured under 10 µL/hr perfusion. Two devices are shown for days 1 and 4 of differentiation.

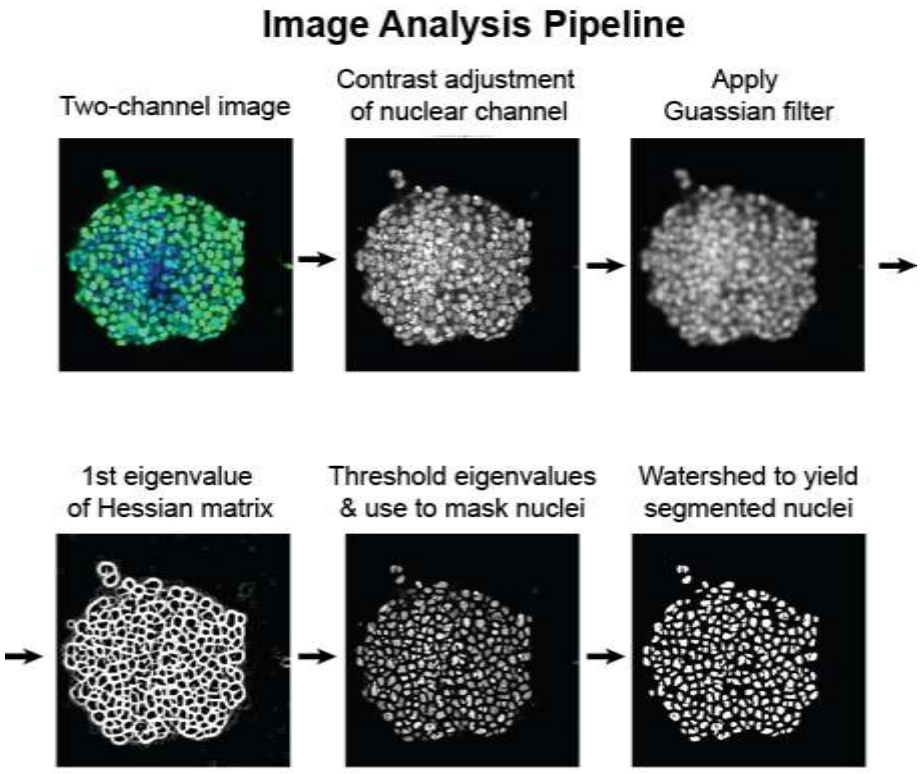

Appendix A.4. Image processing pipeline used to analyze fluorescent images modified from Lou, et al.[110]

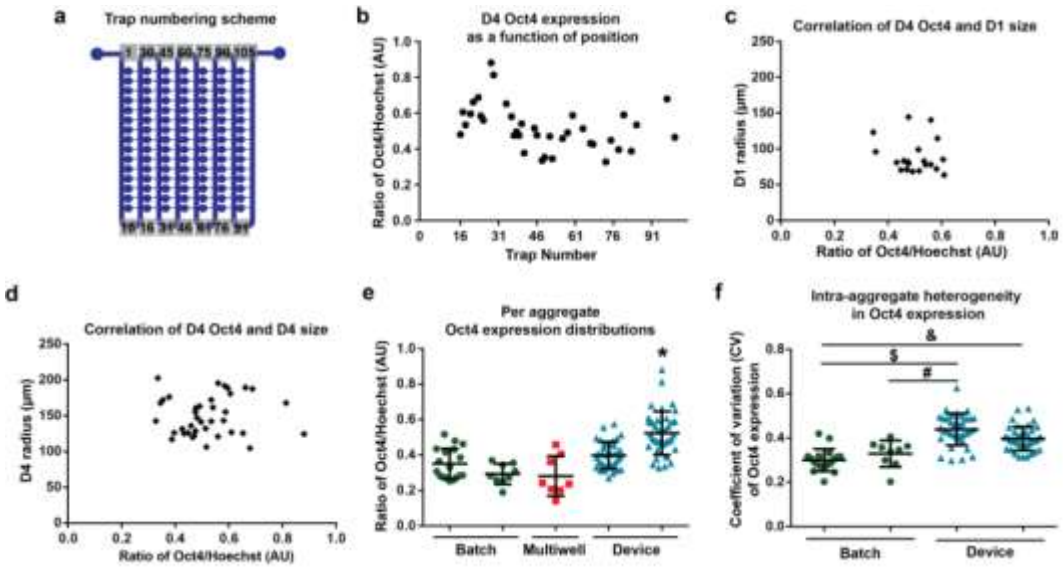

Appendix A.5. a) Schematic of trap numbering convention used in b. b) Mean aggregate Oct4 expression is plotted as a function of position within the device. One device is shown. Performing linear regression on this data produced a line of slope -0.002 and an R^2 value of 0.141, indicating no trend between Oct4 expression and position. c,d) Mean aggregate Oct4 expression is plotted as a function of aggregate radius at day 1 (c) and day 4 (d). e) Scatter plot shows mean Oct4 expression for individual aggregates cultured within batch, multiwell, or device platforms (raw data corresponding to Figure 5b). Two independent experiments are shown for batch and device conditions ($n \geq 25$ each) and one experiment is shown for multiwell condition ($n = 8$). * $P < 0.00001$ vs. both batch and multiwell samples, $P < 0.0001$ vs. other device sample. f) Intra-aggregate heterogeneity in Oct4 expression for device and batch platforms. Two independent experiments are shown for batch and device conditions ($n \geq 25$ each). # $P < 0.001$, $ $P < 0.00001$, & $P < 0.0001$.

APPENDIX B: CHAPTER 4 SUPPLEMENTARY MATERIAL

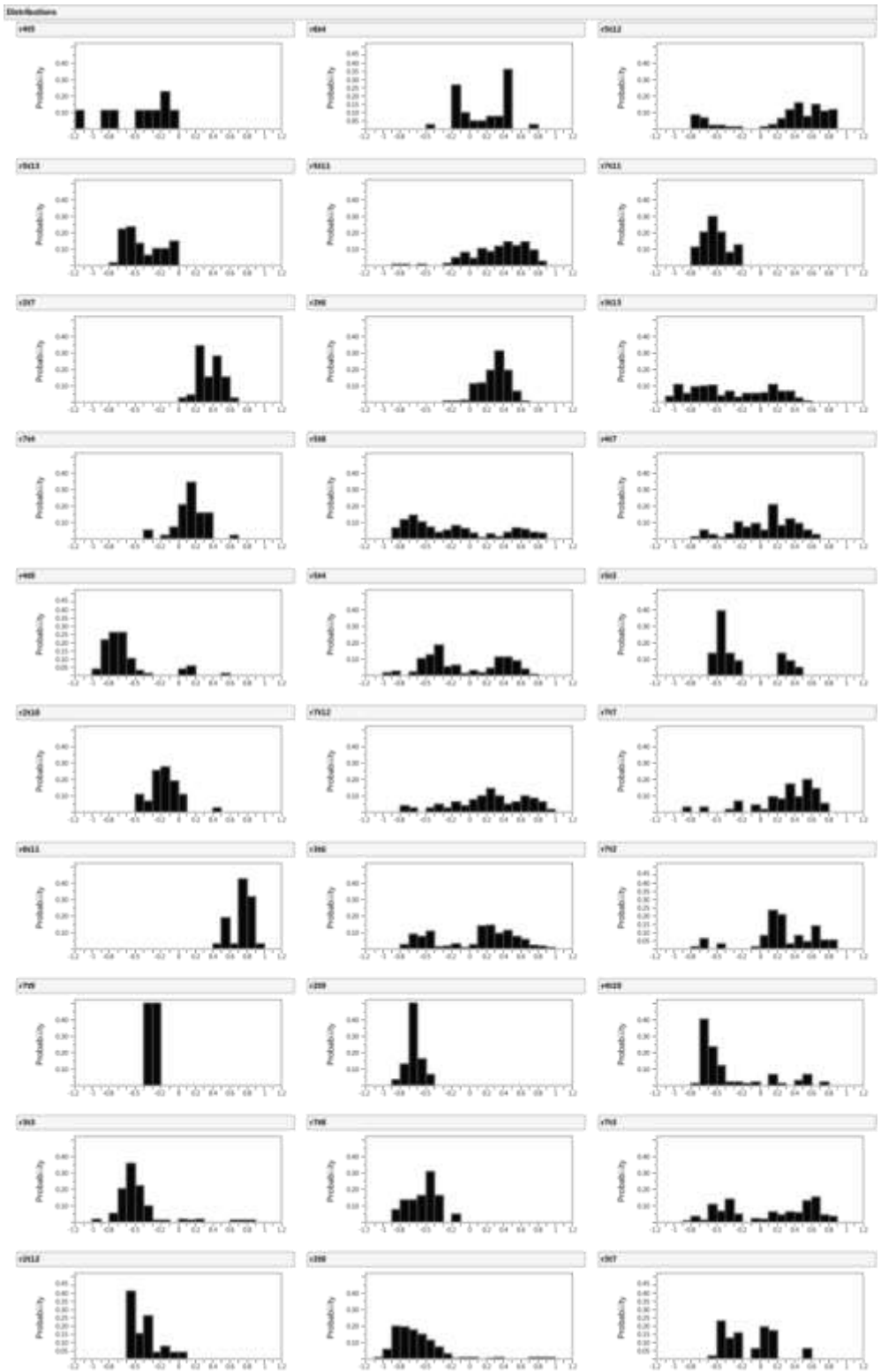

Appendix B.1. Histograms show horizontal position of Olig2+ cells with respect to aggregate center line for discontinuous perfusion (f = 1 d-1) with 2 μM RA and 1.5 μM Pur. Zero indicates aggregate center line, positive numbers indicate portion of aggregate closer to trap entrance, and negative numbers indicate portion of aggregate closer to back of trap.

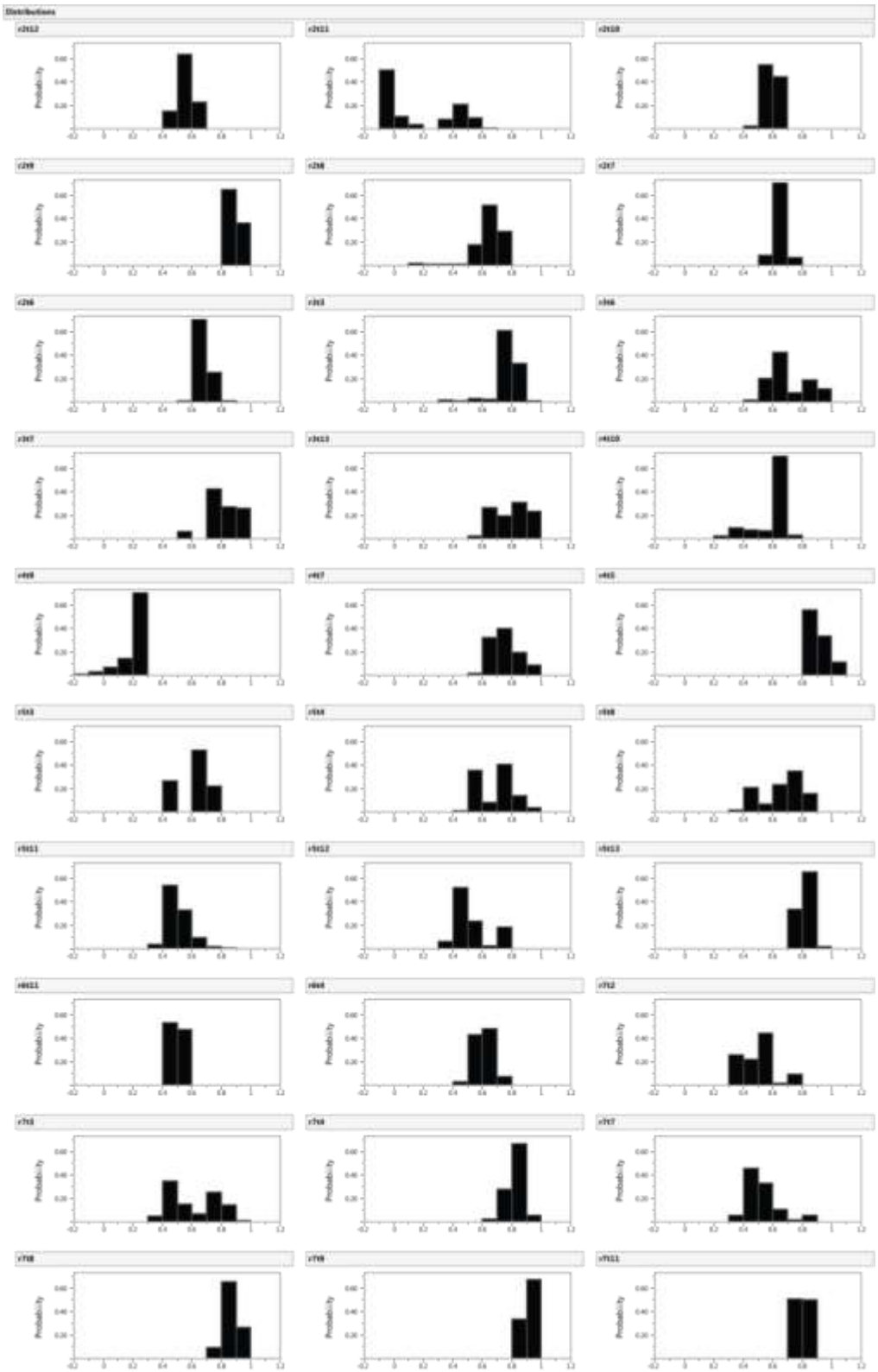

Appendix B.2. Histograms show horizontal position of Olig2+ cells with respect to trap coordinates for discontinuous perfusion (f = 1 d^{-1}) with 2 μM RA and 1.5 μM Pur. Zero indicates trap entrance and 1 indicates back of trap, where circular trap meets restriction channel.

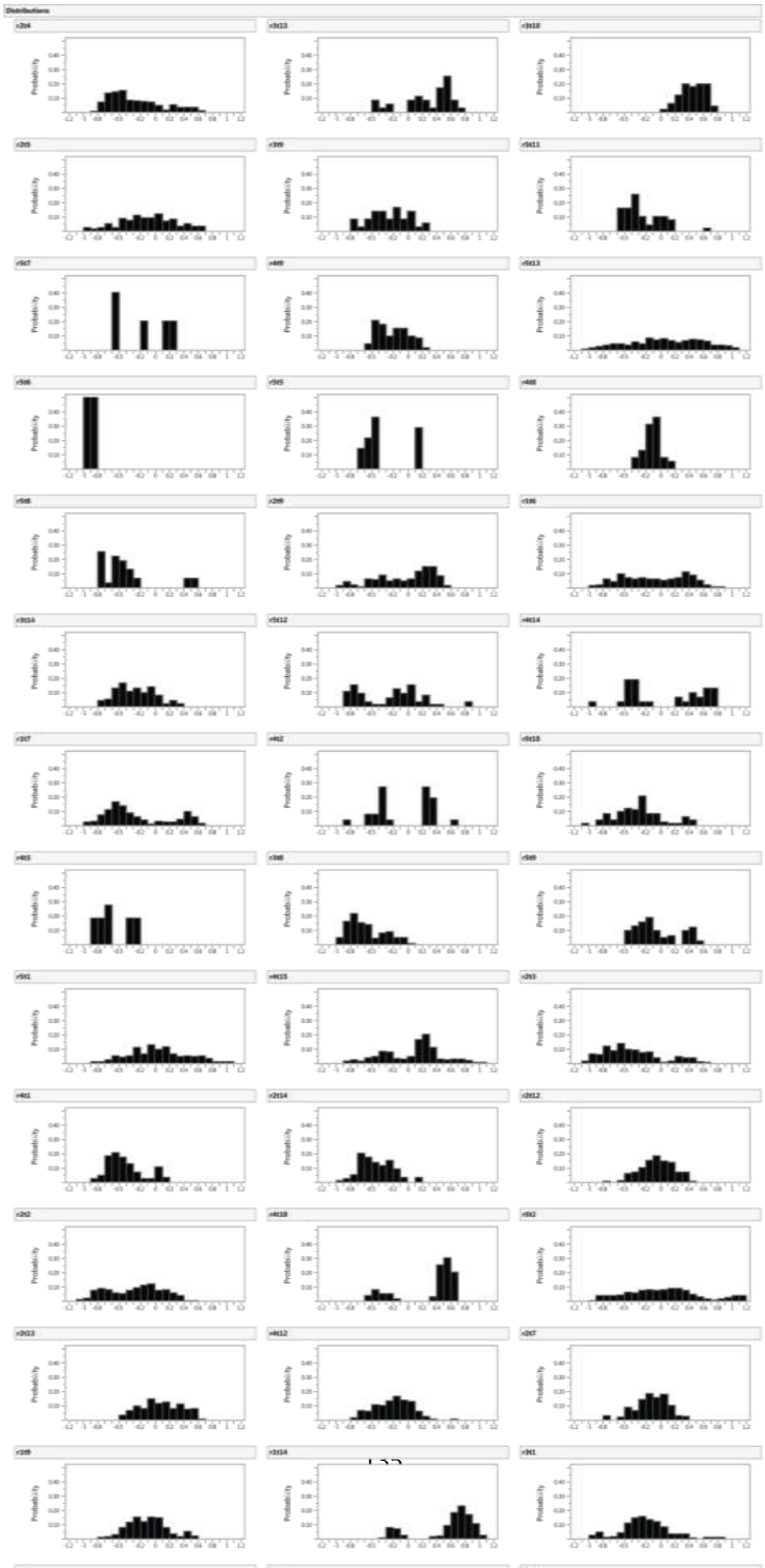
Distributions
r2t4
r3t13
r3t18
r2t5
r3t9
r5t11
r5t7
r4t9
r5t13
r5t6
r5t5
r4t8
r5t8
r2t9
r3t6
r3t14
r5t12
r4t14
r2t7
r4t2
r5t18
r4t3
r3t8
r5t9
r5t1
r4t15
r2t3
r4t1
r2t14
r2t12
r2t2
r4t18
r5t2
r2t13
r4t12
r2t7
r2t9
r3t14
r3t1
r3t7
r3t2
r2t1

Appendix B.3. Histograms show horizontal position of Olig2+ cells with respect to aggregate center line for discontinuous perfusion ($f = 3\ d^{-1}$) with 6 μM RA and 3 μM Pur, one device. Zero indicates aggregate center line, positive numbers indicate portion of aggregate closer to trap entrance, and negative numbers indicate portion of aggregate closer to back of trap.

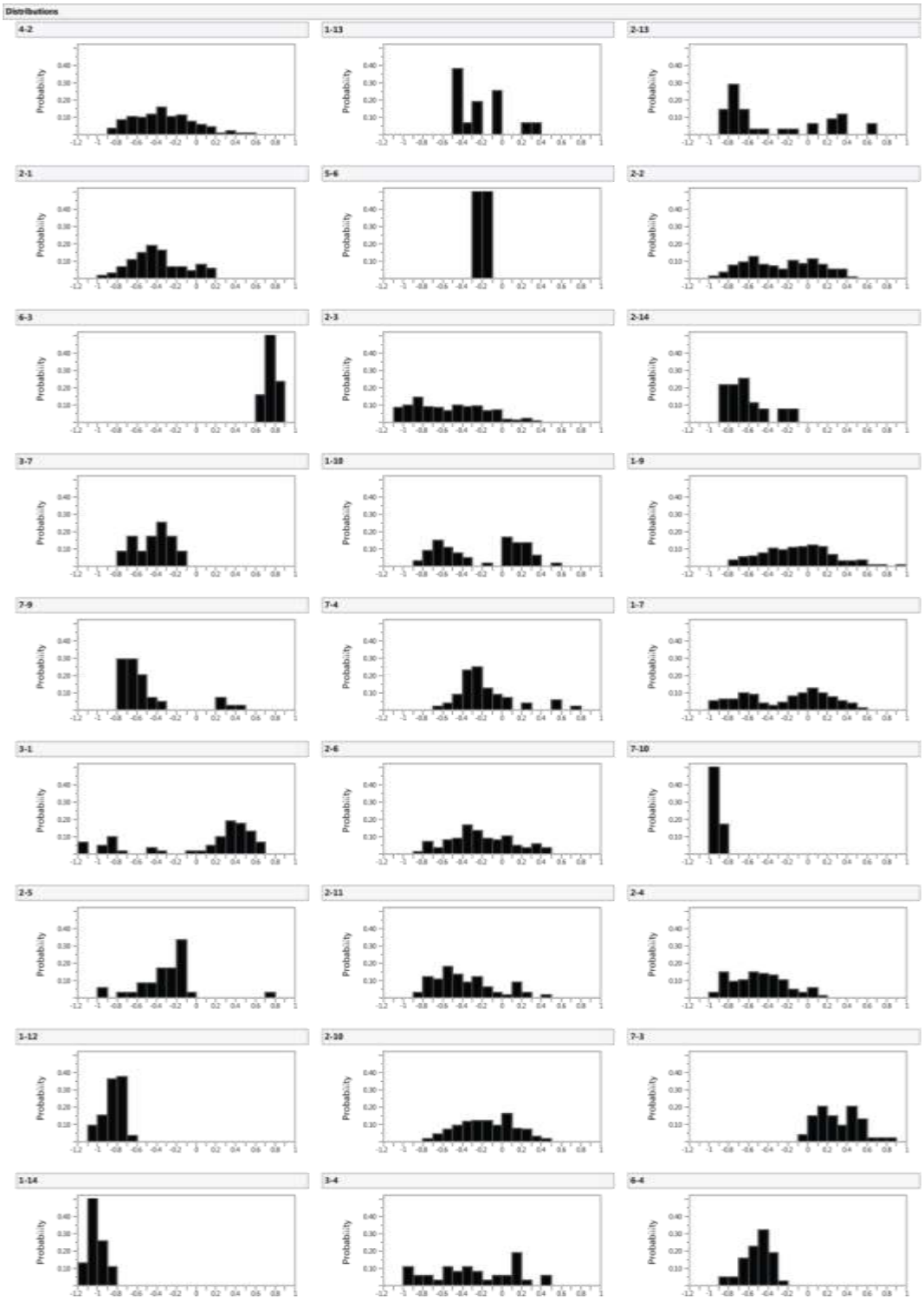

Appendix B.4. Histograms show horizontal position of Olig2+ cells with respect to aggregate center line for discontinuous perfusion ($f = 3\ d^{-1}$) with 6 μM RA and 3 μM Pur, a second device. Zero indicates aggregate center line, positive numbers indicate portion of aggregate closer to trap entrance, and negative numbers indicate portion of aggregate closer to back of trap.

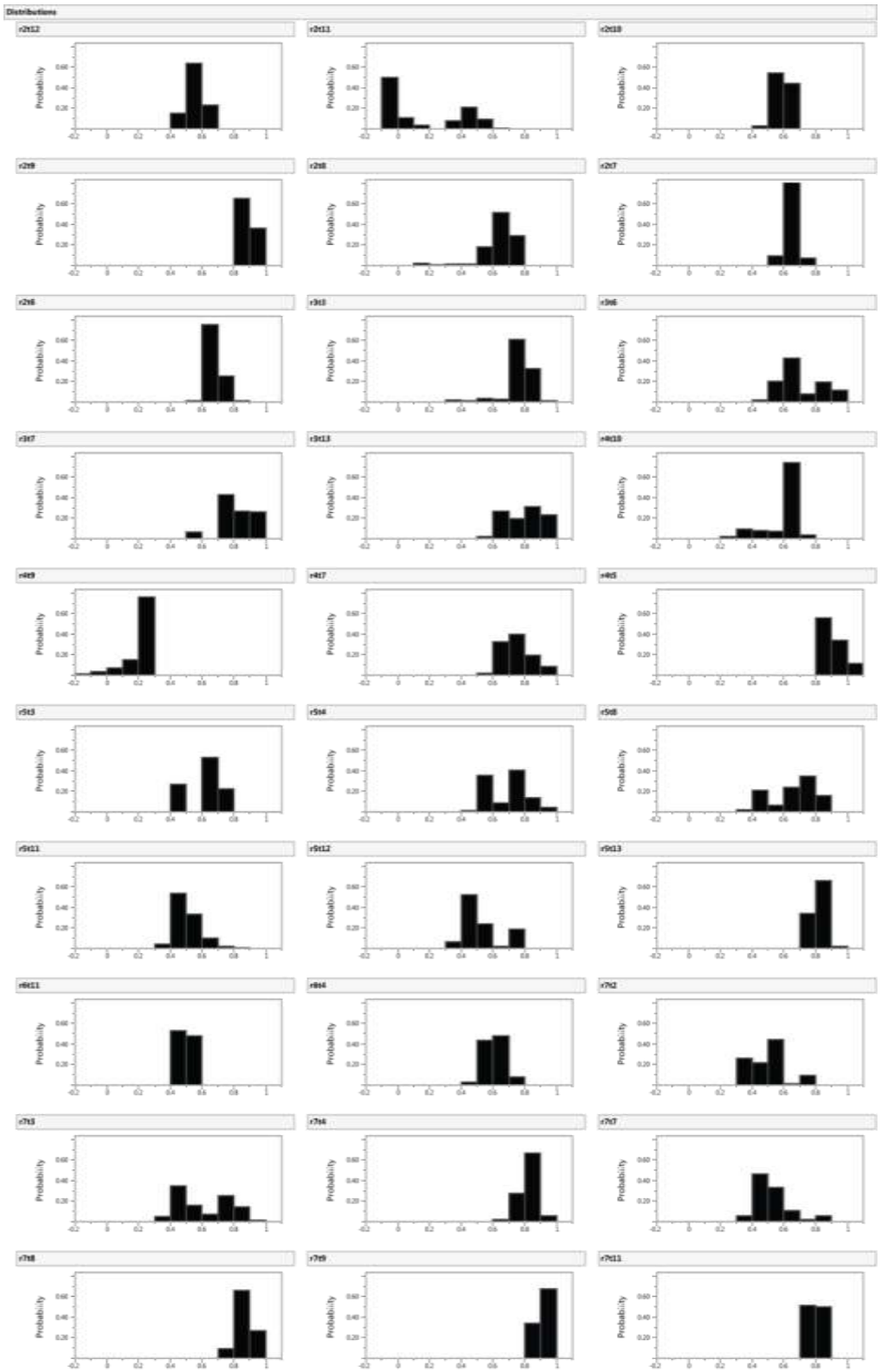

Appendix B.5. Histograms show horizontal position of Olig2+ cells with respect to trap coordinates for discontinuous perfusion (f = 3 d^{-1}) with 6 μM RA and 3 μM Pur, one device. Zero indicates trap entrance and 1 indicates back of trap, where circular trap meets restriction channel.

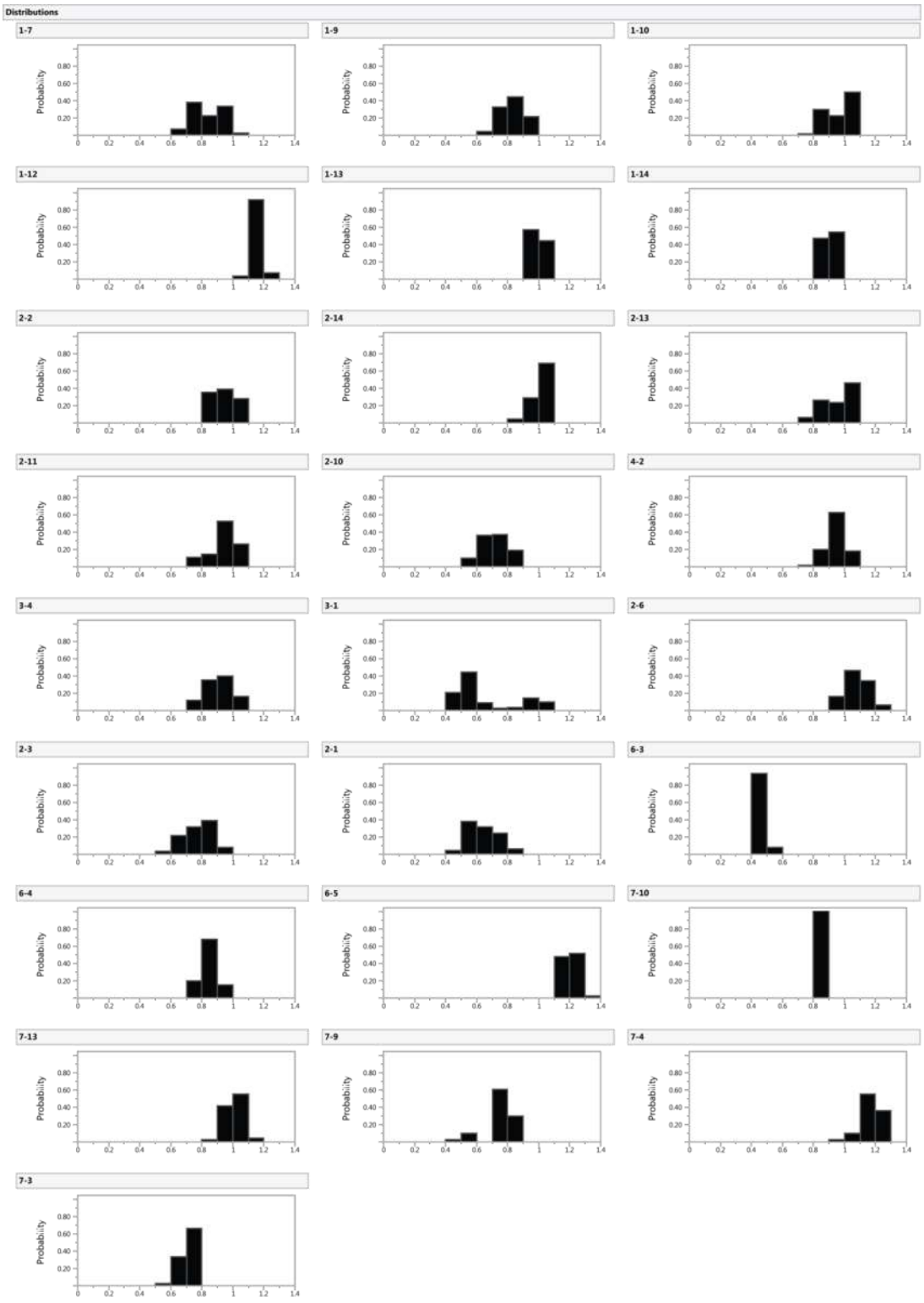

Appendix B.6. Histograms show horizontal position of Olig2+ cells with respect to trap coordinates for discontinuous perfusion (f = 3 d^{-1}) with 6 μM RA and 3 μM Pur, a second device. Zero indicates trap entrance and 1 indicates back of trap, where circular trap meets restriction channel.

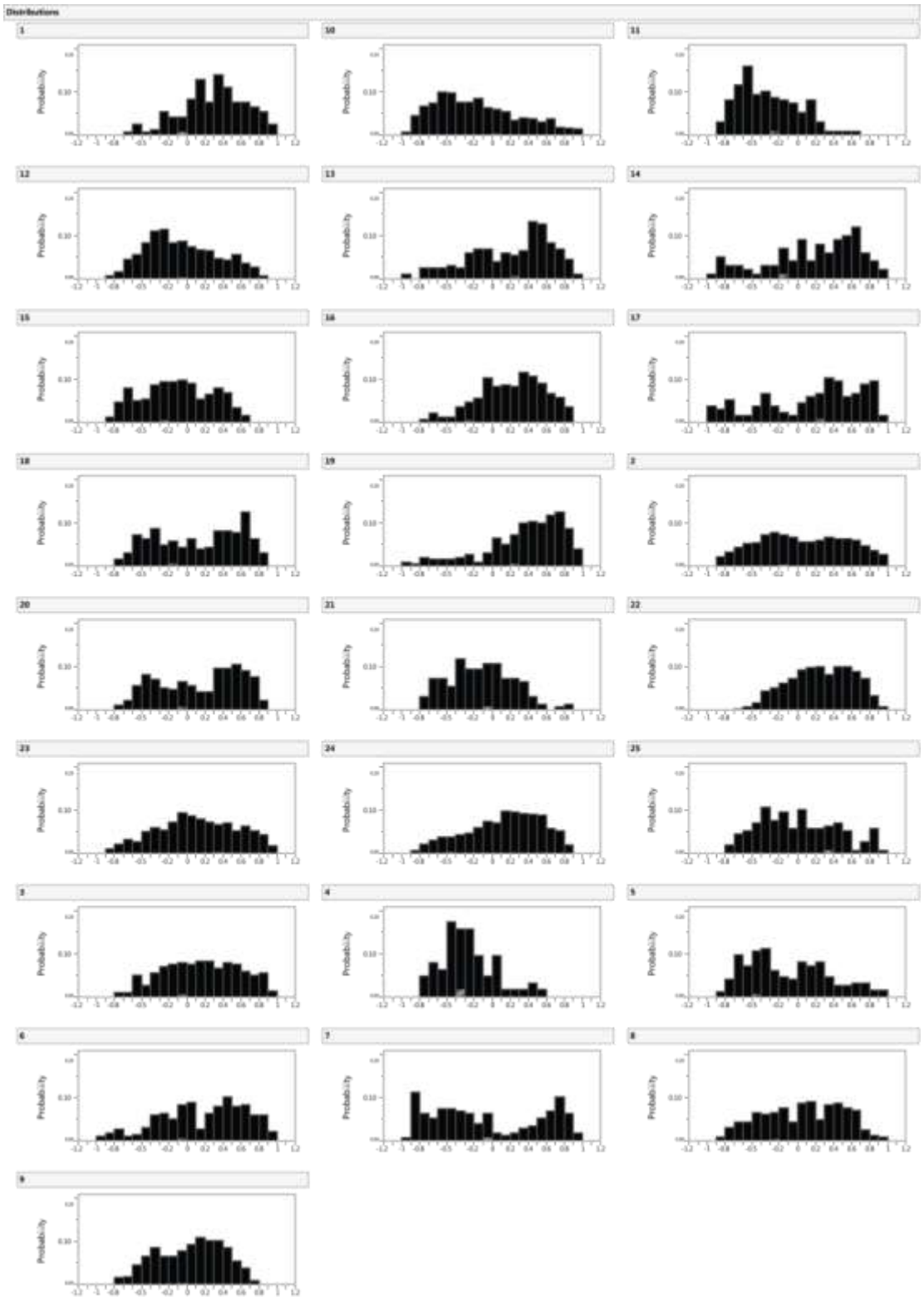

Appendix B.7. Histograms show horizontal position of Olig2+ cells with respect to aggregate center line for plate controls with 6 μM RA and 3 μM Pur. Zero indicates aggregate center line, positive numbers indicate portion of aggregate closer to trap entrance, and negative numbers indicate portion of aggregate closer to back of trap.

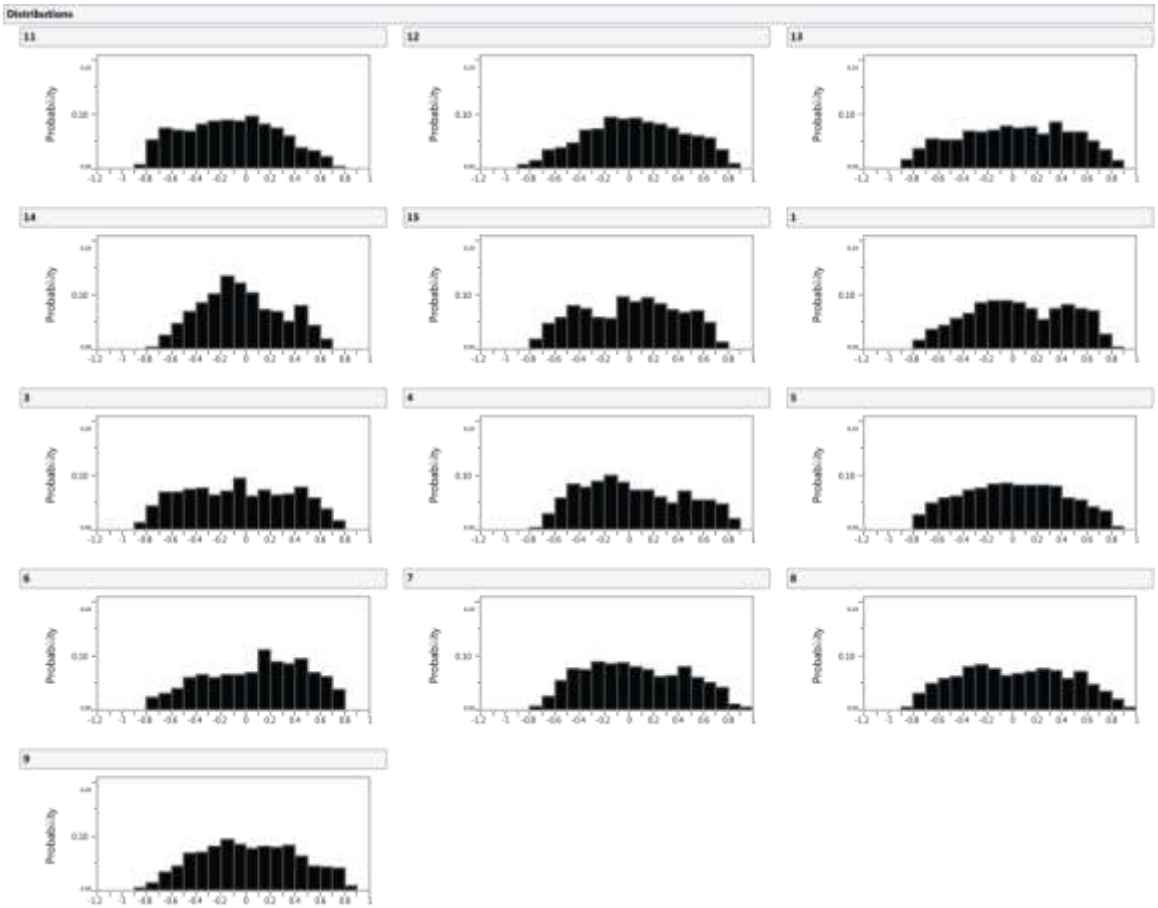

Appendix B.8. Histograms show horizontal position of Olig2+ cells with respect to aggregate center line for plate controls with 2 μM RA and 1.5 μM Pur. Zero indicates aggregate center line, positive numbers indicate portion of aggregate closer to trap entrance, and negative numbers indicate portion of aggregate closer to back of trap.

APPENDIX C: CHAPTER 5 SUPPLEMENTARY MATERIAL

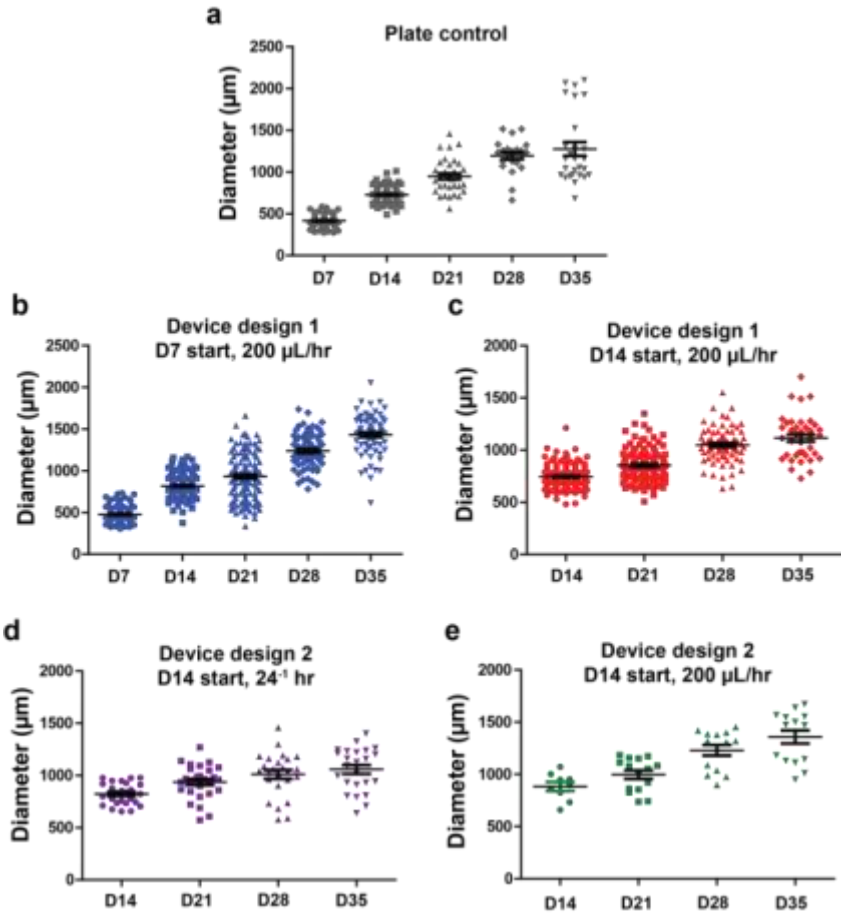

Appendix C.1. Organoid size distributions. Organoid diameter measured at days 14, 21, 28, and 35 of culture. Diameter was calculated from the cross-sectional area of organoids in brightfield images. Each dot represents an individual organoid. Growth rate was calculated, defined as the difference in size between two time points and normalized by the size at the first of the two time points. Error bars are SEM.

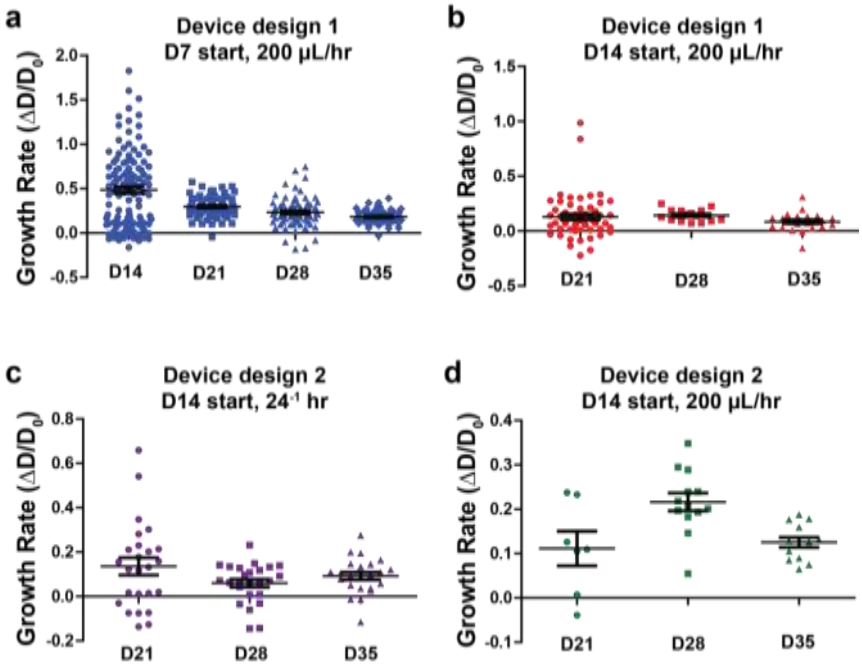

Appendix C.2. Organoid growth rate distributions in device cultures. Growth rate was calculated, defined as the difference in size between two time points and normalized by the size at the first of the two time points. Error bars are SEM.

REFERENCES

1 Jackson, E. L. & Lu, H. Three-dimensional models for studying development and disease: moving on from organisms to organs-on-a-chip and organoids. *Integr Biol (Camb)* **8**, 672-683, doi:10.1039/c6ib00039h (2016).

2 Jackson-Holmes, E. L., McDevitt, T. C. & Lu, H. A microfluidic trap array for longitudinal monitoring and multi-modal phenotypic analysis of individual stem cell aggregates. *Lab Chip* **17**, 3634-3642, doi:10.1039/c7lc00763a (2017).

3 Martin, G. R. Isolation of a pluripotent cell line from early mouse embryos cultured in medium conditioned by teratocarcinoma stem cells. *Proceedings of the National Academy of Sciences* **78**, 7634-7638 (1981).

4 Evans, M. J. & Kaufman, M. H. Establishment in culture of pluripotential cells from mouse embryos. *Nature* **292**, 154-156 (1981).

5 Doetschman, T. C., Eistetter, H., Katz, M., Schmidt, W. & Kemler, R. The in vitro development of blastocyst-derived embryonic stem cell lines: formation of visceral yolk sac, blood islands and myocardium. *Journal of embryology and experimental morphology* **87**, 27-45 (1985).

6 Takahashi, K. *et al.* Induction of pluripotent stem cells from adult human fibroblasts by defined factors. *Cell* **131**, 861-872, doi:10.1016/j.cell.2007.11.019 (2007).

7 Takahashi, K. & Yamanaka, S. Induction of pluripotent stem cells from mouse embryonic and adult fibroblast cultures by defined factors. *Cell* **126**, 663-676, doi:10.1016/j.cell.2006.07.024 (2006).

8 Yu, J. *et al.* Induced pluripotent stem cell lines derived from human somatic cells. *Science* **318**, 1917-1920, doi:10.1126/science.1151526 (2007).

9 Wernig, M. *et al.* In vitro reprogramming of fibroblasts into a pluripotent ES-cell-like state. *Nature* **448**, 318-324, doi:10.1038/nature05944 (2007).

10 Park, I. H. *et al.* Reprogramming of human somatic cells to pluripotency with defined factors. *Nature* **451**, 141-146, doi:10.1038/nature06534 (2008).

11 Itskovitz-Eldor, J. *et al.* Differentiation of human embryonic stem cells into embryoid bodies compromising the three embryonic germ layers. *Molecular medicine (Cambridge, Mass.)* **6**, 88-95 (2000).

12 Dvash, T. *et al.* Temporal gene expression during differentiation of human embryonic stem cells and embryoid bodies. *Human Reproduction* **19**, 2875-2883, doi:10.1093/humrep/deh529 (2004).

13 Zandstra, P. W. *et al.* Scalable production of embryonic stem cell-derived cardiomyocytes. *Tissue engineering* **9**, 767-778, doi:10.1089/107632703768247449 (2003).

14 Zhang, S. C., Wernig, M., Duncan, I. D., Brustle, O. & Thomson, J. A. In vitro differentiation of transplantable neural precursors from human embryonic stem cells. *Nat Biotechnol* **19**, 1129-1133, doi:10.1038/nbt1201-1129 (2001).

15 Carpenedo, R. L., Sargent, C. Y. & McDevitt, T. C. Rotary suspension culture enhances the efficiency, yield, and homogeneity of embryoid body differentiation. *Stem cells* **25**, 2224-2234, doi:10.1634/stemcells.2006-0523 (2007).

16 Sargent, C. Y. *et al.* Hydrodynamic modulation of embryonic stem cell differentiation by rotary orbital suspension culture. *Biotechnol Bioeng* **105**, 611-626, doi:10.1002/bit.22578 (2010).

17 Kinney, M. A., Saeed, R. & McDevitt, T. C. Systematic analysis of embryonic stem cell differentiation in hydrodynamic environments with controlled embryoid body size. *Integr Biol (Camb)* **4**, 641-650, doi:10.1039/c2ib00165a (2012).

18 Hwang, Y. S. *et al.* Microwell-mediated control of embryoid body size regulates embryonic stem cell fate via differential expression of WNT5a and WNT11. *Proceedings of the National Academy of Sciences of the United States of America* **106**, 16978-16983, doi:10.1073/pnas.0905550106 (2009).

19 Bauwens, C. L. *et al.* Control of human embryonic stem cell colony and aggregate size heterogeneity influences differentiation trajectories. *Stem cells* **26**, 2300-2310, doi:10.1634/stemcells.2008-0183 (2008).

20 Mohr, J. C. *et al.* The microwell control of embryoid body size in order to regulate cardiac differentiation of human embryonic stem cells. *Biomaterials* **31**, 1885-1893, doi:10.1016/j.biomaterials.2009.11.033 (2010).

21 Wilson, J. L., Najia, M. A., Saeed, R. & McDevitt, T. C. Alginate encapsulation parameters influence the differentiation of microencapsulated embryonic stem cell aggregates. *Biotechnol Bioeng* **111**, 618-631, doi:10.1002/bit.25121 (2014).

22 Guvendiren, M. & Burdick, J. A. Engineering synthetic hydrogel microenvironments to instruct stem cells. *Curr Opin Biotechnol* **24**, 841-846, doi:10.1016/j.copbio.2013.03.009 (2013).

23 Lutolf, M. P. & Hubbell, J. A. Synthetic biomaterials as instructive extracellular microenvironments for morphogenesis in tissue engineering. *Nat Biotechnol* **23**, 47-55, doi:10.1038/nbt1055 (2005).

24 Bratt-Leal, A. M., Nguyen, A. H., Hammersmith, K. A., Singh, A. & McDevitt, T. C. A microparticle approach to morphogen delivery within pluripotent stem

cell aggregates. *Biomaterials* **34**, 7227-7235, doi:10.1016/j.biomaterials.2013.05.079 (2013).

25 Hettiaratchi, M. H., Miller, T., Temenoff, J. S., Guldberg, R. E. & McDevitt, T. C. Heparin Microparticle Effects on Presentation and Bioactivity of Bone Morphogenetic Protein-2. *Biomaterials* **35**, 7228-7238, doi:10.1016/j.biomaterials.2014.05.011 (2014).

26 Nguyen, A. H., Wang, Y., White, D. E., Platt, M. O. & McDevitt, T. C. MMP-mediated Mesenchymal Morphogenesis of Pluripotent Stem Cell Aggregates Stimulated by Gelatin Methacrylate Microparticle Incorporation. *Biomaterials* **76**, 66-75, doi:10.1016/j.biomaterials.2015.10.043 (2016).

27 Maltsev, V. A., Wobus, A. M., Rohwedel, J., Bader, M. & Hescheler, J. Cardiomyocytes differentiated in vitro from embryonic stem cells developmentally express cardiac-specific genes and ionic currents. *Circulation Research* **75**, 233-244, doi:10.1161/01.res.75.2.233 (1994).

28 Ng, E. S., Davis, R. P., Azzola, L., Stanley, E. G. & Elefanty, A. G. Forced aggregation of defined numbers of human embryonic stem cells into embryoid bodies fosters robust, reproducible hematopoietic differentiation. *Blood* **106**, 1601-1603, doi:10.1182/blood-2005-03-0987 (2005).

29 Koike, M., Kurosawa, H. & Amano, Y. A Round-bottom 96-well Polystyrene Plate Coated with 2-methacryloyloxyethyl Phosphorylcholine as an Effective Tool for Embryoid Body Formation. *Cytotechnology* **47**, 3-10, doi:10.1007/s10616-005-3743-x (2005).

30 Nakazawa, K., Yoshiura, Y., Koga, H. & Sakai, Y. Characterization of mouse embryoid bodies cultured on microwell chips with different well sizes. *Journal of bioscience and bioengineering* **116**, 628-633, doi:10.1016/j.jbiosc.2013.05.005 (2013).

31 Moeller, H. C., Mian, M. K., Shrivastava, S., Chung, B. G. & Khademhosseini, A. A microwell array system for stem cell culture. *Biomaterials* **29**, 752-763, doi:10.1016/j.biomaterials.2007.10.030 (2008).

32 Azarin, S. M. *et al.* Modulation of Wnt/beta-catenin signaling in human embryonic stem cells using a 3-D microwell array. *Biomaterials* **33**, 2041-2049, doi:10.1016/j.biomaterials.2011.11.070 (2012).

33 Bauwens, C. L. *et al.* Geometric control of cardiomyogenic induction in human pluripotent stem cells. *Tissue engineering. Part A* **17**, 1901-1909, doi:10.1089/ten.TEA.2010.0563 (2011).

34 Cameron, C. M., Hu, W. S. & Kaufman, D. S. Improved development of human embryonic stem cell-derived embryoid bodies by stirred vessel cultivation. *Biotechnol Bioeng* **94**, 938-948, doi:10.1002/bit.20919 (2006).

35 Wichterle, H., Lieberam, I., Porter, J. A. & Jessell, T. M. Directed differentiation of embryonic stem cells into motor neurons. *Cell* **110**, 385-397 (2002).

36 Shin, S., Dalton, S. & Stice, D. S. L. Human Motor Neuron Differentiation from Human Embryonic Stem Cells. *Stem Cells and Development* **14**, 266-269, doi:10.1089/scd.2005.14.266 (2005).

37 Li, X. J. *et al.* Specification of motoneurons from human embryonic stem cells. *Nat Biotechnol* **23**, 215-221, doi:10.1038/nbt1063 (2005).

38 Karumbayaram, S. *et al.* Directed differentiation of human induced pluripotent stem cells generates active motor neurons. *Stem cells (Dayton, Ohio)* **27**, 806-811, doi:10.1002/stem.31 (2009).

39 Mizuguchi, R. *et al.* Combinatorial roles of olig2 and neurogenin2 in the coordinated induction of pan-neuronal and subtype-specific properties of motoneurons. *Neuron* **31**, 757-771 (2001).

40 Novitch, B. G., Chen, A. I. & Jessell, T. M. Coordinate regulation of motor neuron subtype identity and pan-neuronal properties by the bHLH repressor Olig2. *Neuron* **31**, 773-789 (2001).

41 Xian, H. & Gottlieb, D. I. Dividing Olig2-expressing progenitor cells derived from ES cells. *Glia* **47**, 88-101, doi:10.1002/glia.20010 (2004).

42 Lu, Q. R. *et al.* Common developmental requirement for Olig function indicates a motor neuron/oligodendrocyte connection. *Cell* **109**, 75-86 (2002).

43 McCreedy, D. A. *et al.* A new method for generating high purity motoneurons from mouse embryonic stem cells. *Biotechnol Bioeng* **111**, 2041-2055, doi:10.1002/bit.25260 (2014).

44 McCreedy, D. A., Rieger, C. R., Gottlieb, D. I. & Sakiyama-Elbert, S. E. Transgenic enrichment of mouse embryonic stem cell-derived progenitor motor neurons. *Stem Cell Res* **8**, 368-378, doi:10.1016/j.scr.2011.12.003 (2012).

45 Li, X. J. *et al.* Directed differentiation of ventral spinal progenitors and motor neurons from human embryonic stem cells by small molecules. *Stem cells* **26**, 886-893, doi:10.1634/stemcells.2007-0620 (2008).

46 Sasai, Y. Next-generation regenerative medicine: organogenesis from stem cells in 3D culture. *Cell Stem Cell* **12**, 520-530, doi:10.1016/j.stem.2013.04.009 (2013).

47 Sasai, Y. Cytosystems dynamics in self-organization of tissue architecture. *Nature* **493**, 318-326, doi:10.1038/nature11859 (2013).

48 Eiraku, M. *et al.* Self-organizing optic-cup morphogenesis in three-dimensional culture. *Nature* **472**, 51-56, doi:http://www.nature.com/nature/journal/v472/n7341/abs/10.1038-nature09941-unlocked.html#supplementary-information (2011).

49 Sato, T. *et al.* Single Lgr5 stem cells build crypt-villus structures in vitro without a mesenchymal niche. *Nature* **459**, 262-265, doi:10.1038/nature07935 (2009).

50 Takasato, M. *et al.* Kidney organoids from human iPS cells contain multiple lineages and model human nephrogenesis. *Nature* **526**, 564-568, doi:10.1038/nature15695 (2015).

51 Takebe, T. *et al.* Vascularized and functional human liver from an iPSC-derived organ bud transplant. *Nature* **499**, 481-484, doi:10.1038/nature12271 http://www.nature.com/nature/journal/v499/n7459/abs/nature12271.html#supplementary-information (2013).

52 Lancaster, M. A. *et al.* Cerebral organoids model human brain development and microcephaly. *Nature* **501**, 373-379, doi:10.1038/nature12517 http://www.nature.com/nature/journal/v501/n7467/abs/nature12517.html#supplementary-information (2013).

53 Shi, Y., Inoue, H., Wu, J. C. & Yamanaka, S. Induced pluripotent stem cell technology: a decade of progress. *Nat Rev Drug Discov* **16**, 115-130, doi:10.1038/nrd.2016.245 (2017).

54 Dutta, D., Heo, I. & Clevers, H. Disease Modeling in Stem Cell-Derived 3D Organoid Systems. *Trends Mol Med* **23**, 393-410, doi:10.1016/j.molmed.2017.02.007 (2017).

55 Sutcliffe, M. & Lancaster, M. A. A Simple Method of Generating 3D Brain Organoids Using Standard Laboratory Equipment. *Methods Mol Biol*, doi:10.1007/7651_2017_2 (2017).

56 Qian, X. *et al.* Brain-Region-Specific Organoids Using Mini-bioreactors for Modeling ZIKV Exposure. *Cell* **165**, 1238-1254, doi:10.1016/j.cell.2016.04.032 (2016).

57 Chung, K. *et al.* Structural and molecular interrogation of intact biological systems. *Nature* **497**, 332-337, doi:10.1038/nature12107 (2013).

58 Hama, H. *et al.* Scale: a chemical approach for fluorescence imaging and reconstruction of transparent mouse brain. *Nat Neurosci* **14**, 1481-1488, doi:10.1038/nn.2928 (2011).

59 Susaki, E. A. *et al.* Whole-brain imaging with single-cell resolution using chemical cocktails and computational analysis. *Cell* **157**, 726-739, doi:10.1016/j.cell.2014.03.042 (2014).

60 Erturk, A. *et al.* Three-dimensional imaging of solvent-cleared organs using 3DISCO. *Nature protocols* **7**, 1983-1995, doi:10.1038/nprot.2012.119 (2012).

61 Kelava, I. & Lancaster, M. A. Stem Cell Models of Human Brain Development. *Cell Stem Cell* **18**, 736-748, doi:10.1016/j.stem.2016.05.022 (2016).

62 Iefremova, V. *et al.* An Organoid-Based Model of Cortical Development Identifies Non-Cell-Autonomous Defects in Wnt Signaling Contributing to Miller-Dieker Syndrome. *Cell Rep* **19**, 50-59, doi:10.1016/j.celrep.2017.03.047 (2017).

63 Bagley, J. A., Reumann, D., Bian, S., Levi-Strauss, J. & Knoblich, J. A. Fused cerebral organoids model interactions between brain regions. *Nat Methods* **14**, 743-751, doi:10.1038/nmeth.4304 (2017).

64 Renner, M. *et al.* Self-organized developmental patterning and differentiation in cerebral organoids. *EMBO J* **36**, 1316-1329, doi:10.15252/embj.201694700 (2017).

65 Yan, Y., Song, L., Madinya, J., Ma, T. & Li, Y. Derivation of Cortical Spheroids from Human Induced Pluripotent Stem Cells in a Suspension Bioreactor. *Tissue engineering. Part A* **24**, 418-431, doi:10.1089/ten.TEA.2016.0400 (2018).

66 Li, Y. *et al.* Induction of Expansion and Folding in Human Cerebral Organoids. *Cell Stem Cell* **20**, 385-396 e383, doi:10.1016/j.stem.2016.11.017 (2017).

67 Mariani, J. *et al.* FOXG1-Dependent Dysregulation of GABA/Glutamate Neuron Differentiation in Autism Spectrum Disorders. *Cell* **162**, 375-390, doi:10.1016/j.cell.2015.06.034 (2015).

68 and, Y. X. & Whitesides, G. M. SOFT LITHOGRAPHY. *Annual Review of Materials Science* **28**, 153-184, doi:doi:10.1146/annurev.matsci.28.1.153 (1998).

69 Sia, S. K. & Whitesides, G. M. Microfluidic devices fabricated in poly(dimethylsiloxane) for biological studies. *Electrophoresis* **24**, 3563-3576, doi:10.1002/elps.200305584 (2003).

70 Whitesides, G. M. The origins and the future of microfluidics. *Nature* **442**, 368-373 (2006).

71 Whitesides, G. M., Ostuni, E., Takayama, S., Jiang, X. & Ingber, D. E. Soft Lithography in Biology and Biochemistry. *Annual Review of Biomedical Engineering* **3**, 335-373, doi:doi:10.1146/annurev.bioeng.3.1.335 (2001).

72 Sakai, Y. *et al.* Detachably assembled microfluidic device for perfusion culture and post-culture analysis of a spheroid array. *Biotechnology journal* **9**, 971-979, doi:10.1002/biot.201300559 (2014).

73 Kim, C. *et al.* 3-Dimensional cell culture for on-chip differentiation of stem cells in embryoid body. *Lab Chip* **11**, 874-882, doi:10.1039/c0lc00516a (2011).

74 Occhetta, P. *et al.* High-Throughput Microfluidic Platform for 3D Cultures of Mesenchymal Stem Cells, Towards Engineering Developmental Processes. *Sci Rep* **5**, 10288, doi:10.1038/srep10288 (2015).

75 Patra, B. *et al.* A microfluidic device for uniform-sized cell spheroids formation, culture, harvesting and flow cytometry analysis. *Biomicrofluidics* **7**, 54114, doi:10.1063/1.4824480 (2013).

76 Fu, C. Y. *et al.* A microfluidic chip with a U-shaped microstructure array for multicellular spheroid formation, culturing and analysis. *Biofabrication* **6**, 015009, doi:10.1088/1758-5082/6/1/015009 (2014).

77 de Groot, T. E., Veserat, K. S., Berthier, E., Beebe, D. J. & Theberge, A. B. Surface-tension driven open microfluidic platform for hanging droplet culture. *Lab Chip* **16**, 334-344, doi:10.1039/c5lc01353d (2016).

78 Frey, O., Misun, P. M., Fluri, D. A., Hengstler, J. G. & Hierlemann, A. Reconfigurable microfluidic hanging drop network for multi-tissue interaction and analysis. *Nat Commun* **5**, 4250, doi:10.1038/ncomms5250 (2014).

79 Lee, W. G., Ortmann, D., Hancock, M. J., Bae, H. & Khademhosseini, A. A hollow sphere soft lithography approach for long-term hanging drop methods. *Tissue engineering. Part C, Methods* **16**, 249-259, doi:10.1089/ten.TEC.2009.0248 (2010).

80 Rismani Yazdi, S. *et al.* Adding the 'heart' to hanging drop networks for microphysiological multi-tissue experiments. *Lab Chip* **15**, 4138-4147, doi:10.1039/c5lc01000d (2015).

81 Chan, H. F. *et al.* Rapid formation of multicellular spheroids in double-emulsion droplets with controllable microenvironment. **3**, 3462, doi:10.1038/srep03462 https://www.nature.com/articles/srep03462#supplementary-information (2013).

82 Sart, S., Tomasi, R. F. X., Amselem, G. & Baroud, C. N. Multiscale cytometry and regulation of 3D cell cultures on a chip. *Nature Communications* **8**, 469, doi:10.1038/s41467-017-00475-x (2017).

83 Astolfi, M. *et al.* Micro-dissected tumor tissues on chip: an ex vivo method for drug testing and personalized therapy. *Lab Chip* **16**, 312-325, doi:10.1039/c5lc01108f (2016).

84 Bergstrom, G., Christoffersson, J., Schwanke, K., Zweigerdt, R. & Mandenius, C. F. Stem cell derived in vivo-like human cardiac bodies in a microfluidic device for toxicity testing by beating frequency imaging. *Lab Chip* **15**, 3242-3249, doi:10.1039/c5lc00449g (2015).

85 Hribar, K. C. *et al.* Nonlinear 3D projection printing of concave hydrogel microstructures for long-term multicellular spheroid and embryoid body culture. *Lab Chip* **15**, 2412-2418, doi:10.1039/c5lc00159e (2015).

86 Khoury, M. *et al.* A microfluidic traps system supporting prolonged culture of human embryonic stem cells aggregates. *Biomed Microdevices* **12**, 1001-1008, doi:10.1007/s10544-010-9454-x (2010).

87 Ruppen, J. *et al.* A microfluidic platform for chemoresistive testing of multicellular pleural cancer spheroids. *Lab Chip* **14**, 1198-1205, doi:10.1039/c3lc51093j (2014).

88 Suri, S. *et al.* Microfluidic-based patterning of embryonic stem cells for in vitro development studies. *Lab Chip* **13**, 4617-4624, doi:10.1039/c3lc50663k (2013).

89 Zhu, Y. *et al.* In situ generation of human brain organoids on a micropillar array. *Lab Chip* **17**, 2941-2950, doi:10.1039/c7lc00682a (2017).

90 Wang, Y., Wang, L., Guo, Y., Zhu, Y. & Qin, J. Engineering stem cell-derived 3D brain organoids in a perfusable organ-on-a-chip system. *RSC Advances* **8**, 1677-1685, doi:10.1039/c7ra11714k (2018).

91 Wang, Y., Wang, L., Zhu, Y. & Qin, J. Human brain organoid-on-a-chip to model prenatal nicotine exposure. *Lab Chip* **18**, 851-860, doi:10.1039/c7lc01084b (2018).

92 Chen, C. S., Mrksich, M., Huang, S., Whitesides, G. M. & Ingber, D. E. Micropatterned surfaces for control of cell shape, position, and function. *Biotechnol Prog* **14**, 356-363, doi:10.1021/bp980031m (1998).

93 Takayama, S. *et al.* Patterning cells and their environments using multiple laminar fluid flows in capillary networks. *Proceedings of the National Academy of Sciences* **96**, 5545-5548, doi:10.1073/pnas.96.10.5545 (1999).

94 Takayama, S. *et al.* Subcellular positioning of small molecules. *Nature* **411**, 1016, doi:10.1038/35082637 (2001).

95 Mettetal, J. T., Muzzey, D., Gómez-Uribe, C. & van Oudenaarden, A. The Frequency Dependence of Osmo-Adaptation in Saccharomyces cerevisiae. *Science* **319**, 482-484, doi:10.1126/science.1151582 (2008).

96 Bennett, M. R. *et al.* Metabolic gene regulation in a dynamically changing environment. *Nature* **454**, 1119-1122, doi:10.1038/nature07211 (2008).

97 Charvin, G., Cross, F. R. & Siggia, E. D. Forced periodic expression of G1 cyclins phase-locks the budding yeast cell cycle. *Proceedings of the National Academy of Sciences of the United States of America* **106**, 6632-6637, doi:10.1073/pnas.0809227106 (2009).

98 Blagovic, K., Kim, L. Y. & Voldman, J. Microfluidic Perfusion for Regulating Diffusible Signaling in Stem Cells. *PLoS ONE* **6**, e22892, doi:10.1371/journal.pone.0022892 (2011).

99 Przybyla, L. M. & Voldman, J. Attenuation of extrinsic signaling reveals the importance of matrix remodeling on maintenance of embryonic stem cell self-renewal. *Proceedings of the National Academy of Sciences of the United States of America* **109**, 835-840, doi:10.1073/pnas.1103100109 (2012).

100 Przybyla, L. & Voldman, J. Probing embryonic stem cell autocrine and paracrine signaling using microfluidics. *Annu Rev Anal Chem (Palo Alto Calif)* **5**, 293-315, doi:10.1146/annurev-anchem-062011-143122 (2012).

101 Thomson, J. A. *et al.* Embryonic stem cell lines derived from human blastocysts. *Science* **282**, 1145-1147 (1998).

102 Sato, T. *et al.* Single Lgr5 stem cells build crypt–villus structures in vitro without a mesenchymal niche. *Nature* **459**, 262-265, doi:http://www.nature.com/nature/journal/v459/n7244/suppinfo/nature07935_S1.html (2009).

103 Kinney, M. A., Hookway, T. A., Wang, Y. & McDevitt, T. C. Engineering three-dimensional stem cell morphogenesis for the development of tissue models and scalable regenerative therapeutics. *Annals of biomedical engineering* **42**, 352-367, doi:10.1007/s10439-013-0953-9 (2014).

104 Zandstra, P. W., Le, H. V., Daley, G. Q., Griffith, L. G. & Lauffenburger, D. A. Leukemia inhibitory factor (LIF) concentration modulates embryonic stem cell self-renewal and differentiation independently of proliferation. *Biotechnol Bioeng* **69**, 607-617 (2000).

105 Yu, H., Alexander, C. M. & Beebe, D. J. Understanding microchannel culture: parameters involved in soluble factor signaling. *Lab Chip* **7**, 726-730, doi:10.1039/b618793e (2007).

106 Ungrin, M. D., Joshi, C., Nica, A., Bauwens, C. & Zandstra, P. W. Reproducible, ultra high-throughput formation of multicellular organization from single cell suspension-derived human embryonic stem cell aggregates. *PLoS One* **3**, e1565, doi:10.1371/journal.pone.0001565 (2008).

107 Alessandri, K. *et al.* Cellular capsules as a tool for multicellular spheroid production and for investigating the mechanics of tumor progression in vitro. *Proceedings of the National Academy of Sciences* **110**, 14843-14848, doi:10.1073/pnas.1309482110 (2013).

108 El-Ali, J., Sorger, P. K. & Jensen, K. F. Cells on chips. *Nature* **442**, 403-411, doi:10.1038/nature05063 (2006).

109 Chen, Y. H., Peng, C. C. & Tung, Y. C. Flip channel: A microfluidic device for uniform-sized embryoid body formation and differentiation. *Biomicrofluidics* **9**, 054111, doi:10.1063/1.4931638 (2015).

110 Lou, X., Kang, M., Xenopoulos, P., Munoz-Descalzo, S. & Hadjantonakis, A. K. A rapid and efficient 2D/3D nuclear segmentation method for analysis of early mouse embryo and stem cell image data. *Stem Cell Reports* **2**, 382-397, doi:10.1016/j.stemcr.2014.01.010 (2014).

111 Wang, F. *et al.* Microfluidic delivery of small molecules into mammalian cells based on hydrodynamic focusing. *Biotechnology and Bioengineering* **100**, 150-158, doi:10.1002/bit.21737 (2008).

112 Chung, K. *et al.* A microfluidic array for large-scale ordering and orientation of embryos. *Nat Methods* **8**, 171-176, doi:10.1038/nmeth.1548 (2011).

113 Chung, K., Rivet, C. A., Kemp, M. L. & Lu, H. Imaging single-cell signaling dynamics with a deterministic high-density single-cell trap array. *Analytical chemistry* **83**, 7044-7052, doi:10.1021/ac2011153 (2011).

114 Levario, T. J., Zhan, M., Lim, B., Shvartsman, S. Y. & Lu, H. Microfluidic trap array for massively parallel imaging of Drosophila embryos. *Nature protocols* **8**, 721-736, doi:10.1038/nprot.2013.034 (2013).

115 White, D. E. *et al.* Quantitative multivariate analysis of dynamic multicellular morphogenic trajectories. *Integr Biol (Camb)* **7**, 825-833, doi:10.1039/c5ib00072f (2015).

116 Vrij, E. J. *et al.* 3D high throughput screening and profiling of embryoid bodies in thermoformed microwell plates. *Lab Chip* **16**, 734-742, doi:10.1039/c5lc01499a (2016).

117 Young, E. W. & Beebe, D. J. Fundamentals of microfluidic cell culture in controlled microenvironments. *Chem Soc Rev* **39**, 1036-1048, doi:10.1039/b909900j (2010).

118 Kim, L., Toh, Y. C., Voldman, J. & Yu, H. A practical guide to microfluidic perfusion culture of adherent mammalian cells. *Lab Chip* **7**, 681-694, doi:10.1039/b704602b (2007).

119 ten Berge, D. *et al.* Embryonic stem cells require Wnt proteins to prevent differentiation to epiblast stem cells. *Nat Cell Biol* **13**, 1070-1075, doi:10.1038/ncb2314 (2011).

120 Bendall, S. C. *et al.* IGF and FGF cooperatively establish the regulatory stem cell niche of pluripotent human cells in vitro. *Nature* **448**, 1015-1021, doi:10.1038/nature06027 (2007).

121 Ogawa, K. *et al.* Activin-Nodal signaling is involved in propagation of mouse embryonic stem cells. *Journal of Cell Science* **120**, 55-65, doi:10.1242/jcs.03296 (2007).

122 Mittal, N. & Voldman, J. Nonmitogenic survival-enhancing autocrine factors including cyclophilin A contribute to density-dependent mouse embryonic stem cell growth. *Stem Cell Res* **6**, 168-176, doi:10.1016/j.scr.2010.10.001 (2011).

123 Chung, B. G. *et al.* Human neural stem cell growth and differentiation in a gradient-generating microfluidic device. *Lab Chip* **5**, 401-406, doi:10.1039/b417651k (2005).

124 Giobbe, G. G. *et al.* Confined 3D microenvironment regulates early differentiation in human pluripotent stem cells. *Biotechnol Bioeng* **109**, 3119-3132, doi:10.1002/bit.24571 (2012).

125 Cimetta, E., Figallo, E., Cannizzaro, C., Elvassore, N. & Vunjak-Novakovic, G. Micro-bioreactor arrays for controlling cellular environments: design principles for human embryonic stem cell applications. *Methods* **47**, 81-89, doi:10.1016/j.ymeth.2008.10.015 (2009).

126 Giobbe, G. G. *et al.* Functional differentiation of human pluripotent stem cells on a chip. *Nat Methods* **12**, 637-640, doi:10.1038/nmeth.3411 (2015).

127 Swetenburg, R., White, D.E., McDevitt, T.C., Kemp, M.L., Stice, S. . Elucidating motor neuron and oligodendrocyte differentiation pathways via computational analysis of subpopulation dynamics. *In revision*.

128 McMurtrey, R. J. Analytic Models of Oxygen and Nutrient Diffusion, Metabolism Dynamics, and Architecture Optimization in Three-Dimensional Tissue Constructs with Applications and Insights in Cerebral Organoids. *Tissue engineering. Part C, Methods* **22**, 221-249, doi:10.1089/ten.TEC.2015.0375 (2016).

129 Griffith, L. G. & Swartz, M. A. Capturing complex 3D tissue physiology in vitro. *Nature reviews. Molecular cell biology* **7**, 211-224, doi:10.1038/nrm1858 (2006).

130 Regehr, K. J. *et al.* Biological implications of polydimethylsiloxane-based microfluidic cell culture. *Lab Chip* **9**, 2132-2139, doi:10.1039/b903043c (2009).

131 Toepke, M. W. & Beebe, D. J. PDMS absorption of small molecules and consequences in microfluidic applications. *Lab Chip* **6**, 1484-1486, doi:10.1039/b612140c (2006).

132 Wang, J. D., Douville, N. J., Takayama, S. & ElSayed, M. Quantitative analysis of molecular absorption into PDMS microfluidic channels. *Annals of biomedical engineering* **40**, 1862-1873, doi:10.1007/s10439-012-0562-z (2012).

133 United States Environmental Protection Agency. *Chemistry Dashboard: Purmorphamine*, <https://comptox.epa.gov/dashboard/dsstoxdb/results?search=DTXSID20415293 > (

134 McMurtrey, R. J. Roles of Diffusion Dynamics in Stem Cell Signaling and Three-Dimensional Tissue Development. *Stem Cells Dev* **26**, 1293-1303, doi:10.1089/scd.2017.0066 (2017).

135 Herculano-Houzel, S. Scaling of brain metabolism with a fixed energy budget per neuron: implications for neuronal activity, plasticity and evolution. *PLoS One* **6**, e17514, doi:10.1371/journal.pone.0017514 (2011).

136 Varum, S. *et al.* Energy metabolism in human pluripotent stem cells and their differentiated counterparts. *PLoS One* **6**, e20914, doi:10.1371/journal.pone.0020914 (2011).

137 Chen, X. *et al.* Investigations into the metabolism of two-dimensional colony and suspended microcarrier cultures of human embryonic stem cells in serum-free media. *Stem Cells Dev* **19**, 1781-1792, doi:10.1089/scd.2010.0077 (2010).

138 Turner, J. *et al.* Metabolic profiling and flux analysis of MEL-2 human embryonic stem cells during exponential growth at physiological and atmospheric oxygen concentrations. *PLoS One* **9**, e112757, doi:10.1371/journal.pone.0112757 (2014).

139 Abdollahi, H. *et al.* The role of hypoxia in stem cell differentiation and therapeutics. *J Surg Res* **165**, 112-117, doi:10.1016/j.jss.2009.09.057 (2011).

140 Csete, M. Oxygen in the cultivation of stem cells. *Ann N Y Acad Sci* **1049**, 1-8, doi:10.1196/annals.1334.001 (2005).

141 Lim, H. J. *et al.* Biochemical and morphological effects of hypoxic environment on human embryonic stem cells in long-term culture and differentiating embryoid bodies. *Mol Cells* **31**, 123-132, doi:10.1007/s10059-011-0016-8 (2011).

142 Dias, J. M., Alekseenko, Z., Applequist, J. M. & Ericson, J. Tgfbeta signaling regulates temporal neurogenesis and potency of neural stem cells in the CNS. *Neuron* **84**, 927-939, doi:10.1016/j.neuron.2014.10.033 (2014).

143 Warmflash, A., Sorre, B., Etoc, F., Siggia, E. D. & Brivanlou, A. H. A method to recapitulate early embryonic spatial patterning in human embryonic stem cells. *Nature Methods* **11**, 847, doi:10.1038/nmeth.3016 https://www.nature.com/articles/nmeth.3016#supplementary-information (2014).

144 Xue, X. *et al.* Mechanics-guided embryonic patterning of neuroectoderm tissue from human pluripotent stem cells. *Nature materials*, doi:10.1038/s41563-018-0082-9 (2018).

145 Bratt-Leal, A. M., Kepple, K. L., Carpenedo, R. L., Cooke, M. T. & McDevitt, T. C. Magnetic manipulation and spatial patterning of multi-cellular stem cell aggregates. *Integr Biol (Camb)* **3**, 1224-1232, doi:10.1039/c1ib00064k (2011).

146 ten Berge, D. *et al.* Wnt signaling mediates self-organization and axis formation in embryoid bodies. *Cell Stem Cell* **3**, 508-518, doi:10.1016/j.stem.2008.09.013 (2008).

147 van den Brink, S. C. *et al.* Symmetry breaking, germ layer specification and axial organisation in aggregates of mouse embryonic stem cells. *Development* **141**, 4231-4242, doi:10.1242/dev.113001 (2014).

148 Aghvami, S. A. *et al.* Rapid prototyping of cyclic olefin copolymer (COC) microfluidic devices. *Sensors and Actuators B: Chemical* **247**, 940-949, doi:10.1016/j.snb.2017.03.023 (2017).

149 Bernard, M. *et al.* Biocompatibility assessment of cyclic olefin copolymers: Impact of two additives on cytotoxicity, oxidative stress, inflammatory reactions, and hemocompatibility. *J Biomed Mater Res A* **105**, 3333-3349, doi:10.1002/jbm.a.36199 (2017).

150 Lee, U. N. *et al.* Fundamentals of rapid injection molding for microfluidic cell-based assays. *Lab Chip* **18**, 496-504, doi:10.1039/c7lc01052d (2018).